UNIVERSITY OF SOUTHAMPTON

DEVELOPMENT OF HOLLOW-CORE PHOTONIC BANDGAP FIBRES FREE OF SURFACE MODES

by

Rodrigo Amezcua Correa

A thesis submitted in partial fulfillment for the
degree of Doctor of Philosophy

in the
Faculty of Engineering, Science and Mathematics
Optoelectronics Research Centre

March 2009

UNIVERSITY OF Southampton

UNIVERSITY OF SOUTHAMPTON

ABSTRACT

FACULTY OF ENGINEERING, SCIENCE AND MATHEMATICS
OPTOELECTRONICS RESEARCH CENTRE

Doctor of Philosophy

DEVELOPMENT OF HOLLOW-CORE PHOTONIC BANDGAP FIBRES FREE OF SURFACE MODES

by Rodrigo Amezcua Correa

Conventional optical fibres can only guide light in a high refractive index core by total internal reflection. By using total internal reflections it is not possible to guide light in an air core. Light guidance in air is of great interest for various technological and scientific applications and has only recently been possible with the advent of photonic band gap fibres. However, the transmission performance of silica/air hollow-core photonic bandgap fibres has until now been affected by the existence of surface modes. These surface modes couple with the air-guided mode in specific spectral ranges inside the bandgap simultaneously increasing the attenuation and dispersion of the air-guided mode and reducing the useable bandwidth of the fibre. Therefore, for many applications it is important to eliminate surface modes or at least reduce their impact on the air mode.

The aim of this thesis is to gain a profound insight into ways of reducing the density of surface modes and ways of tuning their wavelength out of the bandgap in order to minimize their impact on the air mode. A complete numerical study of the effects that variations of the core geometry have on the fibre's transmission properties is presented in this thesis. In particular, it is found that reducing the thickness of the glass wall that surrounds the core, can simultaneously suppress surface modes interference and reduce the fibre attenuation. The proposed core designs have a core wall just half the thickness of the thinnest features of the cladding -this is approximately 50 nm thinner than in previous designs.

The fabrication of the first hollow-core photonic bandgap fibre with no surface modes is presented in this thesis. The fibre has state-of-the-art attenuation over the full spectral width of the bandgap. As a result of the elimination of surface modes the fibre presents increased bandwidth, reduced dispersion and dispersion slope compared to previous hollow-core photonic bandgap fibers. These advances have been possible due to the development of a modified fabrication method which makes the production of low-loss hollow-core fibers both simpler and 5 to 6 times quicker than previously. This development makes hollow-core fibres with improved performance more readily available than ever before.

Declaration of Authorship

I, Rodrigo Amezcua Correa, declare that this thesis entitled:

DEVELOPMENT OF HOLLOW-CORE PHOTONIC BANDGAP FIBRES FREE OF SURFACE MODES

and the work presented in it are my own. I confirm that:

- This work was done wholly or mainly while in candidature for a research degree at this University
- Where any part of this thesis has previously been submitted for a degree or any other qualification at this University or any other institution, this has been clearly stated
- Where I have consulted the published work of others, this is always clearly attributed
- Where I have quoted from the work of others, the source is always given. With the exception of such quotations, this thesis is entirely my own work
- I have acknowledged all main sources of help
- Where the thesis is based on work done by myself jointly with others, I have made clear exactly what was done by others and what I have contributed myself

Rodrigo Amezcua Correa

March 2009

Contents

List of Figures

List of Tables

Nomenclature and Abbreviations

c	Speed of light, $c = 2.998 \times 10^8\,\mathrm{m/s}$
i	Imaginary unit number, $i = \sqrt{-1}$
μ_0	Vacuum magnetic permeability, $\mu_0 = 4\pi \times 10^{-7}\,\mathrm{H/m}$
ε_0	Vacuum dielectric permittivity, $\varepsilon_0 = 8.85 \times 10^{-12}\,\mathrm{F/m}$
$\vec{E}$	Electric field
$\vec{H}$	Magnetic field
$\vec{D}$	Electric flux density
$\vec{B}$	Magnetic flux density
$\vec{J}$	Current density
$\vec{r}$	Spatial vector
t	Time
ρ	Charge density
σ	Conductivity
υ	Frequency
ω	Angular frequency, $\omega = 2\pi\upsilon$
λ	Wavelength
Λ	Pitch
ε	Dielectric permittivity, $\varepsilon = \varepsilon_1 + i\varepsilon_2$
ϵ	Relative dielectric permittivity, $\epsilon = \epsilon_1 + i\epsilon_2$
n	Refractive index, $n = n_1 + in_2$
n_{eff}	Effective mode index, $n_{eff} = \beta/k$
k	Wave vector, $k = k_1 + ik_2$
DOS	Density Of States
TE	Transverse Electric
TM	Transverse Magnetic
FEM	Finite Element Method
FM	Fundamental Mode
FSM	Fundamental Space lling Mode
GVD	Group Velocity Dispersion
HC-PBGF	Hollow-core Photonic Bandgap Fibre

HOM	High Order Mode
MOF	Microstructured Optical Fibre
PBG	Photonic Bandgap
PBGF	Photonic Bandgap Fibre
PC	Photonic Crystal
PCF	Photonic Crystal Fibre
PWEM	Plane Wave Expansion Method
SM	Surface Mode
SEM	Scanning Electron Microscopy
ZDW	Zero Dispersion Wavelength

Acknowledgements

I would firstly like to thank my supervisors Neil Broderick and David Richardson for all the ideas, support and guidance over the three and a half years that I spent working with them. Thanks Neil for your friendship and the cups of coffee that helped me to write this thesis.

Many people have contributed to this work. Francesco, Joanne, Vittoria, and Adriaan, thank you all for very encouraging discussions. I would also like to thank many friends from the ORC, especially: Francesca, Everardo, Pier, Anna, Lionel, Luis, Paulo, Rob and Francesco. Many thanks go to Eve Smith, the ORC student coordinator, for helping me in every situation and reminding me of the deadline to submit this thesis!

I would like to acknowledge my sponsor, CONACyT (National Council for Science and Technology of Mexico), for giving me the opportunity to study at the ORC.

I have really enjoyed this time in Southampton thanks to my housemates and friends: Vladis, Symos, Greg, Helene, Nav, Andy and Arturo. Thanks also go to Ely and Liber for coming all the way from Mexico. I would like to thank Juan Carlos, Mauricio, Rogelio, Gustavo, and Julian the greatest friends one could have.

Thanks to my family for the loving environment in which I grew up. My brothers Adrian and Mariano for being there and for never letting me feel that I am away from them.

I wish to thank my parents who truly inspired me, supported me, taught me, and loved me.

Finally, special thanks to Catia. I am fortunate to have met you and share this time with you.

A mis padres, Paty y Miguel

“”

Chapter 1

Introduction

The fact that modern optical fibres transmit information over long distances at exceptionally high speed rates is a truly fantastic technological and scientific achievement of the last century. Everyday we all use optical fibres when making telephone calls, connecting to the internet, and reading our e-mails. Currently, optical fibres are increasingly been used in non-telecommunications applications such as: structural sensing, biomedicine, medical imaging, astronomy and micro-machining, among many other fields. Conventional optical fibres are formed from two different glasses. One with a higher refractive index runs down the middle of the fibre, forming the core in which light is trapped. A second lower-index glass surrounds the inner rod, protecting it and forming the cladding of the fibre. The inner rod has to have a higher refractive index than the outer, because only then light can be guided in the core by total internal reflections at the core-cladding boundary. Recently, a novel type of optical fibres was envisioned by Philip Russell [1, 2]. These new fibres, known as photonic crystal fibres, can be made entirely from a single material as they do not rely on dopants for light guidance. Instead, the cladding region in photonic crystal fibres has wavelength-scale holes running down the fibre length. The discovery of photonic crystal fibres has been very promising for optical fibre technology since they have enabled light to be controlled in ways not previously possible or even imaginable with conventional optical fibre technology [2].

Research on single material fibres dates back to the early years of fibre optics in the 1970's. At that time, Kaiser *et al.* [3, 4] fabricated a single material fibre consisting of a small diameter silica rod supported by thin struts inside a large tube, Figure 1.1a. Their motivation was to overcome the difficulties in having different chemical compositions required for the core and cladding materials. The development of chemical vapour deposition (CVD) for optical fibre fabrication also in the 1970's overcame such negative effects providing high purity ulta-low loss synthetic silica [5, 6]. CVD also permitted to precisely control the refractive index of silica by the introduction of index increasing

dopants (germanium, aluminium) and index decreasing dopants (boron, fluorine)[7, 8]. The promising capabilities of CVD for making single-mode low-loss optical fibres [9] left single-material fibres research aside for many years. Russell's idea of light guidance in a hollow-core by surrounding it with a large number of smaller holes in order to form a synthetic material which would trap light by using a photonic bandgap, renewed the interest in single material optical fibres [10, 1, 11]. The fabrication of an only-silica photonic crystal fibre in 1996 by Knight *et al.* [12] containing hundreds of air channels of micrometer dimensions forming a two-dimensional photonic crystal around a silica core, Figure 1.1(b), which was single mode over a very wide spectral range, led to the discovery of endlessly single-mode PCFs by Birks *et al.* [13]. This seminal work in photonic crystal fibres fueled the ambition that they would support the growing demands on the performance and functionality of optical fibres. The unusual modal properties of this fibre burst the activities on photonic crystal fibre research.

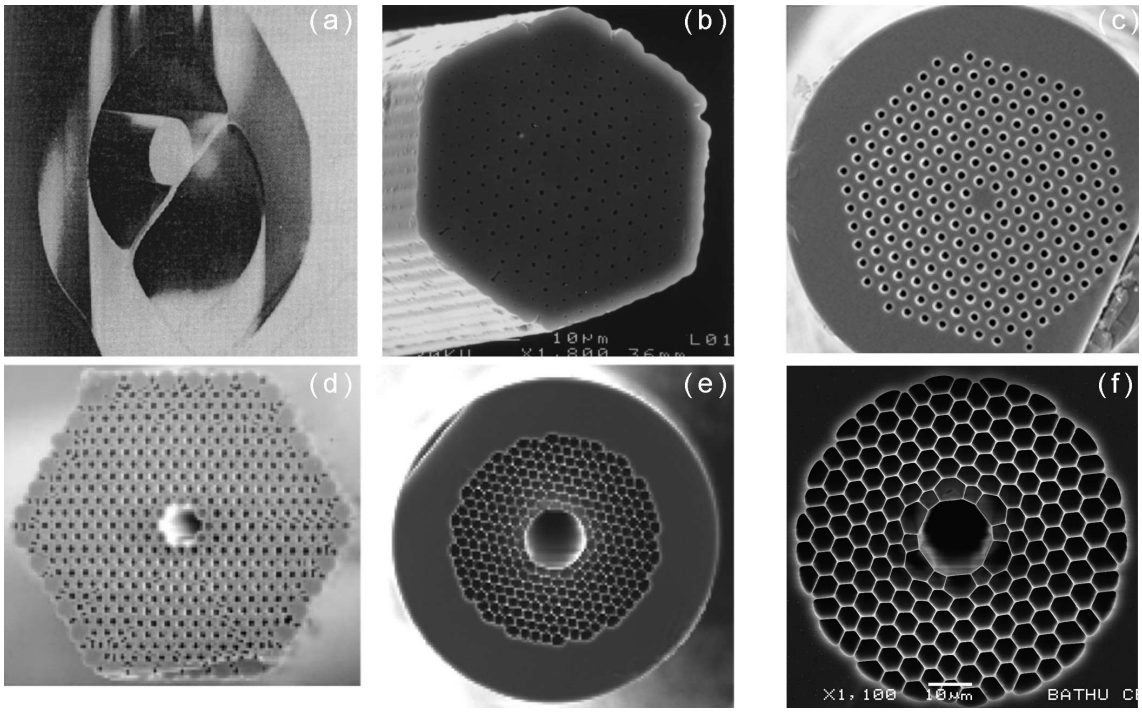

FIGURE 1.1: Examples of index guiding PCFs (top) and photonic bangap fibres (bottom). (a) First demonstration of a silica-only fibre by Kaiser *et al.* in 1973 [3]. (b) Scanning electron microscope (SEM) image of the first photonic crystal fibre with a silica core surrounded by a periodic array of air holes in silica by Knight *et al.* in 1996 [12]. (c) Endlessly single-mode PCF fabricated at the ORC. (d) SEM micrograph of the first hollow-core PCF by Cregan *et al.* in 1999 [14]. (e) SEM micrograph of the lowest loss hollow-core bandgap fibre by Blazephotonics [15]. (f) Hollow-core PCF by Amezcua *et al.* in 2008 [16].

There are two major classes of photonic crystal fibres depending on their guidance mechanism: *index guiding photonic crystal fibres*, which guide light due to a "reduced" refractive index of the cladding region and *photonic bandgap fibres*, which confine light

thanks to photonic bandgaps formed by the cladding. Although fibres belonging to these two classes have been fabricated of different materials and with several cladding configurations, the fibres of interest for this work have a two-dimensional photonic crystal cladding formed by an array of air holes in silica that run down the full fibre length, Figure 1.1.

Index-guiding PCFs consist of a solid core surrounded by an array of air holes, Figure 1.1(b)(c). In this case, the air holes can be seen as to lower the effective refractive index of the cladding region as compare to that of the solid core and guidance occurs by a modified total internal reflection mechanism. Although this mechanism is similar to the way in which conventional optical fibres guide light, the wavelength scale features of the fibre lead to a strongly wavelength dependent cladding index leading to a host of unusual optical properties unique to photonic crystal fibres, including single-mode guidance at all wavelengths and striking nonlinear and dispersive properties [12, 1, 17, 2, 18, 19, 20, 21, 22, 23].

In contrast to index guiding PCFs, in which the guidance mechanism is conceptually similar to that of conventional fibres, photonic bandgap fibres guide light by a completely radical concept: photonic bandgap effects. In photonic bandgap fibres the air holes that define the cladding region have to be arranged in a highly perfect periodical lattice. For certain geometries, the cladding can then form two-dimensional photonic bandgaps which prohibit the propagation of light for specific frequencies and propagation constant values [10]. By breaking the order of the cladding (adding a defect in the periodic structure), it is possible to introduce localized modes within the defect. This is typically done by introducing a bigger hole at the centre of the structure. If light can propagate in the defect but its frequency lies within a bandgap it will not be allowed to propagate in the cladding and therefore the optical energy will be concentrated in the core and guided with low-loss. Hollow-core photonic bandgap fibres (HC-PBGFs) are a special class of bandgap fibres that guide light in an air core. In 1999, Cregan *et al.* [14] demonstrated the first HC-PBGF and over the past decade they have been developed to high-performance products, Figure 1.1. Indeed, now fibres with very low attenuation -well below than 20 dB/km at 1550 nm wavelength- are readily available and the best loss value in a hollow-core fibre is only 1.2 dB/km [15] which is around 10 times higher than the minimum attenuation of $\sim$0.15 dB/km in conventional fibres [24].

1.1 Thesis Structure

The work in this thesis is mainly related to the development of silica hollow-core photonic bandgap fibres with a broad low-loss transmission window by eliminating surface

modes which lie within the bandgap . It comprises various computational and fabrication experiments performed by the author over his PhD. The topics span from the analysis of the modal properties of PBGFs and the design of hollow core fibres with improved transmission performance, to the fabrication and characterization of fibres based on the optimized designs. The design of hollow-core photonic bandgap fibres free of surface modes was carried out by the author during the first 4 years of his PhD at the Optoelectronics Research Centre. Based on these results, hollow-core fibres incorporating a novel core design were fabricated over the last year at the Centre for Photonics and Photonic Materials at the University of Bath, while the author was employed there as a researcher. The fabrication and characterization of these fibres has been included in the thesis in order to confirm the theoretical predictions and prove that the fabrication of the proposed designs is indeed feasible. The thesis is partitioned in 9 chapters as outlined below.

Chapter 2 provides an introduction to photonic crystal fibres, including a description of the stack and draw technique used for the fabrication of silica PCFs. It also includes a comprehensive description of the optical properties of photonic crystals and the optical properties of index-guiding PCFs are briefly discussed.

Chapter 3 is an introduction to hollow core photonic bandgap fibres with the aim of describing the bandgap guiding mechanisms and to provide an intuitive explanation of the optical properties of this type of waveguide. Due to their complex structure, modelling HC-PBGFs is not an straight forward task and several methods are normally used for studying them. The numerical methods used through this project for analyzing HC-PBGFs are briefly described in this chapter. A literature review of the development of HC-PBGFs is also included.

The main objective of chapter 4 and chapter 5 is the design of HC-PBGFs which do not support surface modes within the bandgap and therefore present a broad transmission window. For this task the modal properties of the fibres as a function of the core structure are numerically calculated using a finite element method. All the computational programs, numerical calculations and the analysis of results presented in these chapters were done by the author. In chapter 4 fibres featuring a 7 cell core are analyzed. Contour plots summarizing the evolution of the transmission properties of hollow core bandgap fibres as a function of the core size and the thickness of the core/cladding interface are presented. These contour plots are an original way of analyzing bandgap fibres and they clearly show the dependence between surface modes and core geometry. In particular, it is shown that by carefully choosing the thickness of the core surround then surface modes can be eliminated. The advantages and disadvantages of having different core/cladding interfaces are also discussed.

Chapter 5 extends the study presented in chapter 4 to fibres featuring a larger core (19 cell) and a higher air filling fraction in the cladding. It is shown that the design regime found for 7 cell fibres is also valid for larger cores. Finally, ways of modifying the group velocity dispersion in HC-PBGFs are studied in this chapter.

Chapter 6 deals with the fabrication of HC-PBGFs based on the designs studied in chapters 4,5. The fabrication and characterization of the fibres was carried out at the Centre for Photonics and Photonics Materials of the University of Bath by the author in collaboration with Dr. Frédéric Gérôme, Dr. Sergio Leon-Saval, Prof. Tim Birks, and Prof. Jonathan Knight. The fibres presented here incorporate a thin core wall which eliminates the impact of surface modes enabling for the first time air guidance in a hollow-core fibre with low attenuation over the full bandgap of the photonic crystal cladding. These fibres also present the lowest dispersion slope yet reported for any hollow-core photonic bandgap fibre.

Chapter 7 describes a different type of hollow-core waveguide - Kagome fibre. The author uses the finite element method to numerically study the modal structure of the Kagome fibres with the aim of understanding their guidance mechanisms.

Chapter 8 looks at understanding a specific type of high order modes supported in large mode area index guiding photonic crystal fibres which cannot be explained by index guidance arguments. It is found that these modes exist in low density of states regions and/or bandgaps formed in the cladding. The contribution from the author to this work was on the calculation of the density of states of the different fibres while most of the work was done by Dr. Joanne Flanagan.

Chapter 9 summarizes the major results of this research work and discusses future directions.

Chapter 2

Photonic Crystal Fibres

It is important to mention that *photonic crystal fibres* are also referred as *microstructured optical fibres* and *holey fibres*. In a large part of literature all these names are given to all types of fibres with microscale features defining their transverse profile. In a conventional optical fibre the light propagation is due to total internal reflection at the core/cladding interface. In contrast to this, PCFs are able to guide light by means of two different mechanisms: *Modified total internal reflection*, in which light is guided in a solid core, surrounded by a (not necessarily periodic) structured cladding. In this case the average refractive index of the cladding is decreased because of the air holes (low refractive index) [12]. On the other hand, *photonic bandgap fibres* exploit two-dimensional photonic bandgaps as the mechanism of light guidance therefore they can guide light in a low refractive index medium [10, 25, 14]. In photonic bandgap fibres the air holes that define the cladding region are arranged in a periodic lattice which presents a photonic band gap that does not allow light to propagate in the cladding region under certain conditions.

A good starting point for understanding the properties of photonic crystal fibres is that of photonic crystals. This chapter gives an insight into photonic crystal and the formation of photonic bandgaps. A comprehensive review of the optical properties, guidance mechanisms and fabrication methods of photonic crystal fibres is also presented here.

2.1 Fundamentals of photonic crystals

The periodic structure of atoms within a conducting medium gives rise to different electronic bands, allowing the control of the propagation of electrons through the material [26, 27]. This has been understood for many years, and ultimately has led to personal computers. However, it was not until 1987 when Yablonovitch [28] and John [29] proposed an analogous system to control the propagation of light. The optical version of a solid state crystal, a photonic crystal, is made from dielectric materials periodically patterned on the wavelength scale. Photonic crystals were predicted theoretically to describe two new optical principles, the localization and trapping of light [29, 30] and the complete inhibition of spontaneous emission [28]. In photonic crystals the periodical refractive index distribution can give rise to bandgaps in the dispersion relations of electromagnetic waves. Then propagation of light within these bandgaps is forbidden and thus photonic crystals allow for a fine degree of control over the optical field within a material giving new opportunities in quantum optics, optoelectronics and nonlinear optics [31].

2.1.1 Theoretical description of photonic crystals

The basic starting point in understanding the optical properties of photonic crystals is that of Maxwell's equations. An electromagnetic wave can be expressed in terms of an electric field vector $\vec{E}$ and a magnetic field vector $\vec{B}$. When incident on a material the terms $\vec{H}$, the magnetic flux density, $\vec{D}$ the electric displacement vector, $\vec{J}$ the current density and ρ the charge density are also defined. The Maxwell's equations in the differential form may be expressed in the International System units as:

$$\nabla \times \vec{E}(\vec{r},t) = -\frac{\partial \vec{B}(\vec{r},t)}{\partial t}\,, \tag{2.1a}$$

$$\nabla \times \vec{H}(\vec{r},t) = \frac{\partial \vec{D}(\vec{r},t)}{\partial t} + \vec{J_{free}}\,, \tag{2.1b}$$

$$\nabla \cdot \vec{B}(\vec{r},t) = 0\,, \tag{2.1c}$$

$$\nabla \cdot \vec{D}(\vec{r},t) = \rho_{free}\,. \tag{2.1d}$$

Considering a number of assumptions valid for our particular case the previous equations can be simplified. First, for a medium that is free of free charges and free currents, ρ_{free} and $\vec{J_{free}}$ are set to zero. Next, if the field strengths are assumed to be small enough, the relations $\vec{D}$ to $\vec{E}$ and $\vec{B}$ to $\vec{H}$ can be consider as linear. Finally, for isotropic loss-less

materials the dielectric permittivity, $\varepsilon(\vec{r},\omega)$[1], is scalar and real; where $\vec{r}$ is the spatial vector and ω is the angular frequency of light. Then, the constitutive equations of the material, are given by:

$$\vec{D}(\vec{r},t) = \varepsilon(\vec{r})\vec{E}(\vec{r},t)\,, \tag{2.2a}$$
$$\vec{B}(\vec{r},t) = \mu_0\vec{H}(\vec{r},t)\,, \tag{2.2b}$$

where μ_0 is the magnetic permeability of vacuum. If harmonic time dependence of the electromagnetic fields is assumed, the fields can be written as,

$$\begin{aligned}\vec{E}(\vec{r},t) &= \vec{E}(\vec{r})e^{i\omega t}\,,\\ \vec{H}(\vec{r},t) &= \vec{H}(\vec{r})e^{i\omega t}\,.\end{aligned} \tag{2.3}$$

By the substitution of equations (2.2) into equations (2.1) the following system is obtained

$$\nabla\times\vec{E}(\vec{r}) = -i\omega\mu_0\vec{H}(\vec{r})\,, \tag{2.4a}$$
$$\nabla\times\vec{H}(\vec{r}) = i\omega\varepsilon(\vec{r})\vec{E}(\vec{r})\,, \tag{2.4b}$$
$$\nabla\cdot\vec{H}(\vec{r}) = 0\,, \tag{2.4c}$$
$$\nabla\cdot(\varepsilon(\vec{r})\vec{E}(\vec{r}) = 0 \tag{2.4d}$$

Equation (2.4a) and equation (2.4b) can be rearranged into a single vectorial expression satisfied by the magnetic field $\vec{H}(\vec{r})$

$$\nabla\times\frac{1}{\varepsilon(\vec{r})}\left(\nabla\times\vec{H}(\vec{r})\right) = \omega^2\mu_0\vec{H}(\vec{r}) \tag{2.5}$$

This general expression represents an eigenvalue problem that together with the divergence equation (2.4c) govern the response of an optical field in a dielectric medium whose dielectric constant distribution is given by $\varepsilon(\vec{r})$. If the spatial dependence of the dielectric constant of any medium is known, the solutions to equation (2.5) will provide

[1]Lossy materials can be easily consider by adding an imaginary part to the dielectric permittivity.

the solutions to the optical modes. However, the complex geometry of photonic crystals makes the solution of this equation non-trivial and, outside of the simplest cases, requires a fair amount of computational work to provide answers. The left side of equation (2.5) can be formulated as an operator Θ acting on $\vec{H}(\vec{r})$ so that it takes explicitly the form of an eigenvalue problem,

$$\begin{aligned} \Theta\vec{H}(\vec{r}) &= \omega^2\mu_o\vec{H}(\vec{r})\,, \\ \Theta &\equiv \nabla\times\left(\tfrac{1}{\varepsilon(\vec{r})}\nabla\times\right) \end{aligned} \tag{2.6}$$

Similarly to equation (2.5), a master equation for $\vec{E}$ could also be formulated, however it is more convenient to express the problem in terms of $\vec{H}(\vec{r})$. This is because the operator Θ is *Hermitian* which simplifies the computational problem [32]. After obtaining the modes $\vec{H}(\vec{r})$ for a given frequency, the following relation can be used to obtain the electric field distribution,

$$\vec{E}(\vec{r}) = \left(\frac{-i}{\omega\varepsilon(\vec{r})}\right)\nabla\times\vec{H}(\vec{r}) \tag{2.7}$$

In optical fibres, the translational invariance of the refractive index profile along the z-direction leads to the following form of solutions for equation (2.5)

$$\vec{H}(x,y,z) = \vec{\mathbf{H}}(x,y)e^{-i\beta z} \tag{2.8}$$

where β is the propagation constant along z (the fibre axis). The harmonic mode $\vec{\mathbf{H}}(x,y)$ is the eigenvector associated to the eigenvalue β. In the case of a wave propagating in a homogeneous medium ($\varepsilon(\vec{r}) = \varepsilon$) equation (2.5) reduces to the Heltmholtz equation, which can be solved in a closed form. In the same manner, if the geometry of the system is simple enough to apply analytical boundary conditions at the interfaces, the electromagnetic problem can also have an analytical solution. This is the case of conventional step-index fibres. However, in the case of photonic crystal fibres the eigenvalue problem is more complicated due to the fibre's complex geometry and analytical solutions are usually impossible to obtain. Powerful numerical methods are used to obtain the eigenvectors and eigenvalues of the electromagnetic problem. Nevertheless, when analyzing infinite structures, the periodic nature of a photonic crystal allows the simplification of the electromagnetic problem to a small region of the photonic crystal.

Photonic crystals can be described in terms of a periodic array of points in space called a *lattice*, and a unit cell which is repeated identically at every point of the lattice. The unit cell is defined as the smallest area, which by mere translations can fully represent

the structure. Every point of the lattice can be defined in terms of the *lattice vectors* $(\vec{u_1}, \vec{u_2}, \vec{u_3})$, which are the smallest vectors that can connect one lattice point with another. All crystals have an associated lattice in Fourier space called *reciprocal lattice* which consists of the set of all the allowed terms in the Fourier expansion of the periodic structure. This lattice is defined in terms of the *primitive reciprocal lattice vectors* $(\vec{g_1}, \vec{g_2}, \vec{g_3})$ [27, 33, 32].

To examine the way a photonic crystal affects the propagation of light passing through it, the dielectric constant of the structure must be expressed in terms of the lattice vector $\vec{R}$. The periodic dielectric function of a photonic crystal satisfies $\varepsilon(\vec{r}) = \varepsilon(\vec{r}+\vec{R})$. According to Bloch's theorem, the solutions of the magnetic field can be expressed as Bloch's states consisting of a plane wave modulated by a periodic function with the same periodicity as the photonic crystal,

$$\vec{H}_k(\vec{r}) = \vec{U}_k(\vec{r})e^{i\vec{k}\cdot\vec{r}} \tag{2.9}$$

where $\vec{k}$ is the wave vector, $\vec{r}$ denotes the position vector and $\vec{U}_k(\vec{r})$ has the same periodicity as the lattice, i.e. $\vec{U}_k(\vec{r}) = \vec{U}_k(\vec{r}+\vec{R})$. Therefore, knowing the values of the magnetic field $\vec{H}_k$ in a unit cell, the magnetic field in all the structure can be inferred from equation 2.9. In other words, the electromagnetic problem in an infinite photonic crystal is reduced to finding the values of the magnetic field (2.5) in a small area. In the same way, in the reciprocal lattice, a Bloch state for a wave vector $\vec{k}$ is equal to the Bloch state $\vec{k}+\vec{G}$, where $\vec{G}$ is any vector of the reciprocal lattice. This gives rise to a periodicity of the dispersion curve in the reciprocal space (or $\vec{k}$-space), expressed as $\omega(\vec{k}) = \omega(\vec{k}+\vec{G})$. Consequently, the dispersion information of the modes is contained in a region of the reciprocal space called the *Brillouin zone* and only wave vectors $\vec{k}$ lying inside the Brillouin zone identify an independent mode. Therefore the dispersion curves of a photonic crystal are normally presented as plots of frequency versus wavevectors in the Brillouin zone. In the following section an intuitive approach to understanding the optical properties of photonic crystals is discussed.

2.1.2 One Dimensional Photonic Crystals

A schematic illustration of a 1-dimensional photonic crystal is shown in Figure 2.1(a), the system is a periodic arrangement of layers of two different dielectric materials. The system is repeated in the z-direction with period Λ which is of the order of the wavelength of light. A plane wave traveling along the line of periodicity will be scattered at the crystal interfaces every distance Λ. This will give rise to forward and backward propagating waves which will interfere to form standing waves within the structure. The

system can also be viewed in the k-space as a line of scattering points with separation equal to the reciprocal lattice vector $G = 2\pi/\Lambda$. This implies that a mode with wave vector k_0 has the same dispersion and, thus, couples with a mode with wave vector $k_0 \pm nG$, forming a new state which is strongly linked to the structure.

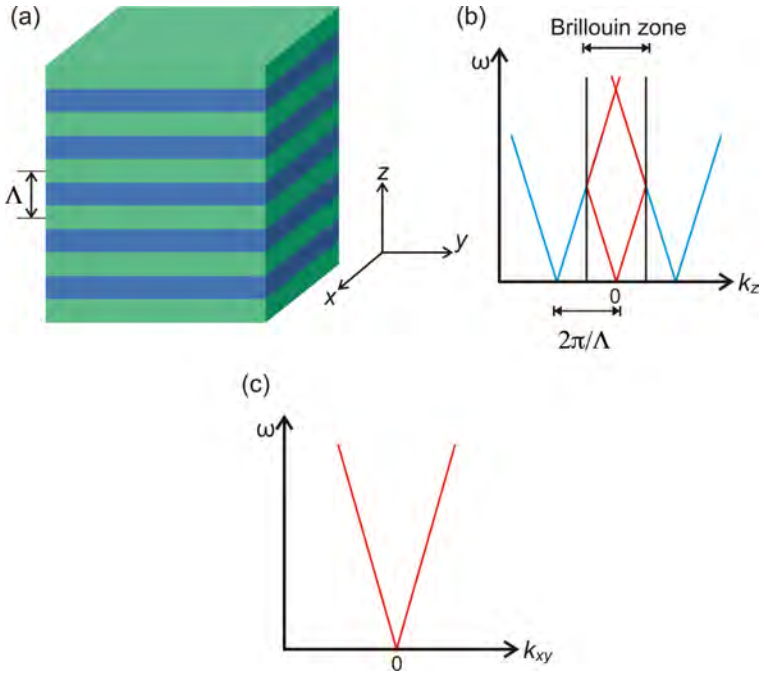

FIGURE 2.1: Illustration of a 1-dimensional photonic crystal with period Λ and reciprocal lattice vector G. Schematic plots of the dispersion relations of plane waves propagating in the photonic crystal in the z-direction and on the xy plane, (b) and (c) respectively.

The dispersion of light propagating in an isotropic medium is given by:

$$\omega(k) = \frac{ck}{\sqrt{\epsilon_d}} = \frac{ck}{n}\,, \tag{2.10}$$

where c is the speed of light in vacuum, $\epsilon_d = \varepsilon_d/\varepsilon_0$ is the medium's relative dielectric permittivity, and n is its refractive index. This dispersion relation indicates that the energy of light changes linearly with the momentum (k) and zero energy corresponds to zero momentum. Now allow a plane wave to propagate in a 1D photonic crystal in the z-direction, crossing the layers of dielectric at normal incidence, see Figure 2.1(a). In this case, $k_{xy} = 0$ and therefore, only the wave vector in the propagation direction (k_z) will determine the dispersion properties. Due to the periodicity in the *k_space* the point $k_z = 0$ can be defined at all the scattering points ($k_z = \pm nG$). This allows to repeat the dispersion relation given by equation (2.10) at all the scattering points $k_z = \pm nG$, blue lines in Figure 2.1(b).

As it is shown in Figure 2.1(b), when the first band $\omega = \pm ck/n$ (red lines), reaches the edges of the Brillouin zone it is translated back into the zone and is named as second band $\omega = \frac{c}{n}(k_0 + G)$ and $\omega = -\frac{c}{n}(k_0 - G)$. This shows that the optical modes fold back on themselves as they reach the Brillouin zone. This folding arises from the scattering of neighbouring sites ($k_z = \pm G$) and leads to very different optical properties for a periodic material compared to an isotropic medium.

Figure 2.1(c) shows the dispersion relations of a wave propagating in the xy-plane, in this case the dispersion is simply that of light propagating in a isotropic medium. The schematic shown in Figure 2.1(b) considers the weak scattering approximation, a condition that assumes no interaction between the dispersion bands from different lattice sites. The weak scattering approximation is limited to structures where the difference in the dielectric constant between the layers is small. When the refractive index difference is large the weak scattering approximation is not valid and one must solve equation (2.6) to obtain the optical modes in the structure.

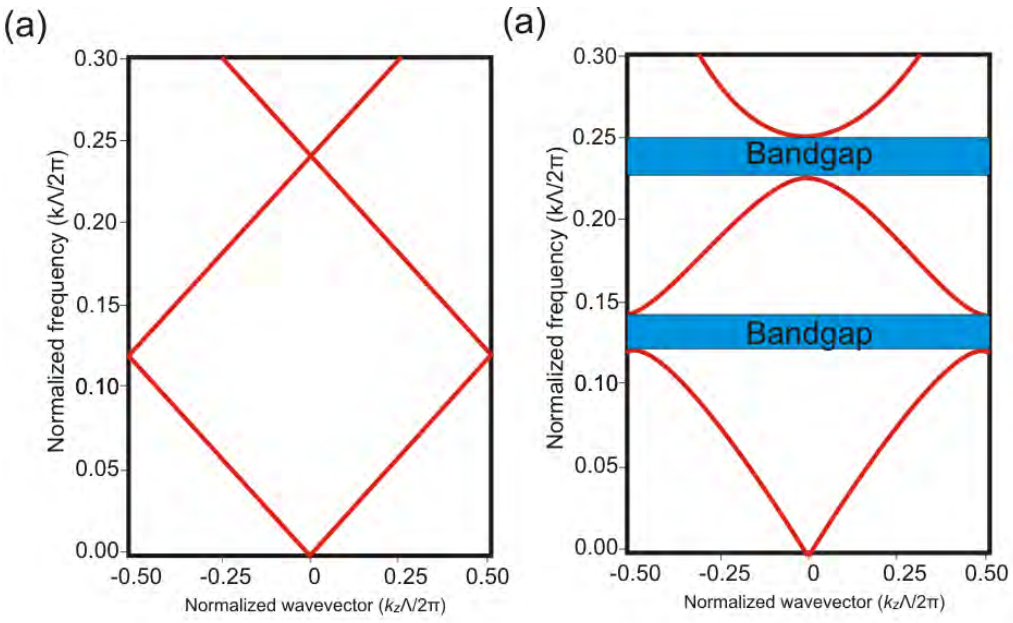

FIGURE 2.2: Dispersion relation of light propagating along a periodic dielectric structure, with dielectric contrast difference between the layers of zero and three for (a) and (b) respectively. These curves are obtained by solving equation (2.6).

The dispersion relations of two different 1D photonic crystals calculated by solving equation (2.6) are shown in Figure 2.2. When light propagates in a structure where both dielectric regions have the same refractive index n (a single slab of material) its dispersion curve is just the *dielectric line* given by equation (2.10), see Figure 2.2(a). Conversely, Figure 2.2(b) plots the dispersion of light propagating through a 1D photonic crystal where the dielectric layers have a difference in dielectric constant of 3. The blue shaded areas show that there are frequency regions where optical modes do not exist at all. These

regions are call photonic bandgaps. For a physical description of the bandgap formation it is useful to consider the electric field distribution directly above and below the first gap, which as seen in Figure 2.2(b) occurs at the edge of the Brillouin zone, at $k = \pi/\Lambda$. At this position, the optical modes correspond to standing waves with wavelengths equal to twice the crystal lattice constant 2Λ. There are only two electric field distribution (for the first two bands), that form standing waves and satisfy the boundary conditions and the symmetry of the system. For the first solution the maximum intensity is located at high refractive index layers while the second one is concentrates in the low dielectric constant layers, (see Figure 2.3). Therefore, it becomes clear that these two modes have different effective mode indices. The dispersion curve also shows that both modes have the same wave vector ($k = \pi/\Lambda$) and hence the same wavelength. However, the mode concentrated in the high refractive index material experiences a greater effective index and, thus, a lower frequency than the mode concentrated in the low refractive index material. This difference in frequency provides the energy gap between the high and low index bands in the photonic crystal, analogous to the valence and conduction band in a semiconductor. It is important to note that band gaps always appear in one-dimensional photonic crystal for any dielectric constant difference. And as the refractive index contrast increases the band gap widens.

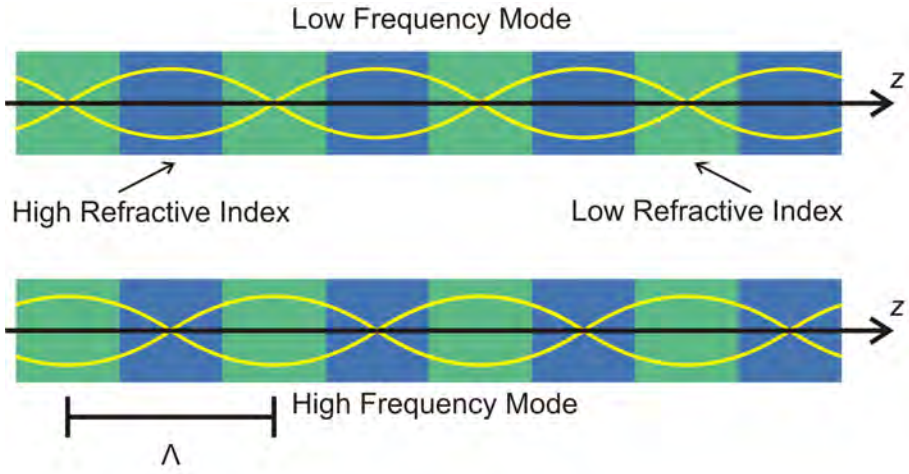

FIGURE 2.3: Distribution of the electric field in a one-dimensional photonic crystal. For both modes $k_{trans} = 0$ however, the mode localized in the high refractive index regions has a lower frequency than the mode which concentrated in the low refractive index regions.

One dimensional photonic crystals are widely used in many optical devices where the transmission of light for certain frequencies needs to be suppressed, light within this range will be reflected very efficiently. Examples of 1D photonic crystals are fibre Bragg gratings, widely used in optical telecommunication systems, Bragg filters for diode lasers, antireflection coatings, etc.

2.1.3 Two Dimensional Photonic Crystals

Two dimensional photonic crystals have a periodic pattern in the xy-plane while remain constant in the z-direction. These structures can be designed to have a photonic band gap for light propagating in the structured plane. In a similar way to the one-dimensional case, to qualitatively understand the dispersion properties of two-dimensional photonic crystals one can use the weak-scattering approximation. For the specific type of photonic crystals of interest in this thesis, photonic crystal fibres, the structure can be represented as a closed packed array of scattering sites (holes) arranged in a triangular lattice, see Figure 2.4(a). In this case the primary lattice vectors are equal in length at a 60° angle to each other, and can be chosen as follows:

$$\vec{R_1} = \frac{\Lambda}{2}\left(\vec{x} + \vec{y}\sqrt{3}\right) , \tag{2.11}$$

$$\vec{R_2} = \frac{\Lambda}{2}\left(\vec{x} - \vec{y}\sqrt{3}\right) . \tag{2.12}$$

The scattered light off the surface may be obtained by taking the Fourier transform of the lattice and the first set of scattered modes corresponds to those of one lattice vector, of which there are six solutions. By taking the Fourier transform of the crystal it is found that the lattice in k-space also forms a triangular lattice rotated 30° with respect to the real-space lattice, as depicted in Figure 2.4(b).

The reciprocal lattice vectors $\vec{G_1}$ and $\vec{G_2}$ are related to the real space lattice vectors by

$$\vec{R_i} \cdot \vec{G_j} = 2\pi\delta_{ij}, i, j = 1, 2 , \tag{2.13}$$

where δ_{ij} is the Dirac delta function. The reciprocal lattice vectors can be written as follows:

$$\vec{G_1} = \frac{2\pi}{\Lambda}\left(\vec{x} + \vec{y}\frac{\sqrt{3}}{3}\right) , \tag{2.14}$$

$$\vec{G_2} = \frac{2\pi}{\Lambda}\left(\vec{x} - \vec{y}\frac{\sqrt{3}}{3}\right) . \tag{2.15}$$

The angle between the lattice vectors of the real- and k-space is also 30°. The irreducible Brillouin zone corresponding to a six-fold symmetric unit cell is illustrated as the black area in Figure 2.4(b). The high symmetry points of the reciprocal lattice are labelled Γ, **M**, and **K**. As in the 1D case, the dispersion relation of a 2D photonic crystal can be obtained by drawing the dispersion of light from each scattering point (weak scattering approximation). However, in this case the visualization is more complicated than in

the 1D case and thus not very practical. For the purposes of this chapter it is more convenient to obtain the dispersion relations by solving the master equation.

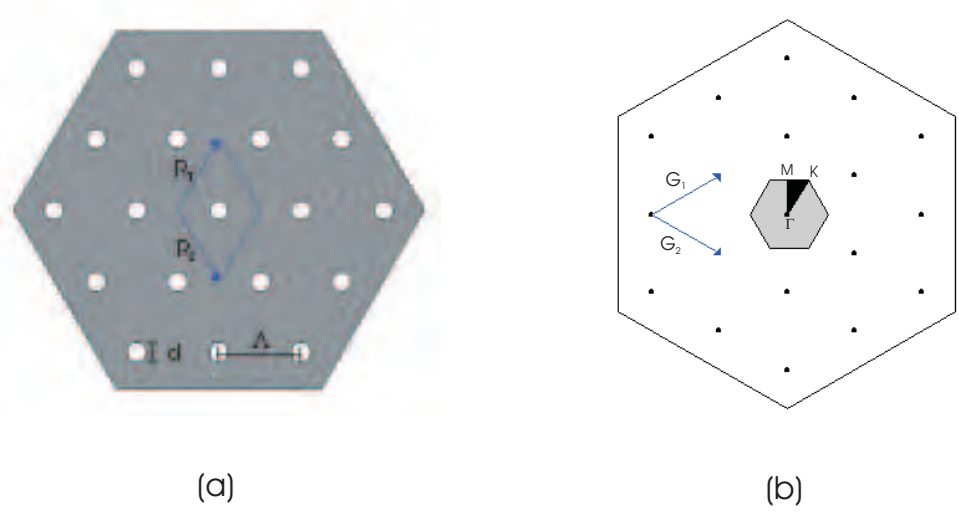

FIGURE 2.4: (a) Triangular lattice of circular holes, real space primitive vectors $\vec{R_1}$ and $\vec{R_2}$. The area inside the blue lines is the unit cell. (b) The crystal can be represented in the k-space as a triangular lattice of scattering points with corresponding reciprocal lattice vectors $\vec{G_1}$ and $\vec{G_2}$. The shaded hexagon is the Brillouin zone, the irreducible Brillouin zone is the darker area. The marked points in the Brillouin zone are conventionally known as Γ, M and K.

As photonic crystal fibres are invariant along the fibre axis (z), from equation (2.8) the optical modes can be written as:

$$\vec{H}(\vec{r}) = \vec{H}(\vec{r}_t)e^{-i\beta z}\,, \tag{2.16}$$

where $\vec{r}_t$ is the transverse component of the position vector $\vec{r}$, $\beta = k_z$ is the propagation constant (axial component of the wavevector). β is conserved across every region of the structure. The optical modes $[\vec{H}(\vec{r}_t)]$ of the structure can be calculated to obtain the band structure of a 2D photonic crystal. From Bloch's theorem and due to the symmetry of the triangular lattice, the band structure is shown for the irreducible Brillouin zone. Figure 2.5 shows the band diagrams of a triangular photonic crystal calculated by scanning the transverse component of the wave vector $\vec{k}_t\Lambda$ at 16 points along the boundaries of the irreducible Brillouin zone (see Figure 2.4) for $\beta\Lambda = 20$ left and $\beta\Lambda = 21$ right. In both cases a photonic band gap appears. As $\beta\Lambda$ is increased the bandgap is pushed towards higher frequencies whilst. The different bands, as in the one dimensional case, represent optical modes localized mainly in the silica and air regions, high and low refractive index. However, the mode field distribution is now in two-dimensions and its structure is more complicated than in the 1D case.

A useful way of seeing the behaviour of photonic bandgaps of PBGFs is by plotting the edges of the gaps as a function of β, this graph is known as *gapmap*. Figure 2.6 is the gapmap of a photonic crystal with triangular arrangement of circular holes in silica with an air filling factor $f = 45\%$, forming the cladding of a PCF. The radiation line indicates the lowest frequency of a mode allowed in the photonic crystal. Light incident on the cladding with a frequency below this line will be reflected. Above this line, light is free to propagate in the photonic crystal except in the bandgaps represented with green. Modes with frequencies in these ranges cannot exist in the photonic crystal cladding and only can be trapped and guided along a defect [1].

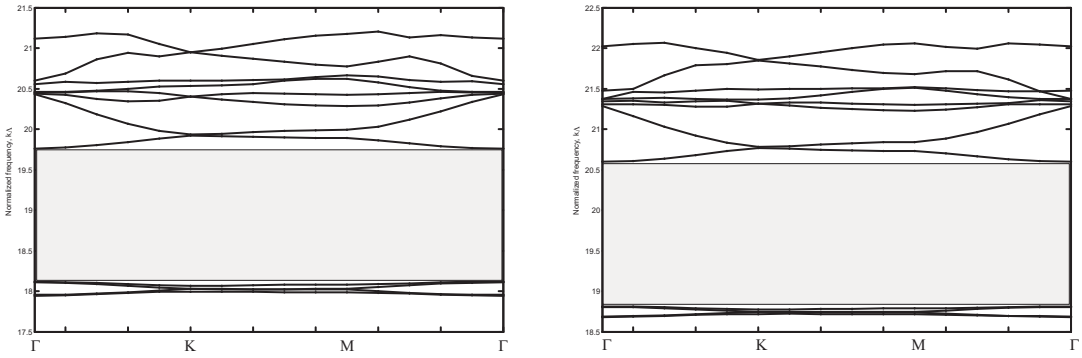

FIGURE 2.5: Band diagrams for a triangular PBGF for $\beta\Lambda = 20$ left and $\beta\Lambda = 21$ right. Shaded regions are bandgaps.

An important feature of this gapmap is that some of the bandgaps cross the air line, which is the region of the map with $\beta < k$. Indicating that electromagnetic waves with frequencies within these gaps are free to propagate in air. Therefore, light propagating in a region of air surrounded by the photonic crystal is not allowed to leave the air region but will be evanescent in the photonic crystal cladding due to interference effects. The presence of these bandgaps in the cladding structure opens the possibility of light guidance in an air core. It is important to notice that the PBGs overlap the air line only at some narrow regions. Therefore light can be guided in air only over narrow spectral intervals. A key point of the gap map (for air-silica) is that no gap extends for all values of $\beta\Lambda$ indicating that a complete 3D bandgap gap does not exist in a 2D photonic crystal. However a 2D bandgap is enough for bandgap guidance in the transverse direction [10].

In the case that the core is formed by a medium that has higher refractive index than the photonic crystal cladding, i.e. the blue region of Figure 2.6, light is free to propagate in the higher index core but will be evanescent in the lower index cladding. Therefore, the PCF operates in a similar way as a conventional fibre, for certain incidence angles light will be total internal reflected in the core-cladding interface.

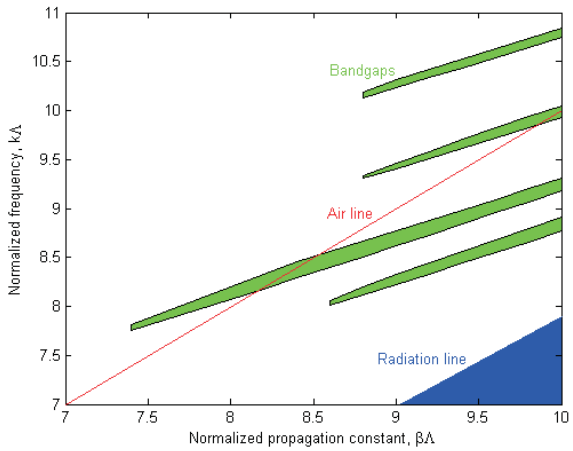

FIGURE 2.6: Band map for a triangular lattice of circular holes in silica with $f = 45\%$ The blue region is where holey fibres work, in this region light is transmitted by modified total internal reflection. Inside the bandgaps, green regions, light could be guided by the PBG effect. The regions of the bandgaps with $\beta < k$ may be used to guide light in an air core

2.2 Fabrication of PCFs

Optical fibre fabrication typically involves two stages, preform fabrication and fibre drawing. A preform is a large-scale replica of the fibre normally $\sim 50\,\text{cm}$ in length and $\sim 20\,\text{mm}$ in diameter (for PCFs). A preform is drawn down to micro-scale dimensions on a fibre drawing tower (see Figure 2.7). During the relatively short history of PCFs they are now made in many laboratories around the world using various preform synthesis methods, such as: stacking of capillaries and rods, sol-gel casting [34], ultrasonic drilling [35], extrusion from bulk glass with low softening temperature [36] and rolling flexible material sheets into tubes [37], each of which has advantages and disadvantages depending on the glass used and the desired fibre geometry.

For silica PCFs, capillary stacking has become the most widely used technique mainly due to the design flexibility it offers. In this approach, firstly, approximately half a metre long capillaries with a typical outer diameter of $\sim 1\,\text{mm}$ are drawn from a starting tube of high-purity synthetic silica with an outer diameter of $10 - 20\,\text{mm}$. The inner/outer diameter of the starting tube determines the ratio between the hole diameter and the lattice pitch (d/Λ) in the drawn fibre. The capillaries are stacked on a horizontal rig in a close-packed arrangement which reproduces the structure that is to be obtained in the final fibre. These package is then inserted into a jacket tube and packing silica rods of different diameters are carefully inserted to ensure mechanical stability of the structure. A rod placed in the centre of the stack acts as the solid core of index-guiding PCFs and a tube is inserted if a hollow-core PBGF is to be obtained. The resulting PCF preform is then drawn down to canes of few millimetres diameter. The top end of the

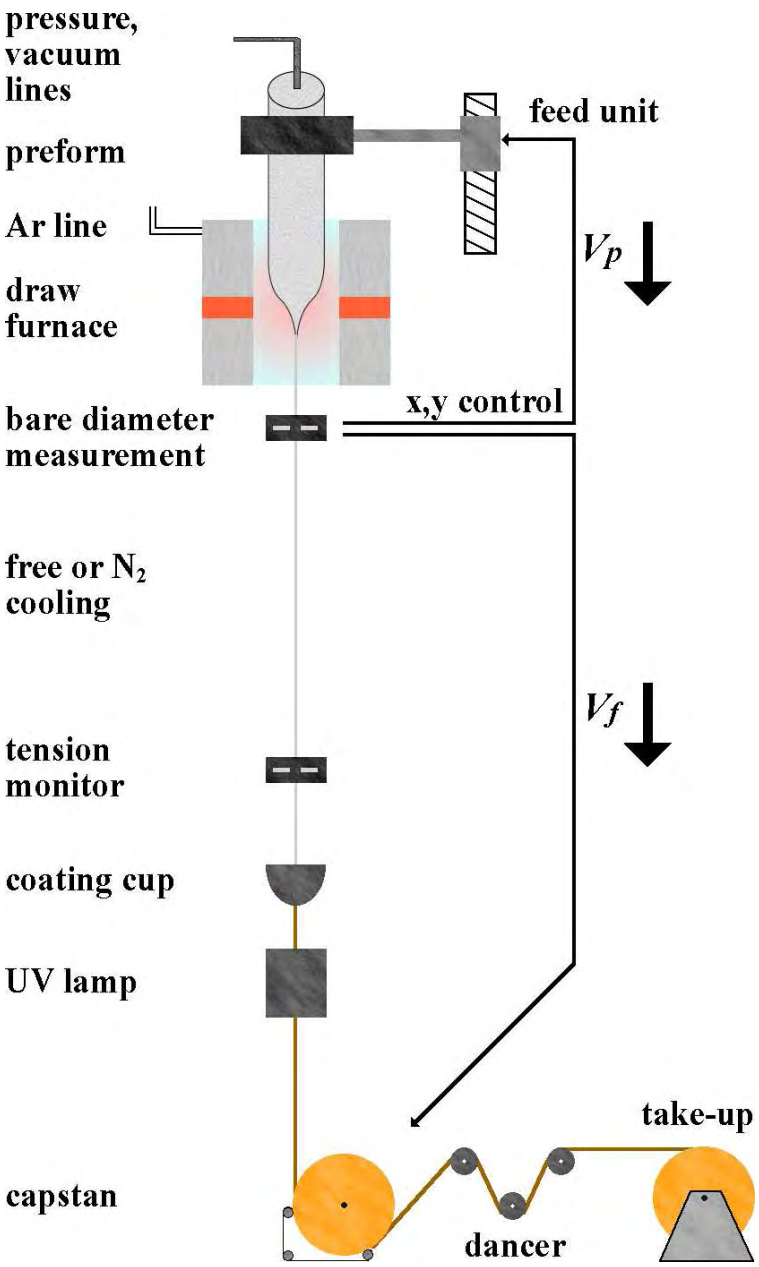

FIGURE 2.7: Schematic diagram for a drawing tower.

capillaries can be sealed in order to create pressure gradient to balance the collapsing effect of surface tension during drawing. Vacuum is normally used during this step to prevent the capillaries from moving. The resulting cane is inserted into a solid jacket tube and by applying a second drawing stage a PCF is produced. In this latest stage, the use of vacuum, pressure and the control of the drawing parameters (tension, furnace temperature, feed speed, fibre speed, etc.) are very important to obtain a fibre with optimal characteristics. Figure 2.8 shows a summary of the stack and draw fabrication process.

An amazing property of silica-air photonic crystal fibres is that the air channels in

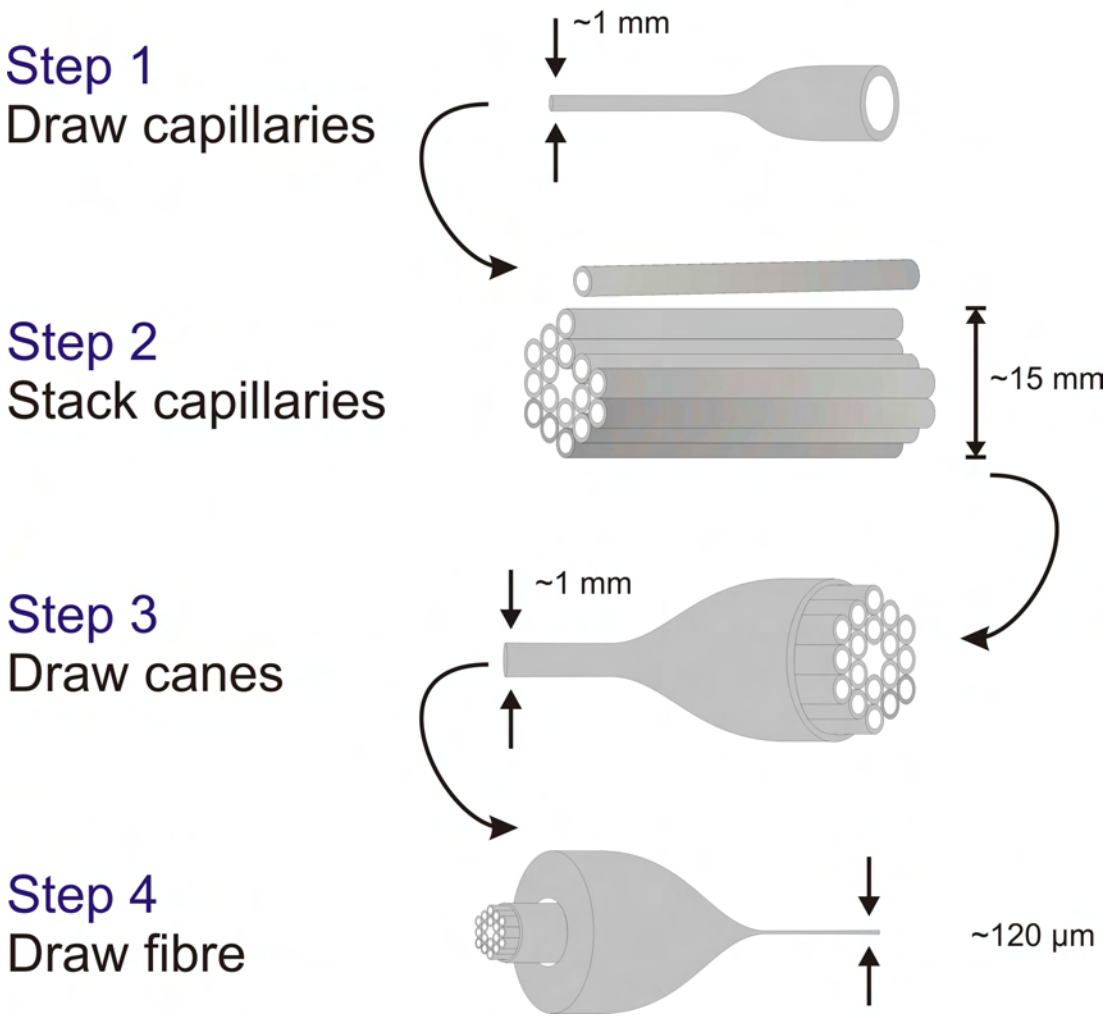

FIGURE 2.8: Summary of the stack and draw PCF fabrication process. Silica capillaries and rods drawn and stacked in order to create a fibre preform. The preform is drawn down to a cane of $\sim 1\,\text{mm}$ and finally this cane is introduced in a jacket tube and drawn down to a fibre.

centimetre scale preforms are preserved when drawn down to the micro-scale. After drawing, these micrometre wide channels run along fibres that can be hundreds of metres of even a couple of kilometres long. During drawing the preform is mounted in a holding chuck attached to a feed mechanism that lowers the preform into a furnace at the feeding speed (V_p). The furnace temperature is raised above the glass-softening temperature about $1900^\circ\,\text{C} - 2200^\circ\,\text{C}$. As the glass softens a "drop" forms due to gravity. The drawn fibre is taken up by the capstan which controls the draw speed (V_f). A variety of furnaces can be used to heat the preform. As turbulence around the fibre causes unacceptable variations in the fibre diameter, the furnace must provide laminar gas flow and must also give off no particles that might attach to the preform and degrade the fibre strength. The most common furnaces used that meet these requirements are graphite resistance and induction furnaces. The advantage of the induction furnace is its compact

size compared to resistance furnaces. The furnace includes inert gas inlets to provide laminar flow of a sufficient quantity to maximize fibre strength and minimize diameter variations characteristic of turbulent gas flows. Furnace temperature is measured with an optical pyrometer from either the outer surface of the heating element or directly from the preform neck-down depending on the furnace set-up, the former being the more typical configuration. The temperature can be controlled to within 1°C.

In order to maintain a uniform fibre diameter, the drawing process includes a diameter control loop. The fibre diameter is monitored as it exits the furnace. The output signal from the diameter monitor is used to automatically adjust the speed of the drawing capstan using a PID controller to obtain a constant diameter. Before the fibre reaches the capstan it is coated with a protective polymer. Coating is required to protect the pristine silica surface from scratches and abrasion and it preserves the intrinsic strength of silica. The coating usually consists of two layers of acrylate, a softer inner layer and a harder outer layer. However, it is possible to use the second coating only. Acrylate coating is applied in liquid phase and is solidified by UV-curing. Before coating the fibre must be cooled below 80° C. Thus, between the furnace and the coating cup the fibre is cooled down by the surrounding air. At high drawing speeds and with limited tower height it may be necessary to use forced cooling using inert gases as helium. After coating the fibre passes over a capstan onto a fibre take-up that winds the fibre onto a spool. Prior to coating, the fibre surface is exposed to potential ambient contamination that will reduce the fibre strength. The fibres are therefore drawn in a clean room.

2.3 Guidance mechanisms in photonic crystal fibres

The "simplest" optical fibre has a step-index geometry which consists of a central doped-silica cylinder with refractive index n_{co} surrounded by a silica cladding whose refractive index n_{cl} is slightly lower than that of the core, Figure 2.9(a). The refractive index profile of optical fibres is constant along the fibre axis, z. As the system is invariant under any translation along the z-axis, electromagnetic waves propagating along this axis have a dependence of $\exp(i\beta z)$ along the propagation direction. The propagation constant of the wave is β [equation (2.8)] which is the z-component of the wavevector. The propagation constant of light traveling in a medium with refractive index n is either equal to or smaller than the absolute value of the wavevector, i.e. $\beta \leq n\vec{k}_0$. Therefore, β must be less than or equal to $n_{co}k_0$ to propagate in the core and less or equal to $n_{cl}k_0$ to propagate in the cladding. The enclosed geometry of optical fibres defines resonant conditions on β which forces all the possible solutions of the Maxwell equations and the

values of β to be discrete. Each allowed field distribution (mode) in the fibre corresponds to an allowed β. Modes for which $n_{cl}k_0 < \beta \leq n_{co}k_0$ are called *guided modes* or *core modes*, as they are propagative in the core and evanescent in the cladding. On the other hand, modes with $\beta \leq k_0 n_{cl}$ are called *cladding modes*. These modes are not evanescent in the cladding. Guided modes usually have low loss whereas cladding modes usually experience high loss. It is convenient to define the effective mode index of a mode as $n_{mode} = \beta/k_0$.

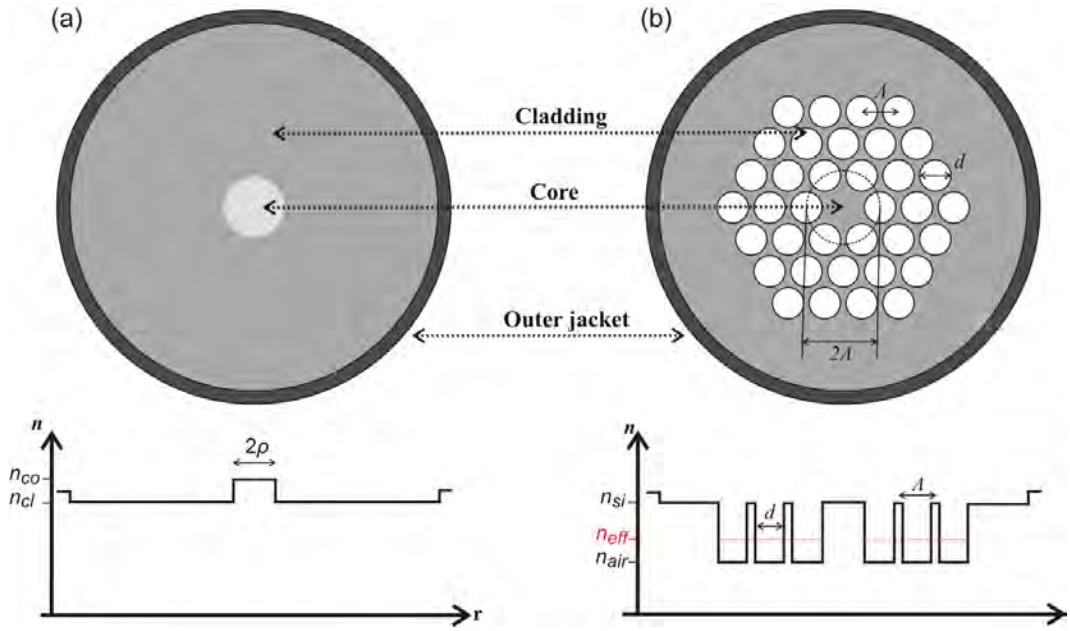

FIGURE 2.9: Cross sectional area and refractive index profile of (a) a conventional step-index optical fibre and (b) solid core PCF. In (b) the white and grey regions are air and silica respectively. The photonic crystal cladding is an ideal hexagonal lattice with parameters: pitch Λ and hole diameter d.

Since the size of the cladding is usually much bigger than the core size, the propagation constant of the cladding modes can be considered as continuous and to form a band. A core mode will inevitably couple into cladding modes if its propagation constant falls within a band of cladding modes. Therefore, in order to design optical fibres able to guide light, the propagation constant of the desired core modes must be outside the bands of cladding modes -this statement is not strictly valid for a certain type of PCFs, see chapter 7.

As it has been previously described, there are two possible methods of making such an optical fibre (see Figure 2.10). Firstly, index-guiding fibres, in which the core index is higher than the largest possible effective mode index of any cladding mode as illustrated in Figure 2.10(a). This is normally done either by doping the core glass so as to increase its refractive index compared to the lower-index glass which forms the cladding or by structuring the cladding so as to decrease its refractive index compared to the

core index, Figure 2.9. Both, conventional fibres and index-guiding PCFs fall into this category. Secondly, photonic bandgap fibres, in which a 2-dimensional photonic bandgap formed by a periodic cladding divides the continuum of cladding modes into different bands.

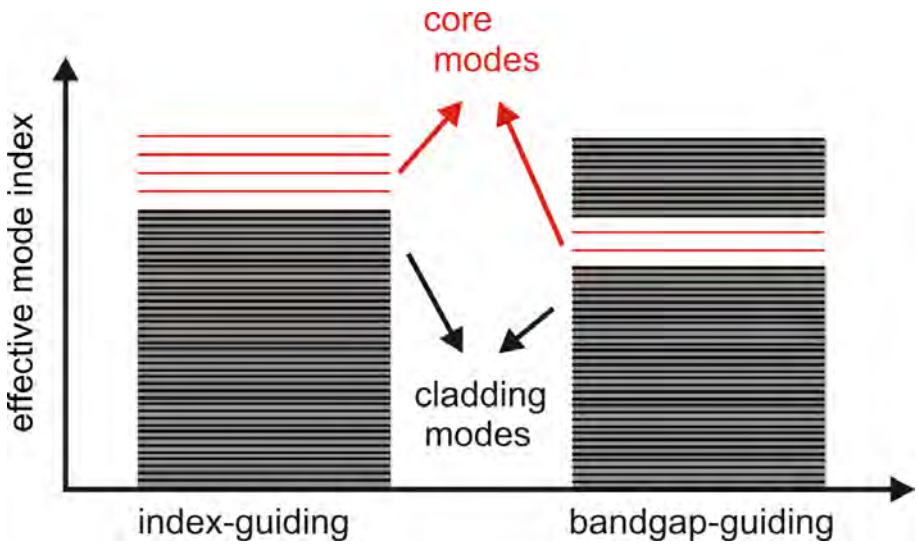

FIGURE 2.10: Schematic illustration of the two possible guidance mechanisms of optical fibres. Cladding modes are represented with black lines and red lines are the discrete guided modes. In index guiding fibres the core refractive index is greater than the cladding refractive index (left). In bandgap fibres the continuous of allowed cladding modes is split in two bands. The core modes are located between these two cladding bands (right).

The following sections briefly describe some properties and applications of index-guiding PCFs while the next chapter describes hollow-core photonic bandgap fibres which are the main focus of this thesis.

2.3.1 Index-guiding PCFs

In conventional optical fibres, light propagation is due to total internal reflection at the core-cladding interface. In these fibres, the maximum cladding mode index is limited by the cladding refractive index, which must be lower than the core refractive index. Under this condition, there can exist a core mode whose mode index is bigger than the material index of the cladding -see Figure 2.10(a).

Index guiding PCFs guide light by means of a *modified total internal reflection* mechanism, in which light propagates in a solid core, surrounded by a structured cladding (not necessarily periodic). In these fibres, the maximum cladding effective mode index is reduced not by using different materials but by having micro-holes in the cladding. The low cladding mode index is somewhere between the bulk material index and that

of air. This ensures the core modes to have greater mode refractive index than the cladding modes. Thus, light incident at certain angles propagates in the high refractive index core by a form of total internal reflection as in conventional optical fibres [12]. Figure 2.9 depicts a comparison of a typical refractive index profile of a conventional step-index fibre and an index-guiding PCF.

Some of the basic optical properties of index guiding PCFs can be related to fundamental concepts concerning conventional optical fibres. For this, Birks *et al.*[13] proposed the now well known effective index method. This method consists of interpreting the structured cladding as a solid medium with a properly chosen effective refractive index, n_{eff}. The effective index method uses a scalar model to evaluate the periodic structure of the cladding in order to calculate n_{eff}. The first step of the effective index method is to determine the fundamental mode or fundamental space-filling mode of the photonic crystal cladding (the cladding mode with the highest refractive mode index). This is done by solving the wave equation (Eq. 2.5) within a cell centred at one of the holes in the periodical lattice. The propagation constant of the resulting fundamental space-filling mode (β_{FSM}) is the maximum propagation constant allowed in the cladding, and can be used to define the effective index $n_{eff} = \beta_{FSM}/k_0$. The red line in Figure 2.9b indicates the effective refractive index of the cladding. The resulting waveguide consists of a solid core and a solid cladding with refractive indices n_{co} and n_{eff} respectively. As a result, some modelling elements for standard optical fibres can be applied for PCFs. Similarly to conventional fibres, the propagation constant of any mode supported in the core needs to be $k_{co} > \beta > \beta_{FSM}$. The effective index method which is valid for small holes provides a good qualitative description of the optical properties of index-guiding PCF [38].

2.3.2 Properties of Index-guiding PCFs

The number of guided modes supported by a step-index fibres depends on the normalized frequency:

$$V = k_0 \rho \sqrt{n_{co}^2 - n_{cl}^2}\,, \tag{2.17}$$

where ρ is the core radius, n_{co} and n_{cl} are the refractive index of the core and cladding respectively [39, 8]. The smaller this parameter the fewer guided modes supported by the core. If at a given wavelength $V < 2.405$, the fibre can only guide one pair of orthogonally polarized modes which have the same β, and the fibre is said to be single-moded. Either of these two degenerated modes is know as the fundamental mode. The design of single mode fibres requires a combination of small core size to wavelength ratio, typically core

sizes between 8.3 to 10 μm for 1550 nm operation, and a small difference in refractive index between the core and cladding. Equation (2.17) indicates that step-index fibres are always multi mode for sufficiently small wavelengths.

The normalized frequency of PCFs is defined as an effective value

$$V_{eff}(\lambda) = k_0 2\Lambda \sqrt{n_{silica}^2 - n_{eff}^2(\lambda)}\,, \tag{2.18}$$

where 2Λ is the core diameter. Endlessly single mode behaviour in PCFs at any wavelength from the UV to the near infrared was observed by Birks *et al.* [13]. Fibres with $d/\Lambda \leq 0.4$ do not support higher order modes as their normalized frequency remains smaller than 2.405 for any wavelength [18]. Endlessly single-mode guidance in PCF originates from the strong wavelength dependence of the cladding refractive index. Light of long wavelengths penetrates into the cladding region and thus, part of its energy is concentrated in the air regions, whereas, shorter wavelengths concentrate most of the energy in the silica core, forcing the core/cladding index difference to fall as the wavelength gets shorter. This counteracts the usual trend towards multimode behaviour and $V_{eff}(\lambda)$ is almost kept constant. As single mode operation does not depend upon the core size but only on the air filling fraction [18], single mode fibres with large cores can be developed, for example a single-mode PCF at 458 nm with core diameter of 22 μm was fabricated [40]. A conventional fibres would require a core $\sim$ 10 fold smaller to be single-moded at this wavelength. Large mode area single mode PCFs are able to transmit higher power before nonlinear effects affect the beam quality. Such fibres are desirable in laser and amplifiers [41, 42].

The optical properties of index-guiding PCF are extremely sensitive to the cladding and core structure. By chosing the pitch, hole and core size, these fibres can present many interesting dispersion, modal and nonlinear properties which are impossible to obtain with standard step-index fibres. For example, PCFs can exhibit unique dispersion properties [21, 23], like flat dispersion covering a broad window [22, 43] and the zero dispersion wavelength can be engineered to be below 1.28 μm which is the ZDW (zero dispersion wavelength) of conventional single-mode fibres [19]. High nonlinearity is another interesting property of index guiding PCFs. Fibres with high air filling fraction can tightly confine light in a small core and thus have high nonlinearity - due to small mode area. Nonlinearities 10-50 times greater than that of conventional fibres can easily be achived with PCF technology. Many nonlinear optical processes such as wavelength conversion, Raman amplification [44], optical switching [45, 46], parametric processes [47], soliton squeezing [48, 49], and supercontinuum generation [17, 50, 51, 52, 53] have been observed in these fibres.

The main subject of this thesis is hollow-core PBGFs therefore readers interested in index-guiding PCF and their applications are referred to a number of comprehensive reviews [11, 1, 2, 54]. The following chapter describes the development, applications and modal properties of hollow-core photonic bandgap fibres.

Chapter 3

Hollow core photonic crystal fibres

As mentioned in previous chapters, the guiding properties of hollow-core photonic bandgap fibres rely on the existence of 2-dimensional photonic bandgaps formed in a precisely structured cladding [14]. Light propagation within the synthetic cladding is prohibited for well defined ranges of optical frequencies and propagation constants. A defect in the photonic bandgap cladding forms the core of the fibre and light introduced into the core mode is then unable to escape through the surrounding cladding material. It is therefore well confined to the core and can be guided with low attenuation. Outside the bandgap the light spreads out into the cladding and is lost. As PBGFs do not rely on total internal refection for guiding, these fibres do not need a high refractive index core to achieve light guidance, allowing the propagation to take place within a core that can even be hollow.

In silica-air hollow-core photonic bandgap fibres light guidance is achieved by surrounding the core with several hundreds of smaller holes arranged in a triangular lattice, a SEM of a HC-PBGF is shown in Figure 3.1(a). Two other types of waveguides have been used to guide light in a hollow core: Kagome fibres Figure 3.1(b), and Bragg fibres Figure 3.1(c). In 1978, Yariv and Yeh [55] theoretically proposed a fibre with a 1D-periodically structured cross-section which could guide light in a low refractive index core due to a Bragg mirror that reflects light back into the core. This type of fibre requires a large refractive index contrast between layers for low confinement loss which makes it difficult to find two compatible materials. A solid core version of a Bragg fibre can be made using modified-CVD [56]. In addition, employing a combination of polymer and chalcogenide glass, a group at MIT in the US have realized hollow-core Bragg fibres for 10 μm and near infrared wavelengths [57, 58, 59]. Recently, an all-silica

Bragg fibre was demonstrated by Vienne *et.at.* [60], Figure 3.1(b). Kagome fibres also have a 2-dimensional photonic crystal cladding. However, the Kagome cladding does not present bandgaps; instead, light is guided thanks to an inhibited coupling between the core mode and cladding modes [61, 62]. These fibres present very interesting properties such a ultra-broad transmission windows as well as low dispersion and dispersion slope. This chapter focused on studying the modal properties of HC-PBGF, the guiadance mechanism of Kagome fibres is studied in chapter 7.

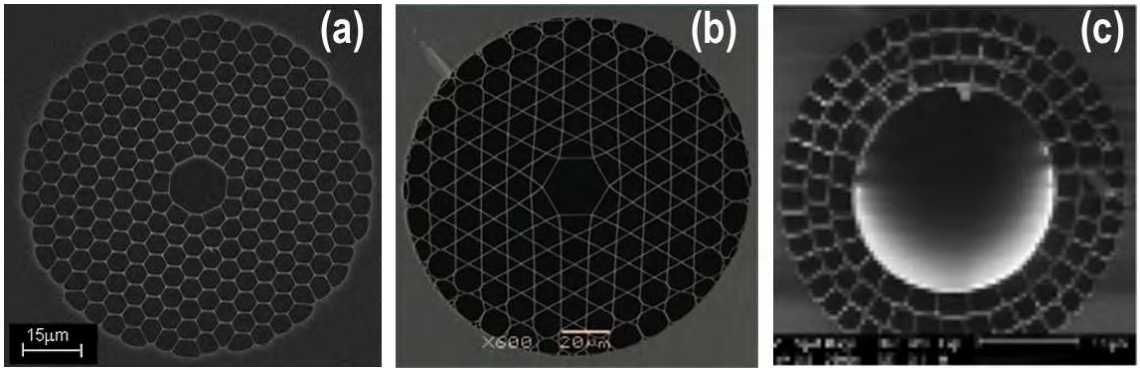

FIGURE 3.1: Examples of silica-air hollow-core photonic crystal fibres. (a) Hollow-core photonic bandgap fibre fabricated at the ORC, core diameter ∼13 μm. (b) Large pitch Kagome fibre, core diameter ∼23 μm from [63]. (c) Bragg fibre, core diameter 20 μm from [60].

3.1 Low-loss HC-PBGFs: applications and general overview

Guiding light with low-loss in a hollow-core holds many promising applications such as delivery and manipulation of high energy ultra-short pulses [64, 65, 66, 67], high power delivery without the risk of destroying the fibre [68], gas sensing [69], particle guidance [70] or guidance in air with lower loss than a standard single mode fibre. Furthermore, this class of fibre has exotic properties not found in any other optical fibre. They can have approximately 1000 times lower nonlinearity than conventional optical fibres and due to the strong confinement, extreme nonlinear interactions between light and matter can be achieved by filling the core with appropriate gases [70, 71, 72, 73, 74]. Additionally, HC-PBGFs are insensitive to bending and present unique dispersion properties.

In conventional optical fibres the group-velocity dispersion of the guided mode is dominated by the dispersion of the bulk material from which the core is made. Instead, due to a negligible contribution from the core material (air), the total dispersion of HC-PBG

fibres is completely dominated by waveguide dispersion. Since HC-PBGFs can only confine light of wavelengths within the bandgap, their transmission spectrum can be thought as the one of a transparent material with a transmission window expanding the bandgap width, this is schematically shown in Figure 3.2(a). This shape of the transmission spectrum gives HC-PBGFs unique dispersion curves, Figure 3.2(b); it starts with large normal dispersion at the blue edge of the photonic bandgap, passes through zero, and becomes anomalous towards the long wavelength bandgap edge -anomalous dispersion values in the thousands of ps/nm/km regime are easily obtained. The zero-GVD dispersion wavelength is always shifted towards the short wavelength bandgap edge rather than being at the centre of the transmission window. This is due to the anomalous contribution to the waveguide dispersion caused by the variation of the core size/wavelength ratio which shifts the curve in Figure 3.2(b) upwards.

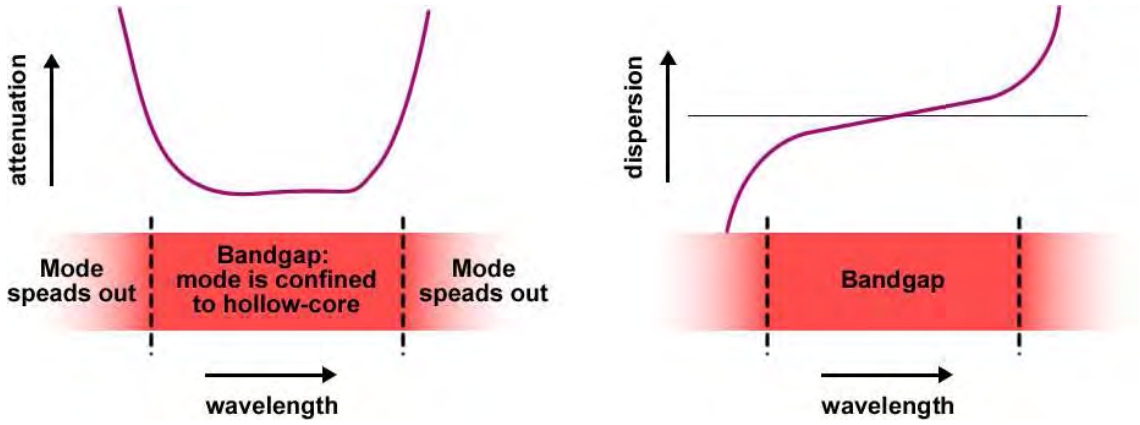

FIGURE 3.2: Schematic of the (a) low-loss transmission window and (b) GVD-dispersion of a HC-PBGF.

Hollow-core PBGFs have various loss mechanisms which are different to conventional fibres. First, if the bandgap is not wide enough then coupling from the core mode to cladding modes due to fibre non-uniformities can easily occur. A narrow bandgap also implies that in order to avoid direct leakage of light from the core and therefore reduce the confinement loss, many rings of holes are required. The first HC-PBGF [14] had a high loss and a very narrow bandgap due to the low air-filling fraction of its cladding. Then lots of efforts were focused on improving the fabrication procedure to increase the fibre homogenity and increase the air filling fraction of the cladding. With these improvements just 3 years after the first demonstration of a HC-PBGF, a group in Corning demonstrated a fibre with a loss of 13 dB/km [75]. This fibre had a very high air-filling fraction and the transmission window extended over approximately 20% of the central bandgap wavelength, Figure 3.3(a). At that time it was noticed that the transmission performance of the fibre was neither limited by confinement loss (since it incorporated enough cladding holes to suppress confinement loss) nor by the width of the photonic bandgap, instead by a mode coupling mechanism between core modes and

surface modes guided at the core cladding interface [76, 77]. It was shown that the coupling with surface modes is responsible for the attenuation peaks around 1600 nm in the attenuation spectrum of the fibre, Figure 3.3(a). Surface modes clearly limit the transmission bandwidth of the fibre and air guidance with low attenuation is not possible over the full bandgap of the photonic crystal cladding which for this fibre extends from around 1400 nm to 1780 nm.

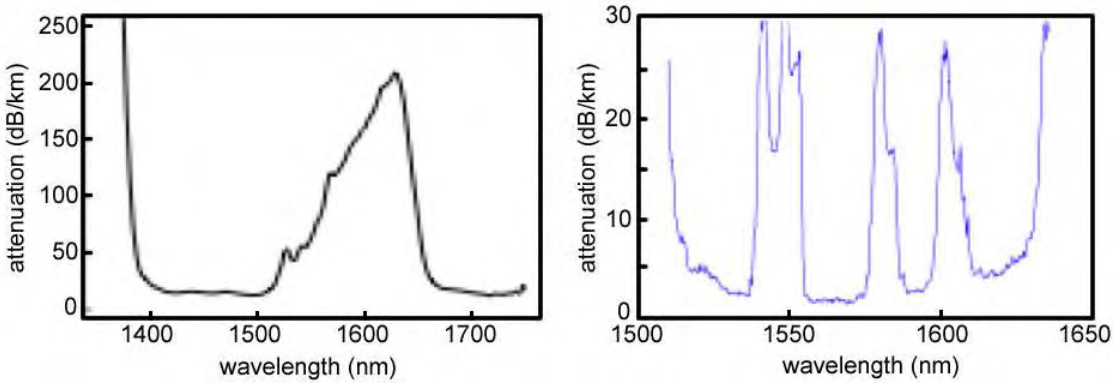

(a) (b)

FIGURE 3.3: Attenuation spectrum of low-loss HC-PBGF: (a) 7-cell core fibre with a minimum attenuation of 13 dB/km fabricated by Corning [75] and (b) lowest loss (1.2 dB/km) HC-PBGF with a larger 19-cell core and antiresonant core surround fabricated by Blaze Photonics [78].

Just one year later, by making a fibre with a larger core and by adjusting the core boundary an impressive reduction of the attenuation to 1.2 dB/km was achieved [79, 15]. On the other hand, this fibre presented several surface modes and low-loss was only achieved over narrow spectral windows. Roberts *et.al* [79] realized that surface imperfections at the glass boundaries are already limiting the loss of HC-PBGFs. The surface roughness scatters and couples light from the core guided mode to cladding modes that are not guided and to surface modes. These surface imperfections are due to surface capillary waves frozen during the fibre drawing process and have thermodynamic origins which make it impossible to be completely eliminated. Surface capillary waves exist on liquid surfaces (such as molten glass) and as the glass solidifies they freeze leaving fluctuations at the surface. The statistical spectral density $S_z(\kappa)d\kappa$ is the mean square amplitude of roughness components with spatial frequencies along the fibre between κ and $\kappa+d\kappa$. For a cylindrical hole of perimeter W [79]

$$S_z(\kappa) = \frac{k_B T_g}{4\pi\gamma\kappa} \coth\left(\frac{\kappa W}{2}\right), \tag{3.1}$$

where T_g is the glass transition temperature, k_B is the Boltzmann's constant, and γ is the surface tension. Surface roughness with a spatial frequency κ couples light from the

fundamental mode of effective mode index n_0 to modes of modal index n given by

$$\kappa = \frac{2\pi}{\lambda}|n - n_0|, \tag{3.2}$$

$S_z(\kappa)$ and the transverse overlap of the modes at the glass surfaces determines the strength of the coupling and the loss can be calculated from the power coupled to the modes. Since HC-PBGF support many cladding modes, surface modes and other core modes, an exact calculation is extremely complicate. However, to a good approximation the overlap of the fundamental air-guided mode with the glass air/interfaces represents a relative measure of the scattering loss due to surface roughness. The normalized interface field intensity can be given by [79, 80, 81]

$$F = \left(\frac{\epsilon_0}{\mu_0}\right)^{1/2} \frac{\oint_{holeperimeters} dl|\mathbf{E}|^2}{\int_{cross-section} dA|\mathbf{E} \times \mathbf{H}^*| \cdot \hat{\mathbf{z}}}, \tag{3.3}$$

where $\mathbf{E}$ and $\mathbf{H}$ are the electric and magnetic fields of the fundamental mode and $\hat{\mathbf{z}}$ is the unit vector along the fibre. Reducing the fibre loss becomes an exercise of reducing the *F-factor*. Improved fibres designs that minimize the overlap of the guided mode with the glass boundaries reduce the scattering loss. From the transmission spectra in Figure 3.3 is also clear that the performance of HC-PBGFs can be improved by eliminating surface modes.

3.2 Modal properties of HC-PBGFs

In general, when designing HC-PBGFs with a wide low-loss transmission window one needs to consider the structure of the cladding and the core. Firstly, the photonic bandgap is determined uniquely by the cladding. Therefore the maximum range of wavelengths over which light can be guided is fixed by the cladding structure. Typically, higher air-filling fractions produce a wider bandgap [82, 83]. Claddings with high air-filling fractions are thus required for broadband transmission and low confinement loss [77]. Secondly, the core defect has to be chosen properly. Ideally, the hollow core would be formed in such a way as to introduce a single core-localized photonic state within the cladding bandgap. However, the termination of the periodic cladding to form the core can lead to the introduction of unwanted guided modes into the bandgap. As described in this section, surface modes exist in the same spectral range as the core-guided air mode, but have far higher dispersion due to their large overlap with the glass. They couple with the air mode in some wavelength ranges leading to hybrid modes,

greatly increasing the attenuation and dispersion of the air mode and reducing the useable bandwidth of the fibre. In practice, the core guided mode should have a gaussian or near gaussian profile to facilitate an efficient coupling to conventional fibres. Therefore, the cores of hollow-core photonic bandgap fibres have normally been formed by omitting the central 7 or 19 cells from the stack, creating an almost circular void [84].

In this section the modal properties of HC-PBGFs are analyzed. Firstly, the evolution of the bandgap structure of a triangular lattice without any core as a function of the air filling fraction is studied. Then a defect is introduced to the periodic lattice to form the core of the fibre and the properties of the different modes supported within the bandgap are discussed.

3.2.1 Photonic bandgap cladding

As previously mentioned (section 2.2), hollow-core fibres are usually made by the stack-and-draw process. Therefore, the geometry of the air-holes is limited by the shape of the elements that can be stacked in a packed array. Although surface tension and pressure applied while drawing the fibre can, to certain extend, modify the structure, the design space is still very limited. Hence, many if not most of the limitations on the design of suitable hollow-core PBGF claddings come directly from the fabrication process. Several photonic crystals have been analyzed and proposed as possible air-guiding structures. These structures must have at least one bandgap crossing the air line [10, 1, 11] (Figure 2.6). Much effort has been devoted to find structures providing the widest bandgaps, however the standard cladding design of hollow-core photonic bandgap fibres consists of a triangular lattice of close-packed circular holes [10]. Other lattices such as honeycomb [85, 86], modified honeycomb [87, 88], and square [89, 90] have been numerically studied. Although, it was shown that they present out-of plane photonic bandgaps crossing the air line, the triangular lattice is the best alternative so far as it provides the widest bandgaps and it is relatively easy to fabricate. Therefore, only HC-PBGFs claddings with a triangular lattice are considered here.

It is also important to consider that the pitch of the cladding should ideally be several times the central wavelength of the bandgap, this is simply because it is far easier to fabricate large structures rather than small ones[1]. A large pitch is also better compared to a small pitch because real fibres have a finite cladding and therefore present confinement loss. As the pitch gets larger the separation between the core and the outside of the fibre gets larger as well, which in turn reduces the confinement loss.

[1]When the fibre is drawn, the glass softens and surface tension collapses the holes. However, small holes collapse quicker than large holes, which makes the fabrication of small structures a lot more complicated.

3.2.1.1 Triangular lattice: band structure *vs.* air filling fraction and hole shape

A useful way of summarizing the dispersion relation or band structure $\omega_n(k)$ of the photonic crystal cladding is by calculating the photonic density of states (DOS). The DOS is defined by counting all allowed modes (electromagnetic states) with a given frequency ω:

$$DOS(\omega) = \sum_n \int_{BZ} d^2k\delta(\omega - \omega_n(\vec{k})) \tag{3.4}$$

where n represents the band number, $\delta(w)$ is the Dirac delta function, and the integral is calculated over the irreducible Brillioun zone. The photonic bandgaps manifest as regions of zero density of states.

Figure 3.4 shows the evolution of the band structure as a function of the air filling fraction of a HC-PBGF cladding with a triangular lattice of circular holes with diameter d and pitch Λ. The background material is silica with refractive index $n = 1.44$. The DOS of claddings with different values of d/Λ (i.e. air filling fracion[2]), are plotted as a function of normalized wavelength (λ/Λ) and effective mode index (β/k) in Figure 3.4($left$). The modes supported by the structures are computed using a freely available plane-wave expansion software package [91]. And the integral of equation (3.4) is evaluated by considering the Dirac delta function as a triangular function [82]. The calculated DOS values are normalized to the density of states in air. Gray scale is used to represent regions of high and low density of states. The red areas correspond to zero DOS of states (bandgaps).

For $d/\Lambda = 90\%$ and $\lambda/\Lambda < 0.66$, several bandgaps crossing the airline appear but they are very narrow and do not extend far away from the air line $\beta/k = 1$. The widest bandgap is centred at a longer wavelength $\lambda/\Lambda = 0.65$ and is the only one that remains open and crossing the air line as d/Λ increases. As the air filling fraction increases this bandgap is blue shifted and becomes exponentially wider. This behaviour is very clear in Figure 3.4($right$) which plots the bandgap width ($\Delta\lambda$) normalized to the central bandgap wavelength λ_c as a function of d/λ. $\Delta\lambda$ and λ_c are obtained from the points at which the edges of the bandgap cross the air line. The maximum achievable bandgap width for an un-supported structure with d/Λ =1 is ∼41% of the central wavelength. In this case the pitch is 2.5 times the wavelength of operation λ_c.

Since wider bandgaps are obtained by increasing the air-filling fraction, much effort has been concentrated on developing fabrication techniques allowing structures with

[2]The air filling fraction of a triangular lattice of circular holes is $\frac{\pi(d/\Lambda)^2}{2\sqrt{3}}$. The air filling fraction of an un-supported structure $d/\Lambda = 1$ is ∼91%

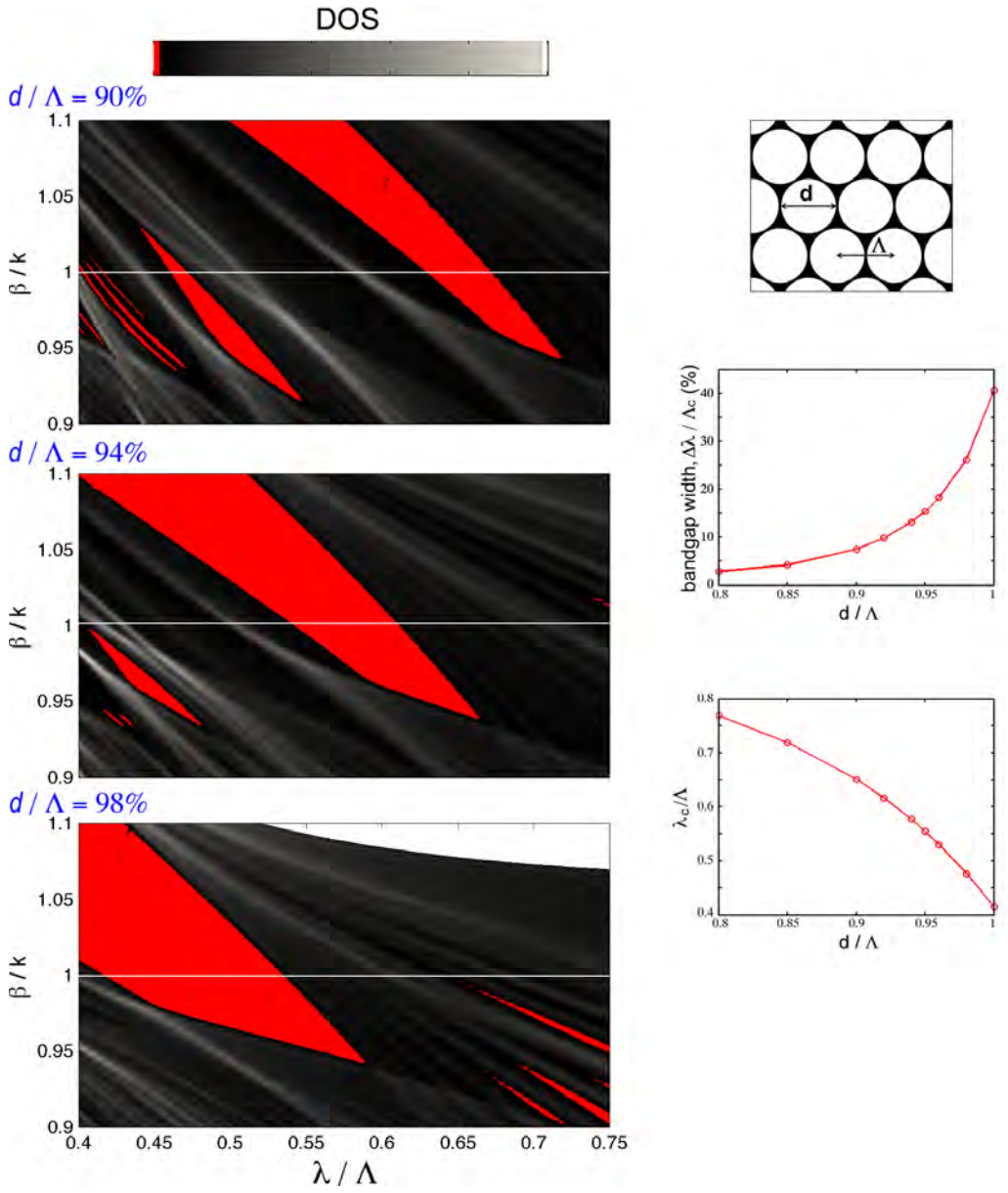

FIGURE 3.4: Evolution of the band structure of a HC-PBGF cladding as a function of the air filling fraction. (*left*) DOS plots for different values of d/Λ. (*right*) From top to bottom: triangular lattice of circular holes in silica, bandwidth as a function of d/Λ, and central wavelength of the bandgap as a function of d/Λ.

high air filling fraction. However, this has resulted in distortion of the cladding holes and fibres with large air filling fraction (larger than 85%) ended up having hexagonal holes with rounded corners instead of circular shape [75, 15]. In order to describe accurately the bandgap properties of high air filling fraction fibres, Mortensen *et al.* [83] introduced a more realistic cladding structure with rounded hexagonal holes into their model. Figure 3.5(a,b) show the parameters used to represent the cladding: hole size d, curvature at the corners d_c and pitch Λ. Figure 3.5(c) is a SEM micrograph of the

cladding holes of a high air filling fraction fibre. Clearly, the voids have formed an almost perfect close packed crystal structure of hexagons with rounded corners.

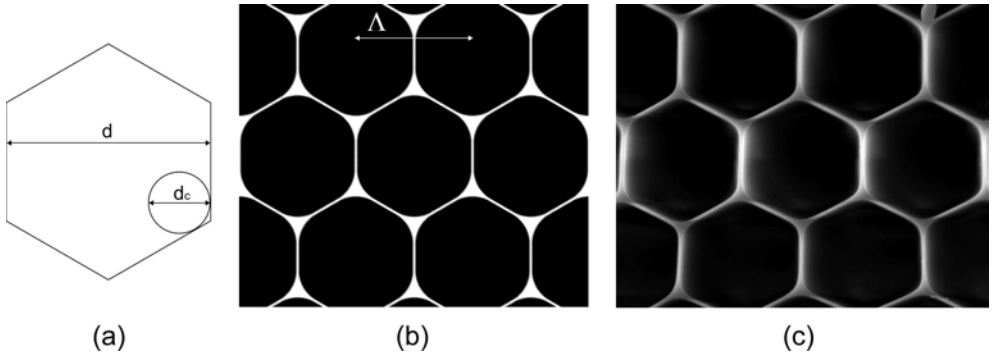

FIGURE 3.5: (a) Hexagon with rounded corners used to represent the air holes of realistic HC-PBGF cladding structures as proposed in [83]. (b) Triangular lattice of rounded hexagonal holes with $d/\Lambda = 0.98$, and $d_c/d = 0.6$. (c) SEM micrograph, cladding holes of the high air filling fraction fibre in [16].

The air filling fraction of the cladding is related to the hole parameters by [83]:

$$f = \left(\frac{d}{\Lambda}\right)^2 \left[1 - \left(1 - \frac{\pi}{2\sqrt{3}}\right)\left(\frac{d_c}{d}\right)^2\right] \tag{3.5}$$

By analysing image Figure 3.5(b,c) further, it is possible to see that between three adjacent voids there is a glass node which is supported and joined to adjacent nodes by thin silica struts. The cladding profiles in Figure 3.6 show that for a given value of d/Λ an increase in the air filling fraction is obtained by decreasing d_c/d which makes the holes more hexagonal and reduces the size of the nodes. For prefect hexagonal holes, obtained when $d_c/d = 0$, the silica nodes vanish. Instead circular holes, obtained for $d_c/d = 1$, present the largest nodes.

Figure 3.6 also compares the evolution of the air-guiding bandgap of cladding structures with constant $d/\Lambda = 0.98$ as a function of the hole shape (i.e. d_c/d). Hexagonal holes, which do not present silica nodes, form a very narrow bandgap that does not extend far below the airline. This clearly indicates that the glass nodes are required for the bandgap formation. As the holes become more circular (d_c/d increases), the nodes become larger and the bandgap widens. The bandgap position is strongly dependent on the size of the silica node. The graphs in Figure 3.6(*right*) plot the calculated bandgap width and central bandgap wavelength for different values of d_c/d. These results show that for a given d/Λ value, the maximum bandgap width is not achieved with circular holes but instead with a more hexagonal hole which has slightly larger air filling fraction. For $d/\Lambda = 0.98$ the widest bandgap is obtained when $d_c/d \approx 0.7$.

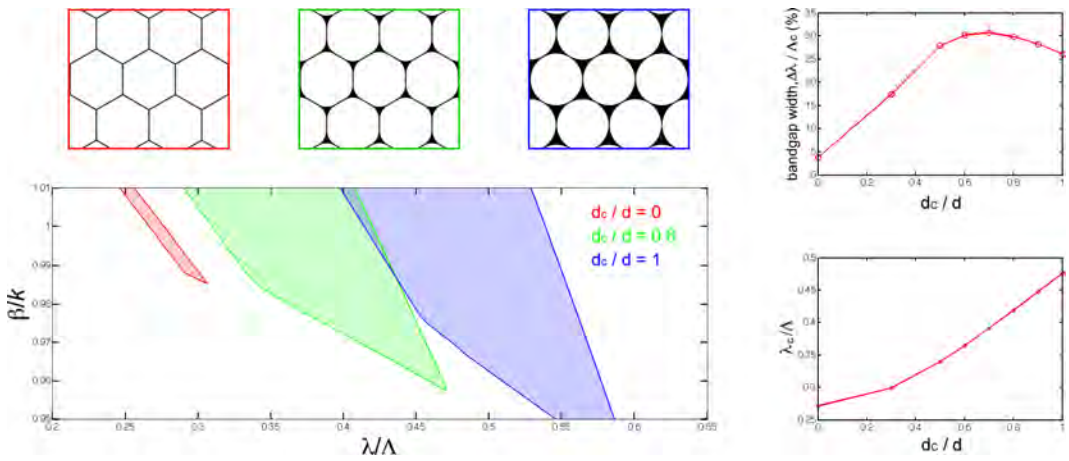

FIGURE 3.6: Evolution of the air-guiding bandgap of cladding structures with $d/\Lambda = 0.98$ as function of the hole shape.

3.2.2 Air-guided core modes and surface modes

In the ideal case, when forming the core of a hollow-core fibre, only one photonic state tightly confined in the air core would be introduced within the cladding bandgap. However, the termination of a periodic structure at the core cladding interface may also introduce surface guided modes. To study this, let's form a fibre by removing the 7 central cladding unit cells of a photonic crystal. The cross section of the resulting fibre is shown in Figure 3.7(a). The calculated dispersion curves of the modes supported by the fibre are plotted against normalized wavelength in Figure 3.7(b). In this figure, the extended cladding modes are represented with black dots and an example of such a mode shown in Figure 3.7(c). The photonic bandgap spans from $\lambda/\Lambda = 0.52$ to 0.64, where no cladding modes exist. Importantly, within the bandgap it is possible to distinguish two very distinct dispersion curves. The first one (blue) is flat and lies below the airline while the second (red) is much more steeper and crosses the airline. The former dispersion curve corresponds to the fundamental core mode[3] which is concentrated in the air-core Figure 3.7(d), while the later is an "unwanted" surface mode which is concentrated at the surface separating the core from the cladding Figure 3.7(e). Finally, the green lines close to the short wavelength bandgap edge correspond to higher order core modes.

Due to their large overlap with the glass, surface modes have higher dispersion than air-guided modes and thus their dispersion curves cross at specific wavelengths, gray region in Figure 3.7(b). This interaction between modes leads to hybrid modes and anticrossing of their dispersion curves. Near the anticrossing, the fibre's performance is severely limited because the attenuation of the core mode becomes very high (see Figure 3.3).

[3]It fact, it is a degenerate pair which we call fundamental core mode. However, it is not the fundamental mode of the fibre (mode with the largest effective index), but we call it fundamental air-guided mode or fundamental mode because is the core confined mode with largest n_{eff}.

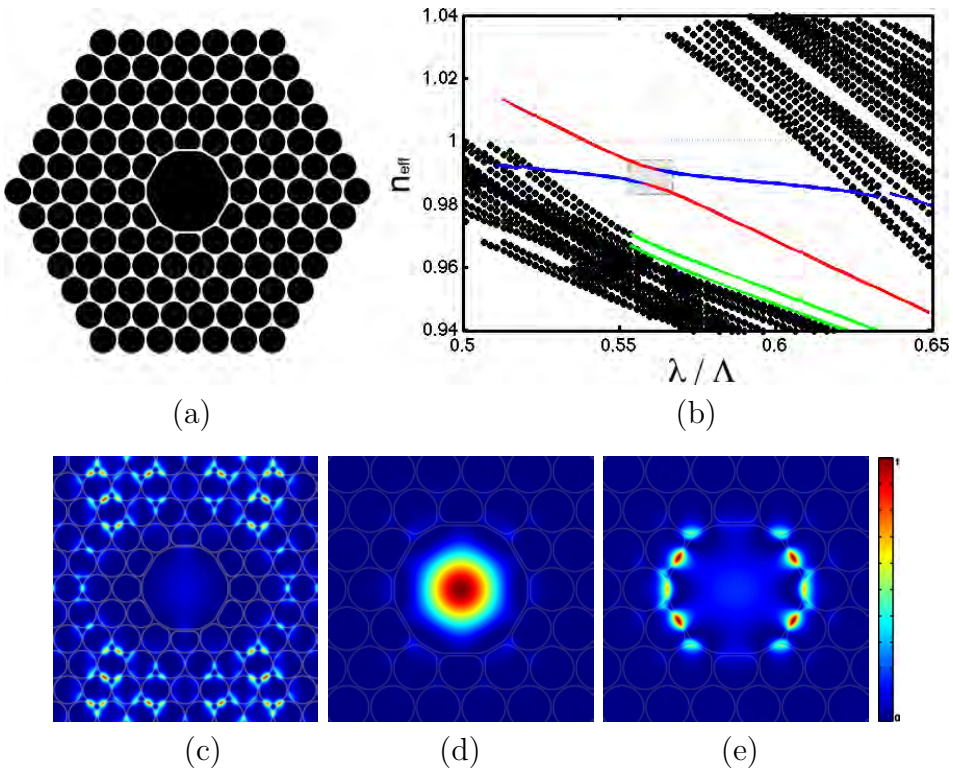

FIGURE 3.7: (a) Cross-section of the modelled 7-cell hollow-core fibre. (b) Calculated dispersion of modes of the fibre. Examples of intensity profiles of a cladding mode, fundamental air-guided mode and surface modes in (c,d,e) respectively.

To understand the effect of the coupling between surface and core modes, Figure 3.8 shows the dispersion curves of the fundamental air-guided mode and the surface mode in the vicinity of the anticrossing together with the evolution of their intensity profiles. At point *i* and *iv* it is easy to distinguish the core mode from the surface mode as the former has little energy in the glass boundary. But when the modes get closer in n_{eff} (i.e. points *ii* and *iii*) the modes have a large amount of energy in the glass and it is not possible to distinguish them as either a core-like mode or a surface-like mode. Since surface modes have a high overlap with the cladding region perturbations along the fibre, such as surface roughness, will easy couple light from them into the closely-spaced cladding modes [76]. Therefore, any light that gets coupled from the core to a surface mode will then couple to cladding modes and will be lost.

Also note that coupling light from a gaussian beam into the fibre is more efficient for wavelengths away from the anticrossing region since the overlap of a gaussian beam and the core-like mode is larger than its overlap with the hybrid mode at the anticrossing wavelengths. For this reason, the transmission spectrum of a fibre that supports surface modes presents attenuation peaks even when short pieces of fibre are used which could be a problem for certain applications such as gas sensing where a flat transmission spectrum is desirable.

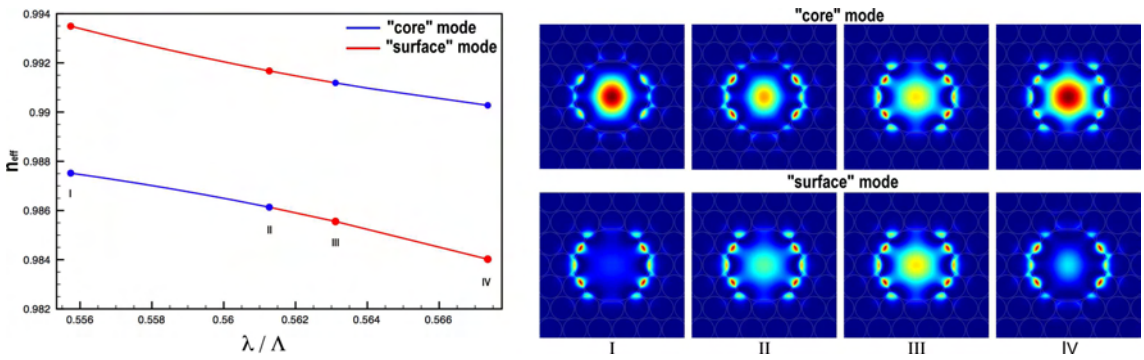

FIGURE 3.8: (*left*) Calculated dispersion of "core" modes and "surface" modes in the vicinity of the anti-crossing. (*right*) Modal plots of the modes at the indicated wavelengths.

3.3 Modelling HC-PBGFs

In the last years, various methods have been developed for the analysis of photonic crystal fibres. Although some the fundamental concepts used in conventional fibres modelling can still be used, the complex structure of the photonic crystal cladding requires the employment of full vectorial methods. Specially, photonic bandgap guiding fibres have been analyzed by novel methods which are related to the methods used for the calculation of bandgaps in semiconductors [32]. A brief description of the numerical methods used in this thesis to calculate the optical properties of hollow-core PBGF is presented in the following sections. A detailed description of the most widely used numerical methods for the analysis of photonic crystal fibres can be found in [92, 93].

3.3.1 Full vectorial plane wave expansion method

The plane wave method was the first accurate method for the calculation of band maps in photonic crystals [94]. Prove of this is that the first structure that had a photonic bandgap was found using this method [95], and now it is one of the most applied tools in the analysis of photonic bandgap fibres. To understand this method recall that in Fourier space the reciprocal lattice vectors form a complete orthogonal set and thus any function can be expanded as a linear superposition of them [96, 97, 98, 99]. In this way the optical modes $[\vec{H}_{\vec{k}}(\vec{r})]$ can be expressed as follows:

$$\vec{H}_{\vec{k}}(\vec{r}) = \sum_{\vec{G}} \sum_{\gamma=1,2} \vec{h}_{\vec{k}+\vec{G},\gamma} e^{j(\vec{k}+\vec{G})\cdot\vec{r}} = \sum_{\vec{G}} \vec{H}_{\vec{k}}(\vec{G}) e^{j(\vec{k}+\vec{G})\cdot\vec{r}} \tag{3.6}$$

where the basis functions are $e^{\vec{G}\cdot\vec{r}}$, with $\vec{G}$ being a vector of the reciprocal lattice, $\vec{k}$ is the wave vector, and γ represents the two polarizations of the field orthogonal to

$\vec{k} + \vec{G}$. Substituting equation (3.6) in equation (2.5), a system of linear equations for the expansion coefficients is obtained [92]:

$$-(\vec{k}+\vec{G}) \times \left[\sum_{\vec{G}'} \epsilon_r^{-1}(\vec{G}-\vec{G}')(\vec{k}+\vec{G}') \times \vec{H}_{\vec{k}}(\vec{G}') \right] = \frac{\omega^2}{c^2} \vec{H}_{\vec{G}} \tag{3.7}$$

where $\epsilon_r^{-1}(\vec{G})$ are the Fourier coefficients of ϵ_r^{-1}. Equation 3.7 represents an infinite set of equations for the eigenvectors $\vec{H}_{\vec{G}}$. Practically the sum is truncated at some point and the resulting finite set of equations constitutes a standard matrix eigenvalue problem that can be solved using any conventional eigenvalue solver. Many variations of the basic plane wave method had been realized, mainly differing in the way operations are realized and the eigensolver algorithm but containing the same fundamental elements [99, 91].

For the analysis of photonic bandgap fibres, knowledge of a complete map of all the modes allowed in the photonic crystal cladding is indispensable. Since *Plane Wave Expansion Methods* assume infinitely periodic structures they are ideal for this problem. In this thesis the freely available version developed by Johnson and Joannopoulos at MIT [91] is used to calculate bandgap diagrams and DOS plots. This particular implementation fixes the propagation constant β and solves for the frequency ω, therefore it is not possible to include material dispersion into the computation. An implementation of the plane wave expansion method which solves for the propagation constant for a fixed frequency has been developed by Pearce *et al.* [100].

To determine the existence of a photonic bandgap it is in principle required to calculate the frequencies of the modes for all possible $\vec{k}$ vectors. This corresponds to all the points inside and at the boundaries of the Brillouin zone. However, symmetries give rise to a further reduction on the $\vec{k}$ vectors that need to be considered. It is widely accepted that varying the $\vec{k}$ vectors along the periphery of the irreducible Brillouin zone is sufficient in order to determine the existence of a bandgap[4].

Since plane wave expansion results in a periodic electromagnetic field, it cannot be directly applied to the study of defects such as that shown in Figure 3.9(a). However, for this task the plane wave methods may still be applied if an auxiliary super structure that contains the defect and several periods of the photonic crystal is considered as the unit cell [101]. The real structure that is simulated with the supercell method Figure 3.9(b), is a periodic structure in which the defect and several periods are periodically repeated, for this reason the size of the supercell has to be large enough to guarantee that neighbour defects do not interact with each other.

[4]I have been unable to find a proof of this but it is universably accepted in the literature.

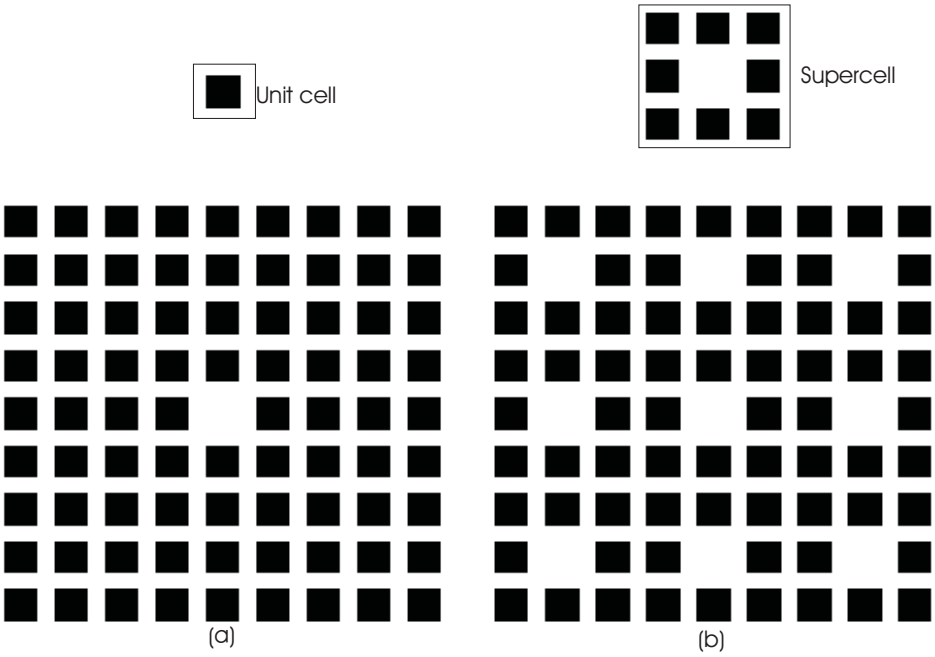

FIGURE 3.9: (a) Square unit cell and structure with a central defect. (b) Illustration of a supercell of size 3x3 required in order to simulate the central defect. In the structure considered using the supercell approximation the defect is repeated periodically.

A drawback of the PWEM is the high number of terms needed to accurately represent small features. This is particularly important when considering PBGF with strut thicknesses being less than one tenth of a wavelength while the core is tenths of wavelength across. For example Steel found that they needed 2^{17} terms to model a standard PCF [102]. Another draw-back of PWEMs is that they required a structured mesh therefore in order to accurately model complicated geometries a large number of terms is required. Hence, in this thesis I adopted the finite element method (FEM) described below to model the modes of HC-PBGFs.

3.3.2 Modelling realistic HC-PBGFs using finite element methods

3.3.2.1 Introduction

The finite element method for the solution of a boundary value problem is based mainly on:

- The variational or weak statement of the problem

- Approximation of the solution of the variational equations by means of the finite element functions

The starting point of this method is the strong or classical formulation of the boundary value problem, but in order to obtain approximate solutions we would need to express this formulation in a different way. To accomplish this, we use some type of functions called the *trial* and *weighting* functions. The former are functions that satisfy the boundary conditions and also that their derivatives shall be square integrable, while the latter are similar to the trial functions but now they satisfy the homogeneous part of the boundary conditions.
The weak or variational form of the boundary value problem is obtained when multiplying the strong formulation by the weighting functions and integrating over the domain. The next step is to approximate the weak formulation in a discretized domain, so the requirement is to approximate the collections of infinite trial and weighting functions by means of convenient collections of finite element functions. Then the variational equations are solved using these functions in the discretized region. The choise of the convenient trial and weight functions is free, the most widespread finite element method is based on the Galerkin method, where the same collection of functions is used to define the trial and weighting spaces.

The Galerkin method converts a partial differential equation into a system of ordinary differential equations. In order to exemplify this, we consider the boundary-value problem defined by a set of boundary conditions and the differential operator $\mathcal{D}$:

$$\mathcal{D}u = f \quad in \quad \Omega \tag{3.8}$$

If $\tilde{u}$ is an approximate solution of equation (3.8), its deviation from the exact solution is defined as:

$$\mathcal{R} = \mathcal{D}\tilde{u} - f \tag{3.9}$$

Clearly, a small residual $\mathcal{R}$ will correspond to a good approximate solution of equation (3.8) and $\mathcal{R}$ will be zero only for the exact solution.

Then $\tilde{u}$ is expressed as a discrete sum of a collection of functions

$$\tilde{u} = \sum_{i=1}^{N} \alpha_i \phi_i = \{\alpha\}^{\mathrm{T}}\{\phi\} \tag{3.10}$$

where ϕ_i are the basis functions, and α_i are the expansion coefficients. The basis functions are defined over the entire domain, and have to form a complete set that can

represent any function but do not need to be orthogonal. At this point, the approximate solution of equation (3.8) has been reduced to finding the coefficients α_i that minimize $\mathcal{R}$ in some average sense. As $\mathcal{R}$ is a continuous function over Ω, it is common to minimize a weighted integral of $\mathcal{R}$ calculated over the entire domain. A set of weighting functions w_i is chosen to use in evaluating the residual

$$\int_{\Omega} \mathcal{R} w_i \, d\Omega = 0 \qquad i = 1, 2, 3, ... \tag{3.11}$$

for the Galerkin method, the weighting functions are the same functions used for the expansion of the approximate solution equation (3.10)

$$w_i = \phi_i \quad . \tag{3.12}$$

Therefore, equation (3.11) can be written as

$$\sum_{i=1}^{N} \alpha_i \int_{\Omega} \phi_j \mathcal{R} \phi_i \, d\Omega - \int_{\Omega} f \phi_j \, d\Omega = 0 \qquad j = 1, 2, 3, ..., N \tag{3.13}$$

which can be written as a matrix equation

$$\left[\; S \; \right] \{\alpha\} = \{b\} \tag{3.14}$$

where the elements of the N x N matrix $\left[\; S \; \right]$ are

$$S_{ji} = \int_{\Omega} \phi_j \mathcal{R} \phi_i \, d\Omega \tag{3.15}$$

and the elements of the vector $\{b\}$ are

$$b_j = \int_{\Omega} f \phi_j \, d\Omega = 0 \tag{3.16}$$

Up to now, the techniques presented here have not said anything about finite elements, we have only transformed the original continuous problem equation (3.8) into a linear system with a finite number of integral equations and the method can be applied to any collection of basis functions. However, to obtain a good approximate solution, the basis functions have to be properly selected. Generally, global functions cannot fit the solution locally and functions satisfying the boundary conditions are extremely difficult to find. The FEM solves this problem by discretizing the domain into smaller regions (called finite elements) in which the expansion functions are defined and are zero outside

these regions. In order to accurately approximate u, these local functions do not need to be complicated and for example, can be defined as simple polynomials.

A detailed description of the FEM is not the objective of this thesis (for a more comprehensive discussion of its application to electromagnetics the reader is refered to [103]. Here the FEM was used as a tool to analyze PCFs. Comsol Multiphysics [104] a powerful commercially available package was adapted to the specific problem of HC-PBGF. Comsol is a commercial implementation of the FEM for modelling engineering and scientific problems based on partial diferential equations. The software package incorporates all the tools required for the FEM modelling process. It contains CAD tools for structural design, mesh generation tools, a vast range of optimized solvers for sparce matrices and visulization and postprocessing tools. It can also be integrated with Matlab allowing for the control of the modelling process. Some details of the FEM used in this thesis are discussed in the following section.

3.3.2.2 Simulation settings

The accurate description of the fibre's transverse profile is essential to obtain reliable simulation results and in our model we have tried to resemble fabricated fibres as close as possible. The structural model used in this thesis for the numerical computation of the optical properties of hollow-core PBGFs is presented in Figure 3.10. As described in section 3.2.1 the cladding of fabricated fibres can be accurately represented by hexagonal holes with rounded corners arranged in a triangular lattice. The width of the hexagons is d, and the corners are rounded with circles of diameter d_c. The distance from hole centre to hole centre is Λ. The cladding holes form complete rings surrounding the core, as in Figure 3.10(a,b). The core is formed by the omission of 7 or 19 unit cells. The hollow-core is then surrounded by a thin silica wall. The computations in chapters **??** demonstrate that the specific geometry of the core wall has a large influence on the optical properties of the fibres. Therefore, the exact details of the core/cladding interface in the model have to be controlled. In the model of Figure 3.10, the core is defined by a non-circular ring of nearly constant thickness t_c at the boundary with the cladding, and a core radius R_c. The corners of the pentagons surrounding the core are rounded using circles of diameter d_p.

HC-PBGFs based on a triangular lattice, as the ones shown in Figure 3.10 belong to the C_{6v} point group and therefore have six fold rotation symmetry and mirror symmetry [105, 106, 107, 108]. The modes supported by the fibre either exhibit the full waveguide symmetry and are nondegenerate, or appear in degenerate pairs that support this symmetry only in combination. The fundamental mode is HE_{11}-like and so

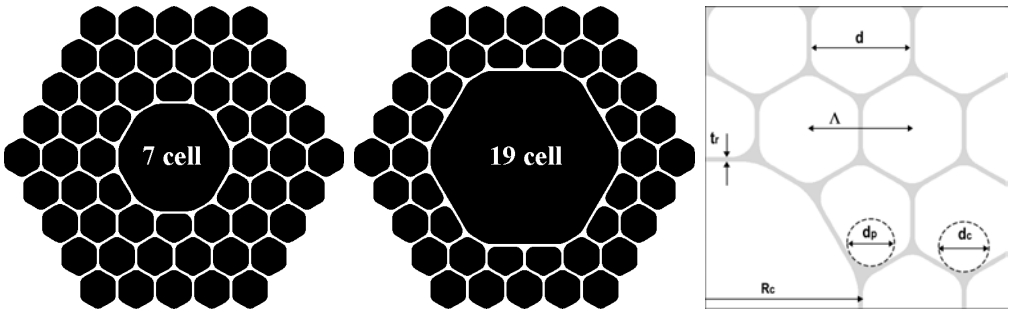

FIGURE 3.10: Structural model of realistic HC-PBGF, the cladding is a triangular array of rounded hexagons and the hollow core is formed by (a) 7 and (b) 19 missing holes. (c) Parameters used to define the structure.

it is two-fold degenerate and can be computed by using a $\pi/2$ sector of the fibre structure, Figure 3.11. By calculating the optical modes only in this fibre sector many higher order modes which are not relevant for most of the studies in this thesis, since they are less concentrated in the hollow-core and experience much higher attenuation, are directly excluded from the computation. Non-degenerate eigenmodes of the fibre can be obtained by computing the field in just a $\pi/6$ fibre sector.

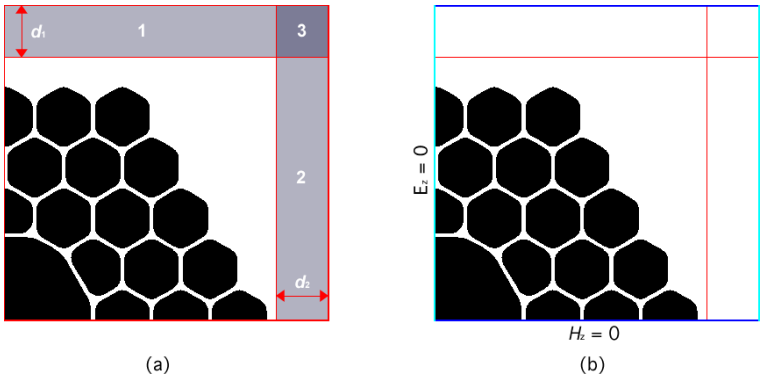

FIGURE 3.11: Fibre cross section surrounded by PMLs. (a) Subdomain definition, and (b) setting of the boundary conditions.

Contrary to the assumption of the plane wave expansion method, photonic crystal fibres have a finite crystal cladding and all propagating modes are leaky. It is therefore possible to calculate the confinement loss -the losses due to the finite size of the cladding- of the propagating modes by surrounding the fibre structure by Perfectly Matched Layes (PML) [109, 110, 77], as in Figure 3.11. However, it has been demonstrated that hollow-core photonic bandgap fibres with large air-filling fractions, as the fibres of interest in this thesis, require no more than 6 to 7 rings of cladding holes in order to reduce the confinement loss to a negligable value [109, 77]. The numerical simulation of hollow-core PBGFs presented in this thesis considers enough ring of holes to ensure low confinement loss, and therefore confinement loss is neglected to evaluate the performance of the fibres.

In the model, Perfectly Matched Layes [gray regions in Figure 3.11(a)] are intoduced to limit the computational domain and avoid reflections from the outer boundaries. PMLs absorb electromagnetic radiation independently of the angle of incidence, polarization and wavelength of the incoming wave [111, 112, 113, 114]. The initial PML technique, proposed by Berenger [111], involves a local modification of Maxwell's equations based on the splitting of the field components into two components. Alternatevely a much easier implementation which defines the material in the PML regions as anisotropic and complex without the need of field splitting was proposed in [112]. The PML regions, are defined as anisotropic materials whose permittivity and permeability tensors [112, 110] are:

$$\varepsilon = \varepsilon_0 n^2 S\,, \tag{3.17a}$$

$$\mu = \mu_0 S \tag{3.17b}$$

with

$$S = \begin{bmatrix} s_y/s_x & 0 & 0 \\ 0 & s_x/s_y & 0 \\ 0 & 0 & s_x s_y \end{bmatrix} \tag{3.18}$$

where ε_0 and μ_0 are the permittivity and permeability of free space, n is the refractive index of the region adjacent to the PML (glass in this case). The PML parameters s_x and s_y are given in table 3.1 for regions 1, 2, and 3 in Figure 3.11(a).

PML parameter	PML region 1	2	3
s_x	1	s_2	s_2
s_y	s_1	1	s_1

TABLE 3.1: PML parameters.

The values of s_i (i =1, 2) are:

$$s_i = 1 - j\alpha_i \left(\frac{\rho}{d_i}\right)^2 \tag{3.19}$$

where ρ is the distance from the beginning of the PML, d_i is the PML width in the vertical and horizontal direction, and the attenuation of the field in the PML regions can be controlled by appropriately choosing α_i.

At the edges of the computational domain Figure 3.11(b), the following boundary conditions are set: short circuit (zero tangential electric field) or open circuit (zero tangential

magnetic field). The particular combination of boundary conditions allows to distinguish between the different modal classes that can be calculated in the analyzed fibre sector. The horizontally polarized mode is calculated with the boundary conditions shown in Figure 3.11(b), while for the vertically polarized mode the boundary conditions are exchanged.

Within Comsol several parameters can be ajusted to generate a triangular mesh. In order to sample the complicated structure of HC-PBGFs, a fine grid is needed at the core/cladding interface where high accuracy is needed, and around curved boundaries. Comsol also includes adaptative grid refinement algorithms that automatically refine the mesh at certain parts of the geometry. The convergence behaviour with respect to the number of triangles and the mesh parameters has been studied in order to validate the solutions of the FEM solver. Comsol includes several linear system solvers which enable a fast computation of the modes by exploiting the sparseness of the matrices resulting from the finite element formulation of the wave equation. The direct linear system solver UMFPACK has been used because it generally provides the fastest solution. Once all the paremeters are set, eigenvalues and mode fields around a user defined guess eigenvalue are computed.

During this PhD project, Matlab scripts that generate the fibre geometry, control the mesh, and set the boundary conditions and solver parametres have been developed. Using these scripts it is possible to find and track a specific mode across wavelength for the calculation of dispersion curves, and the evolution of various fibre parameters as a function of wavelength. The scripts automatically modify the structure if the fibre properties as a function of the fibre geometry are studied, as reported in the next chapters.

Chapter 4

Design of low-loss, broadband hollow-core PBGFs free of surface modes

In previous chapters it was shown that the existence of high-attenuation surface modes localized to the core cladding interface is a major limitation for the development of low loss hollow-core PBGFs with broad transmission spectra. In current state-of-the-art fibres, these surface modes couple with the core guided mode in specific spectral ranges inside the bandgap, decreasing the effective bandwidth of the fibres and also increasing the dispersion and dispersion slope. In this chapter, hollow-core PBGFs incorporating realistic core designs are systematically studied in order to identify new design regimes that are robust in eliminating surface modes. New hollow-core PBGFs designs that do not suffer from surface mode coupling within the photonic bandgap formed in the cladding are proposed. The absence of surface modes enables low attenuation over the full spectral width of the photonic bandgap - for the particular fibre analyzed here, 17% of the central bandgap wavelength is achieved. As a result of the increased bandwidth, these new fibre designs also present reduced dispersion and dispersion slope. These properties are important for several applications of hollow-core PBGFs to high-power ultrashort pulse compression and delivery [115, 67, 66, 116, 65].

Furthermore, the analysis presented in the following sections provides physical arguments for understanding ways to remove the impact of surface mode on the guidance of hollow-core PBGFs. In order to remove surface modes, one needs to design fibres in which the cladding structure terminates as naturally as possible at the core/cladding interface. Although in this chapter, only fibres featuring a core size of seven unit cells and moderately high air-filling fractions in the cladding are analyzed, extension of this

understanding to fibres with larger or smaller core sizes, and higher cladding air-filling fractions promises a new range of hollow-core fibres free of surface modes with improved performance compared to those previously reported.

4.1 Introduction

Currently, the wavelength range over which state-of-the-art hollow-core PBGFs can guide light is not limited by the size of the photonic bandgap formed in the cladding but by the existence of surface modes [76, 78, 75, 15]. As has been previously presented, the coupling of energy between these high-attenuation surface modes and core modes result in absorption peaks in the measured attenuation spectrum of all reported fibres [76, 78, 75, 15, 80]. Moreover, these interactions can drastically reduce the fibre's transmission bandwidth, making the presence of surface modes the major limitation for the development of air-silica PBGFs with a broad transmission spectrum. In a hollow-core fibre the photonic bandgap is determined uniquely by the cladding and therefore the maximum achievable bandwidth is fixed by the cladding structure. However, the fibre's useful bandwidth is determined by the core shape and in particular whether or not surface modes are supported and the density of these surface mdoes. Therefore, one way of increasing the transmission spectrum of previous hollow-core photonic band gap fibres is to design and fabricate fibres with new core structures that do not support surface modes or at least by "moving" them towards the bandgap edges so as to minimize their impact on the air-guided mode.

The problem of minimizing the impact of surface modes in the guidance has attracted much attention and several studies have been carried out in order to understand their nature and ways to eliminate them [117, 118, 119, 77, 76, 120, 121, 122]. For example, Digonnet *et al.* proposed that cores formed by terminating the periodic photonic crystal cladding with a perfectly circular hole can suppress the presence of surface modes if the core radius is chosen properly [118, 119]. This study has provided insights to the physical origin of surface modes which have helped to understand how the core defect can introduce strong perturbations to the cladding bulk modes and introduce surface modes. They have showed that when the core cuts only through the thin silica struts of the photonic crystal, no surface mode is induced and a simple geometric criterion to predict the existence of surface modes was proposed [119]. Figure 4.1 shows a periodic array of holes and highlights the range of core radii that should produce surface mode free fibres. In this figure, the grey regions represent the ranges of core radii that intersect the silica nodes of the photonic crystal cladding, and thus support surface modes, and the white regions between them are the surface mode free bands. These results obtained

by Digonnet's group are very important, however, they do not address the problem in real fibres.

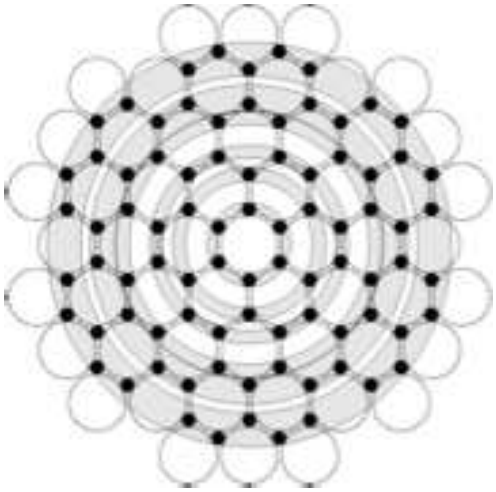

FIGURE 4.1: The grey regions represent the ranges of core radii that intersect rods, and thus support surface modes, and the white regions between them the surface-mode-free bands. After [119].

After having identified surface mode free designs, the same authors studied the effects that adding a circular silica ring around the hollow-core has on the guidance properties of these surface mode free fibres [117], Figure 4.2 shows a cross-section of the fibre studied in [117]. It was suggested that the addition of a circular silica ring at the core-cladding interface always introduces surface modes. However the impact of these surface modes can be reduced if the thickness of the wall is properly chosen [117]. Yet even with the addition of the silica ring, these core designs do not resemble those ones of real fibres and cannot be readily fabricated with the current fibre manufacture technology. In contrast fabricated fibres always have a non-circular silica ring at the core-cladding boundary, and similarly variations in the core size deform the ring of holes immediately surrounding it. Consequently a proper investigation resembling realistic structures of the critical core-cladding interface region is needed to successfully address the problems of surface modes in feasible fibres [123, 121].

In this chapter a detailed study of idealized but realistic silica hollow-core PBGFs structures is presented. Realistic means that it should be possible to fabricate them by stack-and-draw method. The impact that key structural parameters have on the fibre's transmission performance is investigated and a new design regime of fibres with a fundamental core mode robustly free of anticrossings with surface modes for all frequencies within the bandgap is identified.

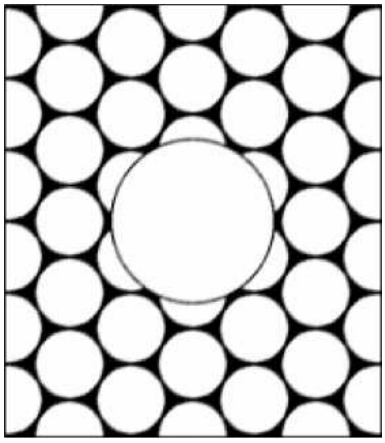

FIGURE 4.2: Cross-section of an air-core photonic-bandgap fibre with a thin silica ring around the core. After [117].

4.2 Fibre structure and design space

This study targets the design of realistic silica 7-cell core hollow-core PBGFs with a low-loss broad transmission spectrum. Firstly, it has to be considered that the width of the optical bandgap is strongly correlated with the air filling fraction of the cladding and the maximum achievable transmission bandwidth will be fixed by the cladding structure. Then it should also be considered that the core defect has to resemble that of fabricated fibres. Therefore, the cladding of the analyzed fibres is an array of hexagonal holes with rounded corners in a silica matrix with a moderately high air filling fraction and the core is formed by seven missing unit cells surrounded by a non-circular silica ring of radius R_c and a constant thickness t_r. The fibres analyzed here have been represented via the 7-parameter model in Figure 3.10.

During the fabrication of hollow-core PBGFs, the shape of the central air-guiding defect can be (to certain extend) independently controlled from the cladding. Indeed, while maintaining the cladding structure unchanged, it is possible to modify the size (R_c) of the hollow-core and the thickness of the "core wall" -the silica ring surrounding the core- (t_r). For example, the core can be expanded or compressed relative to its original size in the preform by modifying the drawing conditions -one way of doing this is by directly applying different pressures to the core and cladding. The thickness of the core wall will be determined by the thickness of the central core tube used in the stack. However, if required, very thin core walls could be achieved by a subsequent chemical etching step before the final draw to fibre. Hence it is obvious to investigate the effects of the variations of these two structural parameters on the fibre's transmission performance.

In order to accurately model realistic fibres of different core sizes, compressions and expansions of the core were modelled considering that only the first ring of holes is

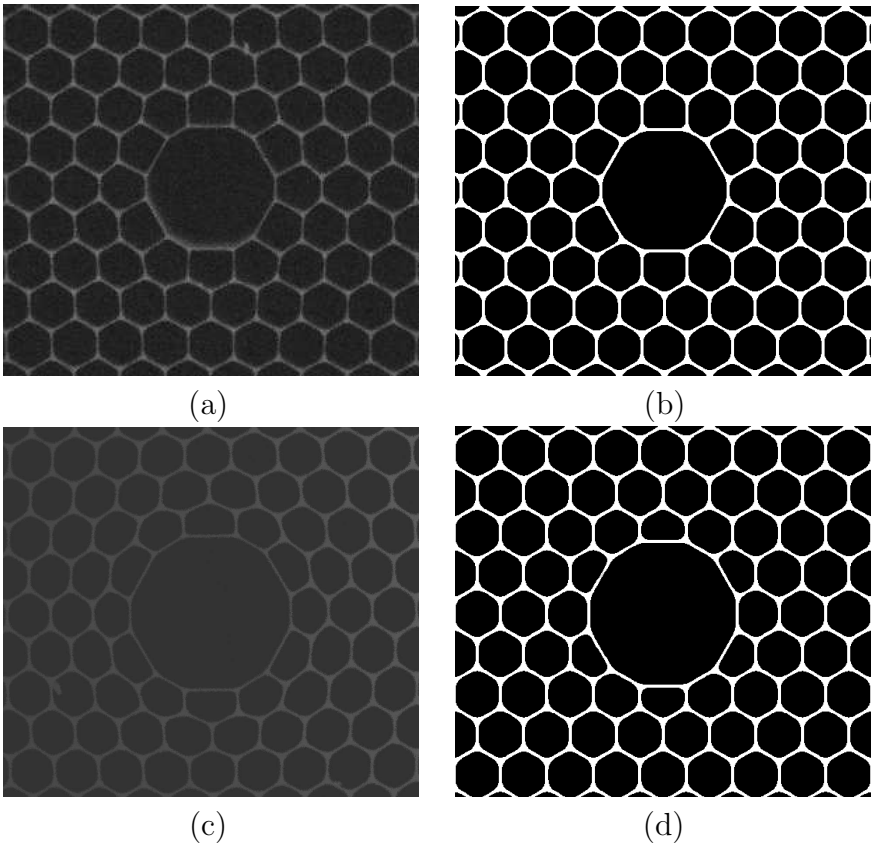

FIGURE 4.3: (a) and (c) SEM images of hollow-core PBGFs with compressed and expanded cores respectively - the fibres were fabricated at the ORC by Dr. Marco Petrovich. (b) and (d) modelled structures that resemble the fabricated fibres, with parameters $d/\Lambda = 0.95$, $d_c/\Lambda = 0.55$, $d_p/\Lambda = 0.317$, normalized ring thickness $T = 1$, and expansion coefficient of 94% for (b) and 106% for (d).

affected while the rest of the cladding is kept unchanged. This assumption was justified based on experimental observation, as shown by SEM micrographs of PBGFs fabricated at the ORC with expanded and compressed cores in Figure 4.3. The SEM of the fibre with a compressed core in Figure 4.3(a) presents a minimal distortion of the cladding structure beyond the first ring of holes. For the fibre with an expanded core a certain degree of distortion is observed for the second ring of holes. However this distortion should have little/or no impact on the surface modes since they are tightly confined to the silica ring around the core. Therefore it is reasonable to believe that considering this distortion would not change the conclusions of the study.

The idealized representations of the fabricated fibres, obtained from the model are shown in Figure 4.3(b)(d). The modelled fibres strongly resemble the fabricated fibres suggesting that the designs obtained from this study are feasible targets for in-house fabrication. Note that changes on the thickness of the ring do not affect the parameter R_c since it is measured from the centre of the fibre to the boundary of the first cladding hole. Normalized variations of R_c were considered by defining an expansion coefficient E:

$$E = \frac{R_c}{\frac{3\Lambda}{2} - \frac{\Lambda - d}{2}} \tag{4.1}$$

where values of $E < 1$ (100%) correspond to fibres with compressed cores and values larger than 1 to fibres with enlarged cores. It is also useful to normalize the thickness of the core boundary with respect to the thickness of the thinnest features in the cladding (the thin silica struts in the cladding):

$$T = \frac{t_r}{\Lambda - d} \tag{4.2}$$

Figure 4.4 shows some of the different fibre structures that can be generated by modifying the structural parameters T and E. In Figure 4.4(a) the core size is fixed to an ideal value ($E = 100\%$) and the thickness of the core wall is modified. Figure 4.4(b) shows fibres for different core expansion coefficients and a constant core wall thickness of $T = 1$.

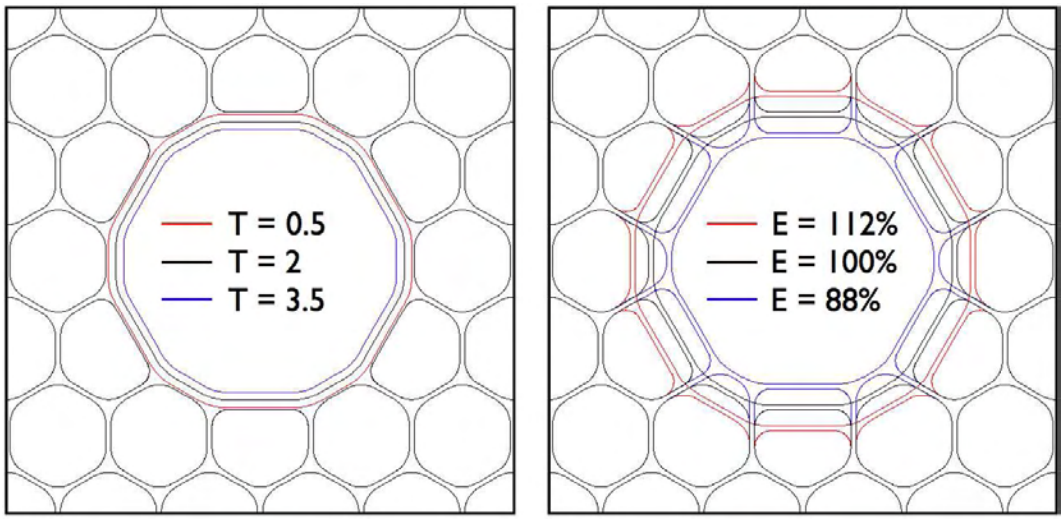

(a) (b)

FIGURE 4.4: Idealized fibre structures genereted with the model with: (a) $E = 100\%$ and different T values; and (b) $T = 1$ and different values of E.

4.3 Evaluation of the fibre's transmission performance

Once that the design space has been selected and the core geometry has been parameterised in terms of E and T, the cladding parameters that will be used throughout

the study were selected. According to detailed structural analysis performed by SEM on fibres fabricated by Dr. Marco Petrovich at the ORC, typical cladding parameters are $d/\Lambda = 0.95$ and $d_c/\Lambda = 0.55$. Therefore, in this study those cladding parameters were chosen and should be realistic targets for in-house fabrication. A hole-to-hole distance $\Lambda = 4.3$ μm was chosen to obtain a bandgap centred at ≈ 2 μm, although the results presented here are more general and can be transposed to other wavelengths by simply scaling the structure, and modifying the refractive index via the Sellmeier equation (A.2).

As described in previous sections, an increase in the fibre's attenuation is always observed at wavelengths near to an avoided crossing with surface modes [76]. Thus each time that surface modes interact with a core guided mode, an attenuation peak in the fibre's transmission spectrum appears, and the fibres useful bandwidth is correspondingly reduced. Initially the fibre with an un-optimized core wall of normalized thickness $T = 1$ shown in Figure 4.5 was modelled. The optical modes within the bandgap were calculated and are presented in Figure 4.6. Blue curves in Figure 4.6(a) show the effective index of the fundamental air-guided mode as a function of wavelength while red curves correspond to a surface mode of the same symmetry class, and the green shaded region represents the photonic bandgap of the caldding.

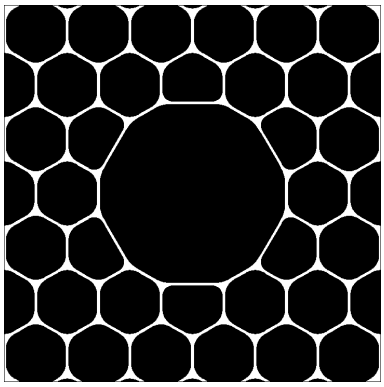

FIGURE 4.5: Cross section of a modelled PBGF with $d/\Lambda = 0.95$, $d_c/\Lambda = 0.55$, $d_p/\Lambda = 0.317$ and $t_r/(\Lambda - d) = 1$, (b) geometric parameters used to define the structure.

This un-optimized fibre supports one surface mode that couples to the fundamental mode within the bandgap at $\lambda = 2.13$ μm. As has already been discussed, away from the avoided crossing point (i), the fundamental mode localizes most of the optical power in the hollow-core whilst the surface mode [eg. point (iv)] is tightly confined in the glass region surrounding the core, as clearly seen from the modal field profiles in the lower panel of Figure 4.6. Near to the anticrossing [eg. point (ii)] the modes hybridize and cannot be differentiated as "true" air-guided modes or as "true" surface modes since at these wavelengths both modes concentrate energy in the hollow-core and in the core wall [76, 77]. Hence, the impact of the modal interaction can clearly be seen as a

dip/peak in the percentage of power in the core/*F-factor* of the fundamental core mode Figure 4.6(b). Furthermore, near the bandgap edges, where the cladding is no longer able to confine the mode in the hollow-core, the power in core and the *F-factor* sharply drop and rise respectively[1]. Therefore the fraction of core confined energy/*F-factor* of the fundamental core mode against wavelength provide a useful qualitative estimation of the fibres transmission/attenuation spectrum and thus can be used to approximate the fibre's operational bandwidth.

Away from anticrossing wavelengths, the loss in PBGFs is ultimately limited the scattering at the glass/air interfaces due to surface roughness [79, 80, 81]. Even though this loss is unlikely to be completely eliminated, it can be reduced by decreasing the overlap of the fundamental mode with the glass. This surface scattering loss is proportional to the *F-factor*, and thus reducing *F-factor* implies a reduction of the fundamental limit of loss in HC-PBGFs. In the following sections, the transmission performance of the fibres as a function of the core shape will be evaluated by using the energy confined by the fundamental mode in the core region and the *F-factor* since these two parameters suffice to identify low-attenuation designs, and since both factors critically depend on whether or not surface modes exist and provide a simple way to estimate the useful bandwidth.

In the following calculations a full-vector finite element method was used to accurately and efficiently solve Maxwell's equations described in section 2.1. The dielectric properties of silica were directly included in the model through the Sellmeier equation (A.2). Since this study only focuses in the fundamental air-guided mode and surface modes belonging to the same symmetry class only one quarter of the fibre was modelled (note that modes of different symmetry classes do not strongly interact due to realistic perturbations to the fibre structure). It also should be noted that the fibres studied here support higher order core modes however these modes are not relevant to the study since they are orthogonal to the fundamental core mode and do not interact with it. In order to accurately calculate the interactions between surface modes and the core mode, the mesh size was adapted to obtain convergence of the propagation constants of both core and surface modes. Typically meshes with ~ 10 elements within the core wall have been used, as in Figure 4.7.

Summarizing, the aim of this study is to design core structures that suppress surface modes. By eliminating the effects of surface modes on the guidance, the fibre's operational bandwidth is increased and the attenuation due to mode coupling mechanisms is reduced [76]. An increased bandwidth will also mean that the variation of other fibre parameters (such as group velocity dispersion) with wavelength will be slower. In addition, in order to reduce the dominant loss factor at wavelengths where the interactions

[1] The *F-factor* is defined as the overlap integral of the fundamental air-guided mode with the silica surfaces equation (3.3).

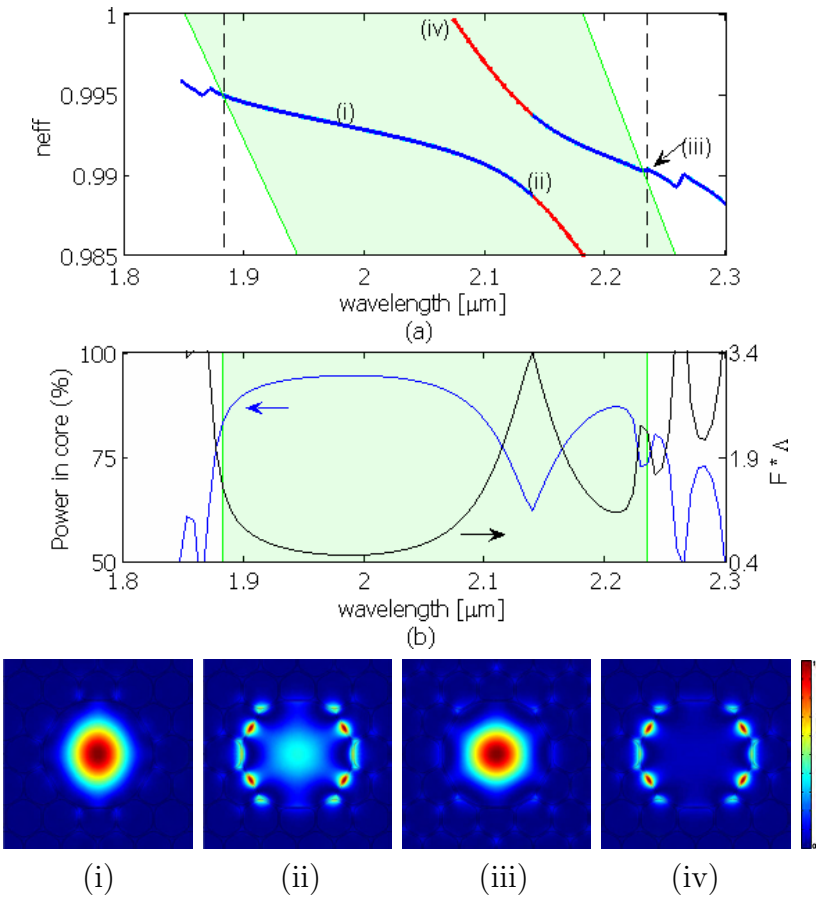

FIGURE 4.6: (a) Effective index of modes (blue for FM and red for SM). (b) Fraction of core-confined energy of the FM (blue) and factor F (black) of the FM *vs.* wavelength for a fibre with $T = 1$ and $E = 0$. Plots of the axial component of the Poynting vector: (i), (ii), and (iii) are of the FM "far" from the anticrossing, at the anticrossing point and near the long wavelength bandgap edge respectively, and (iv) is for the SM.

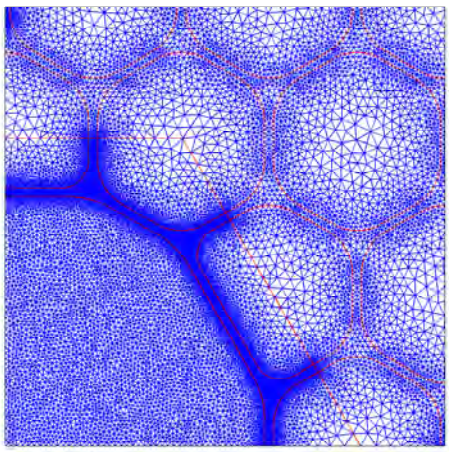

FIGURE 4.7: Typical mesh used for the calculations.

with surface modes is weak, these designs should ideally minimize the *F-factor* at the same time [79, 80].

4.4 Results

4.4.1 Impact of variations in the thickness of the core ring on the guidance

A systematic investigation of the impact that variations in the thickness of the silica ring surrounding the hollow-core have on the fibre's transmission properties is conducted in the first part of this study. For a fibre with an ideal core size E = 100%, the normalized ring thickness is scanned in the range $0.175 \leq T \leq 3.5$. This range has been chosen to reflect the range of possible fibres that can be fabricated with current technologies. For example, fibres with $T > 0.6$ can be obtained by stacking an extra tube to form the core, while fibres with $T \approx 0.5$ by simply omitting the extra core tube in the stack, and extremely thin core walls ($T < 0.4$) could in principle be formed by an additional chemical etching step to the canes. The modes of the resulting fibre geometries are solved for wavelengths within the photonic bandgap and near to the bandgap edges (1.9 μm $\leq \lambda \leq$ 2.3 μm) in small wavelength steps (5 nm), in order not to miss out narrow surface modes crossings. In order to assess the performance of the various designs, the percentage of power in the core and the *F-factor* of the fundamental air-guided mode are calculated. The results of the numerical computations are presented as a function of the normalized ring thickness T and of the wavelength λ in the two dimensional design maps of Figure 4.8. Note that in these design maps each horizontal line corresponds to a particular core design (a different fibre). For the power in the core map shown in Figure 4.8(a), red areas (power in the core $\geq 90\%$) correspond to regions where the fundamental mode is tightly confined in the core and therefore presents low confinement loss; the yellow diagonal lines, where the mode presents lower core confinement (power in the core $\approx 60\%$), correspond to anticrossings between the fundamental mode and surface modes - some lines appear dis-continuous in the graph due to the discrete number of T values considered; green regions (PinC $\approx 50\%$) correspond to wavelengths where the fundamental mode is outside the bandgap and extends into the cladding, i.e. it coexists with cladding modes as shown in Figure 4.6.(iii). Finally, the regions where the fundamental air-guided mode is no longer supported are shown in blue.

Similarly, the map in Figure 4.8(b) shows the normalized field intensity at the air-glass interfaces, plotted in dimensionless units $F\Lambda$. In this map blue areas ($F\Lambda \leq 1$) correspond to regions of high confinement of the fundamental mode, cyan lines ($F\Lambda$

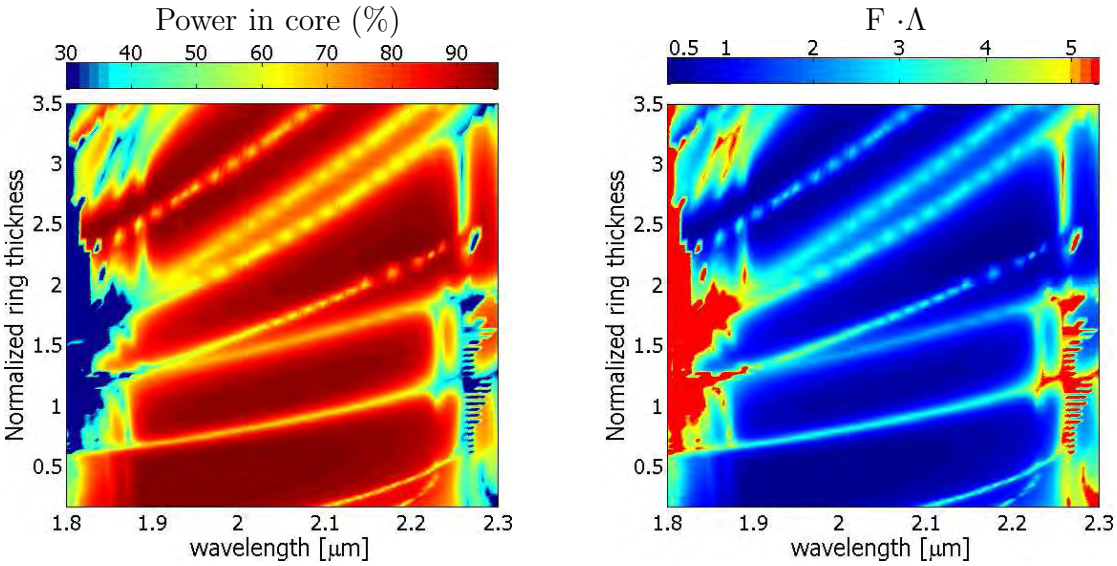

FIGURE 4.8: (a) Fraction of core-confined energy and (b) factor F of the fundamental core mode *vs.* normalized ring thickness and *vs.* wavelength, for un-expanded cores ($E = 0$).

≈ 3) to anticrossings points with surface modes and therefore high loss regions, and red to areas are represent points where a fundamental air-guided mode is no longer supported. As expected, both maps in Figure 4.8 provide very similar information: high power in the core areas correspond to low *F-factor* areas, while weakly confined modes present low values of power in core and large *F-factor* values. The main objective of this study is to identify designs that suppress surface modes and reduce the fibre's loss. In the maps of Figure 4.8, designs with those characteristics will appear as continuous horizontal regions with either high power in the core or low *F-factor* that are not crossed by diagonal lines.

From the maps in Figure 4.8 it is clear that the thickness of the core wall is a critical design parameter since it has a great influence on the density and frequency of surface modes which appear in the bandgap. For example, it can be immediately noticed that the fibre with a core ring of thickness $T = 0.175$ (the lowest value considered in this study) supports two surface modes that couple with the fundamental core mode near the long wavelength bandgap edge at $\lambda = 2.1$ μm and $\lambda = 2.19$ μm, while near the short wavelength edge of the bandgap this fibre does not support surface modes. Similarly, for most values of T multiple surface modes appear within the photonic bandgap in all cases reducing the operational bandwidth of the fibres. In clear contrast, Figure 4.8 also shows that there are two important design regions for which the spectral range over which the fundamental air-guided mode is free from anticrossings with surface modes is maximized. The first one occurs for core surrounds of thickness $T \approx 0.5$ and the second for $T \approx 1.15$. However, fibre designs with T around 0.5 provide a higher confinement of

the core mode, a smaller overlap of the fundamental mode with the glass-air interfaces and seem to provide the widest possible operational bandwidth. Remarkably, the silica glass wall around the hollow-core in the thin core wall fibre ($T = 0.5$) is just around 100 nanometres thinner than for conventional designs ($T = 1$). However, this tiny structural change completely removes surface modes from the bandgap region.

In order to understand why fibres with $T \approx 0.5$ reduce the impact of surface modes, Figure 4.9(right) shows the evolution of the dispersion curves of the fundamental and surface modes as the thickness of the core boundary increases from $T = 0.175$ to $T = 0.7$. Solid lines correspond to the effective mode index of the fundamental air-guided mode while dashed lines correspond to surface modes. As it can be observed from Figure 4.9(a), the addition of glass to the core-cladding interface (modifying T from 0.175 to 0.4) produces an increase in the effective mode index of the surface modes. Indeed, this increase in effective index is larger for surface modes than for core modes as they are localized in the silica ring. Thus the anitcrossing points between the fundamental mode and surface modes are shifted towards the long wavelength edge of the bandgap which in turn increases the fibre's operational bandwidth. Additionally, as the separation in effective index between the interacting modes decreases, the strength of the coupling should be weaker [124]. If T increases still further, the surface modes are progressively shifted beyond the long wavelength edge of the bandgap, see Figure 4.9(b) where they remain as bulk modes of the photonic crystal cladding and do not affect the guidance. However, when the thickness of the core surround is just half the thickness of the thinnest features (struts) in the cladding, i.e. $T = 0.5$, only one weak anticrossing event occurs inside the bandgap and the fundamental mode of a PBGF with $T = 0.6$ is completely free of anticrossings with surface modes for all wavelengths within the photonic bandgap. Increasing the thickness still further results in a structure that supports a new surface mode appearing on the short wavelength edge of the bandgap along with a corresponding decrease in the operational bandwidth of the fibre [the mode profile of this new surface mode is shown in Figure 4.9(b)].

The shift in the position of the surface modes can also be seen in Figure 4.10 which plots the *F-factor* (top) and the power in the core (bottom) for fibres with $T = 0.175$, 0.5 and 0.7. The fibre with $T = 0.175$ presents distinct peaks in $F\Lambda$ and dips in the power in the core indicating coupling to surface modes. By increasing the ring thickness to $T = 0.5$ these surface modes are "pushed" beyond the bandgap edge. As a result, neither the *F-factor* nor the power in the core of the fibre with T = 0.5 present signs of surface modes anticrossing resulting in smooth curves right across the bandgap. Again as before, the reduction of useful bandwidth due to a new surface mode appearing on the high frequency edge of the bandgap is clearly observed for the fibre with $T = 0.7$.

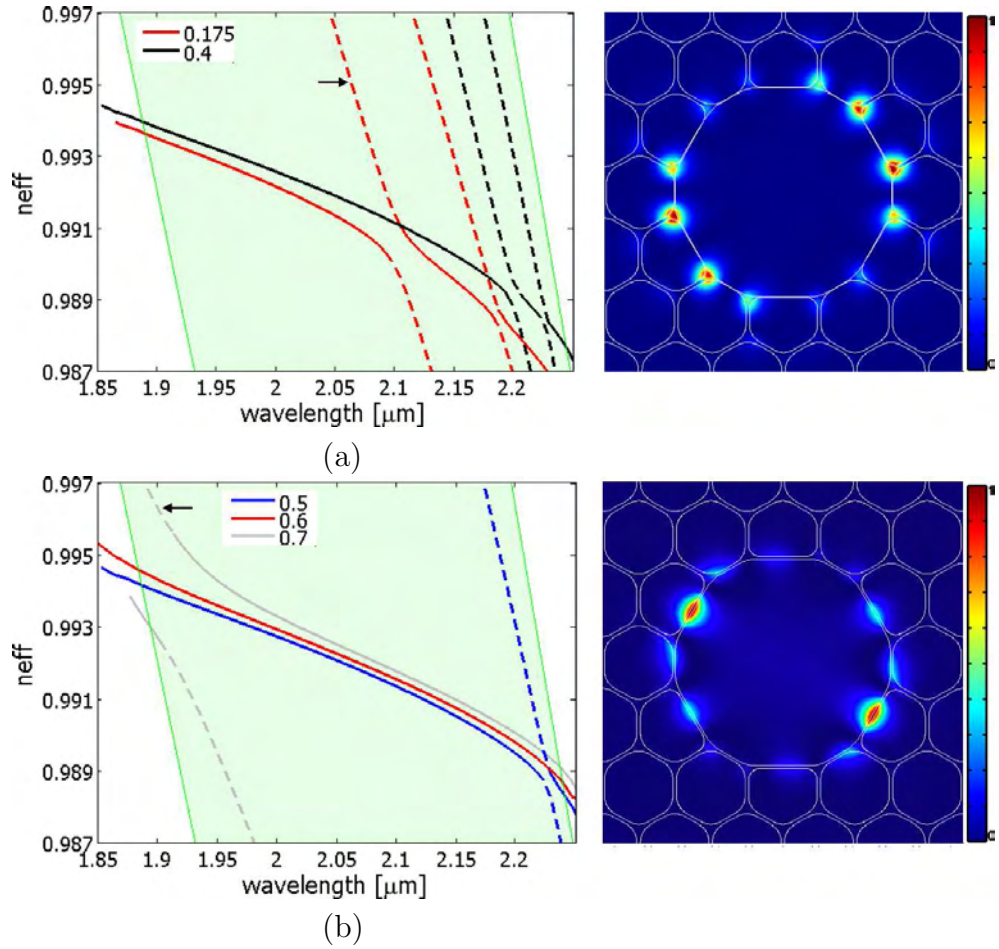

FIGURE 4.9: Dispersion curves of the fundamental mode (solid lines) and surface modes (dashed lines) for fibres with (a) $T = 0.175$ and 0.4, (b) $T = 0.5$, 0.6 and 0.7. (*right*) Mode profiles of the surface modes located by arrows.

The appearance of this design region free of surface modes can be explained as follows. Termination of the cladding periodicity to create the air core without adding a silica ring ($T = 0$), perturbs the photonic crystal in such a way that only surface modes with intensity maxima located at the nodes of the photonic crystal are supported (i.e. thicker dielectric parts between three adjacent holes), as described by Kim and Digonnet *et al.* [119, 118]. The intensity profile of a surface mode localized at the nodes of the photonic crystal is shown in Figure 4.9 (a), which corresponds to the mode supported by a fibre with $T = 0.175$ and pointed by an arrow. When a thick enough silica ring ($T = 0.7$) is added, the structure is perturbed strongly enough to support a new type of surface mode, which concentrates energy at the thin silica struts of the core boundary, see Figure 4.9(b). However, within this study it was found that between these two fibre designs there is an intermediate design regime that induces a perturbation that is too weak to support surface modes of the second type but strong enough to increase the effective mode index of surface modes of the first type and shift them outside the photonic bandgap. Therefore, if the thickness of the silica ring is properly chosen (i.e.

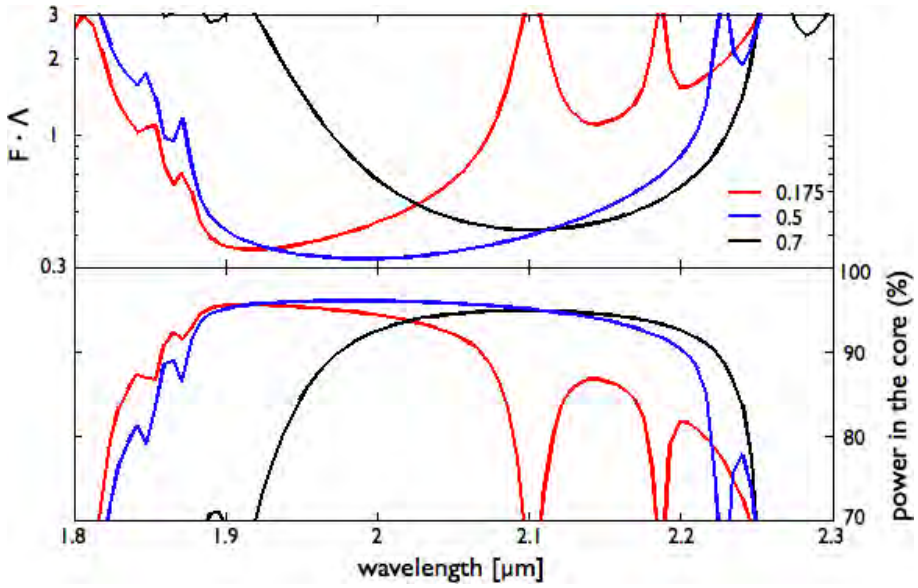

FIGURE 4.10: Plots showing the shift in the position of the surface modes as T varies. (top) *F-factor* and (bottom) power in the core *vs* λ for fibres with T = 0.175, 0.5 and 0.7.

$T \approx 0.5$) surface modes do not appear across the bandgap.

As previously mentioned, much effort in designing hollow-core PBGFs has been focused towards reducing the fibre attenuation, and impressive experimental progress has been reported by the group at the University of Bath and Corning Inc. [15, 78, 75]. However, optimizing the attenuation has relied on engineering the core wall - so as to minimize the overlap of the guided mode with the glass surfaces thus reducing surface scattering [80]. But in doing so extra glass has always been added at the core cladding interface and surface modes have been introduced into the bandgap and the spectral windows within which the loss is low become narrow. On the other hand, the fibres proposed here are different to those previously reported since this study found that in order to remove the impact of surface modes on the guidance, one needs to design and fabricate a fibre in which the cladding structure terminates as naturally as possible at the core-cladding interface. And one way to do this is to simply form the core by terminating the cladding at the natural edge of a unit cell ($T = 0.5$) without the addition of extra glass. Figure. 4.11 shows a periodic arrangement of unit cells, if the periodic structure is terminated at the edge of the unit cells around the core (i.e. red unit cells are removed to create the core), then the thickness of the glass left at the core boundary is just half the thickness of the struts in the cladding. This This understanding of the mechanisms that remove surface modes from the bandgap will be applied to different fibre structures in chapter 5. It is expected that extension of this design to fibres with different core shapes promises a new range of hollow-core fibres free of surface modes with improved performance compared to those previously reported.

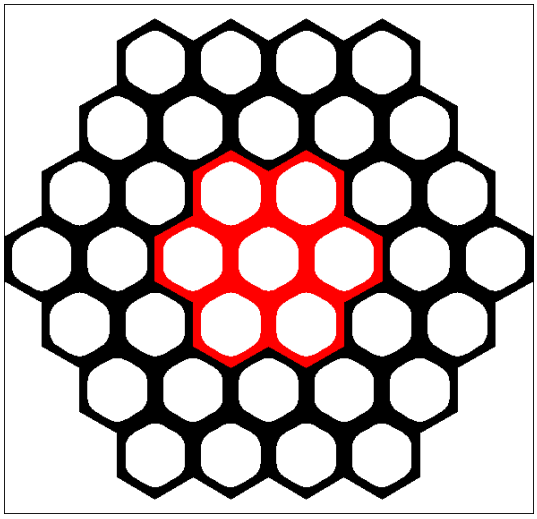

FIGURE 4.11: Periodic arrangement of unit cells, if the periodic structure is terminated at the edge of the unit cells around the core (i.e. red unit cells are removed to create the core), then the thickness of the glass left at the core boundary is just half the thickness of the struts in the cladding.

4.4.1.1 Transmission bandwidth *vs* ring thickness

In order to measure the useful transmission bandwidth of the different fibre designs, it was noticed that (*F-factor* $\cdot$ Λ) of the fundamental mode of a fibre with $T \leq 0.5$ is approximately equal to unity in the vicinity of the short wavelength edge of the bandgap ($\lambda \approx 1.88$ μm), see Figure 4.9(b) and Figure 4.10. Furthermore it remains less than one across most of the bandgap when there are no surface modes present. Therefore a threshold of $F\Lambda < 1$ is set to be the condition for measuring the useful bandwidth of the fibres and the operational bandwidth is defined as the maximum continuous wavelength range for which this condition is satisfied within the bandgap. Using this definition the operational bandwidth as function of the normalized core ring thickness is shown in Figure 4.12. In Figure 4.12(a) the operational bandwidth has been normalized with respect to the central bandgap wavelength $\lambda_c = 2.05$ μm while in Figure 4.12(b) the results are normalized with respect to the bandgap width measured at the airline, equal to 330 nm. As expected, hollow-core PBGFs with core walls of thickness in the range $0.45 \leq T \leq 0.65$ are optimal for broadband transmission providing a wide operational bandwidth of more than 15% of the central bandgap wavelength. Figure 4.12(b) shows that fibres in this new design regime have an operational bandwidth of over 90% of the bandgap width at the airline. The maximum operational bandwidth is 17% of λ_c (105% of the bandgap width at the airline) for a fibre with a core ring of $T = 0.575$. This new design regime drastically reduces the impact of surface modes as compared with a more conventional core design of $T = 1$ which has an operational bandwidth of only 9% of λ_c.

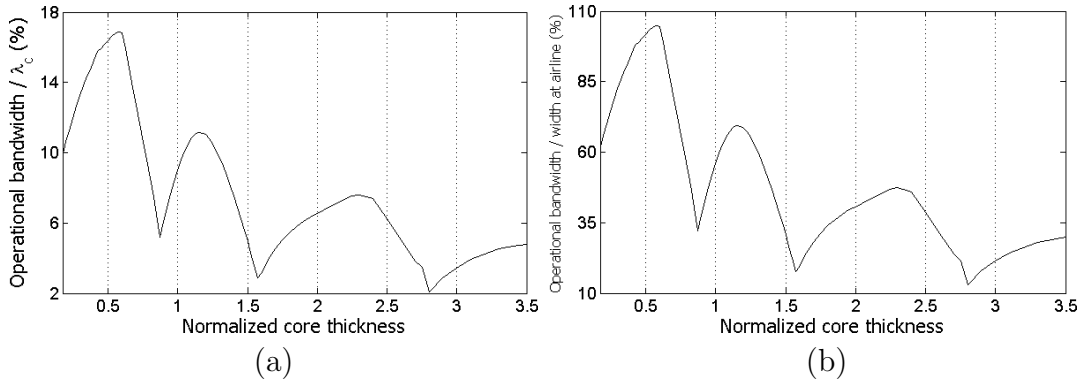

FIGURE 4.12: (a) Operational bandwidth normalized with respect to the central bandgap wavelength $\lambda_c = 2.05$ μm, and (b) normalized with respect to the bandgap width measured at the airline, equal to 330 nm.

It is important to mention that fibres with a thickness of the silica ring close to the optimum value, $T \approx 0.5$, are indeed feasible and can be realized simply by removing the 7 central capillaries from the stacked preform without the need to add an extra element to create the core.

4.4.1.2 Mode confinement and loss *vs* ring thickness

The two design maps in Figure 4.8 have been summarized in the plot of Figure 4.13 as follows: for each different core surround thickness (T) the minimum $F\Lambda$ value and maximum percentage of power in the core across all wavelengths within the bandgap are plotted against the ring thickness. Three design regimes where the confinement of the fundamental mode and the *F-factor* are maximized and minimized respectively have been identified. These correspond to the thin ring region centred around $T = 0.5$, an intermediate region around $T = 1.15$ and the antiresonant region, studied in detail by Roberts *et al.* [80, 78], around $T = 2.5$. Note that for this particular fibre design ($E = 100\%$), antiresonant core surrounds are not particularly noticeable and do not offer advantages over thin core surrounds. However, for other fibre designs it offers the possibility of reducing the scattering loss - see Section 4.4.2, chapter 5 and references [80, 78]. Of these three regimes which one is best depends on the applications of the fibre, however the new thin core design regime offers in all cases the widest operational bandwidth and should thus be preferred when fabricating fibres for broadband operation. Also for this particular core size thin core ring designs (T around 0.5) do present the lowest scattering loss (*F-factor*) in the bandwidth and are thus the preferred targets for fabrication.

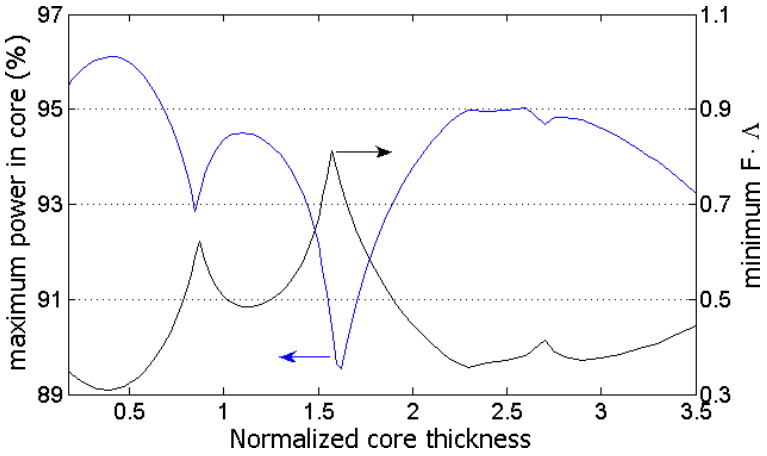

FIGURE 4.13: (blue) Maximum of the core-confined energy and (black) minimum F factor of the fundamental core mode *vs*. normalized ring thickness.

4.4.1.3 GVD and GVD-slope *vs* ring thickness

As previously mentioned, the group velocity dispersion (GVD) in hollow-core photonic bandgap fibres always goes from normal to anomalous within the transmission band, increasing near the bandgap edges and in the vicinity of a surface mode crossing. Therefore at the centre of the transmission band, fibres with wide transmission bands exhibit lower GVD and GVD-slope than fibres with narrow bands (i.e. fibres that support surface modes). This can be seen from Figure 4.14 that shows the calculated group velocity dispersion for the thin core wall fibre with a wide transmission spectrum ($T = 0.5$) and for a fibre with a reduced transmission band due to a surface mode crossing ($T = 1$). The dispersion curve for both fibres crosses zero on the short wavelength side of the bandgap. However, the fibre with $T = 0.5$ presents a much flatter dispersion curve indicating a lower GVD-slope than the thicker core ring fibre. The minimum GVD-slope across the low loss transmission region for each fibre design has been calculated and is plotted as a function of T in Figure 4.15. The trend of this curve closely follows the useful bandwidth *vs* T curve shown in Figure 4.12 - minima of the GVD-slope are found each time the operational bandwidth peaks and the GVD-slope presents a peak each time the bandwidth is minimized. The minimum GVD-slope for the fibre with $T = 0.5$ is equal to 1.391 ps/nm^2/km which represent a factor of five reduction compared to a more conventional design with $T = 1$. Due to their low GVD-slope these new thin core wall designs are convenient for soliton compression of high-power ultrashort pulses since the high order dispersion of previous hollow-core PBGFs has been a profound limitation on their performance in that important application [67, 66, 116].

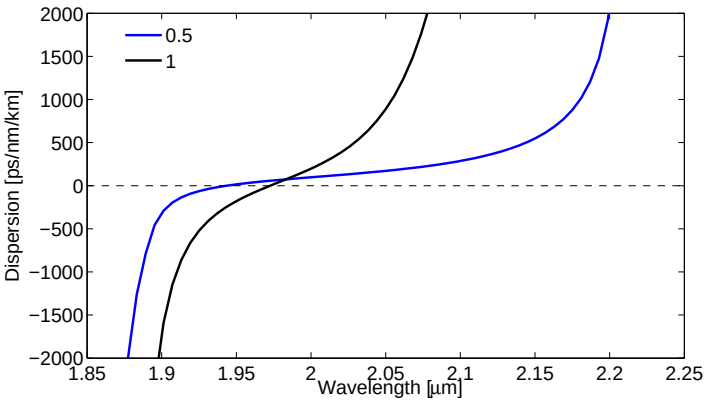

FIGURE 4.14: Calculated group velocity dispersion for fibres with $T = 0.5$ and $T = 1$.

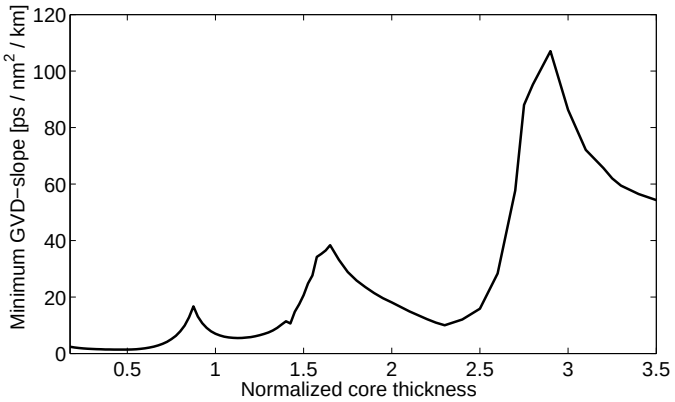

FIGURE 4.15: Minimum GVD-slope value within the bandgap for the different fibres, plotted against the normalized core ring thickenss (T).

4.4.2 Impact of variations in the size of the core on the guidance

After having identified designs that eliminate surface modes from the bandgap region, it is important to study fibres with expanded or compressed cores to check if they still present a wide transmission spectrum or if changes in the core size introduce new surface modes into the bandgap. Furthermore, fibres with a larger core should better confine the fundamental core mode and therefore should present lower loss than the fibres studied in the previous section. In order to understand the effects that compressing or expanding the core have on the fibre's transmission properties, the core has been modified by scanning the expansion coefficient E from 94% to 106% in 1.5% intervals. For each core radius the thickness of the core boundary (T) was varied in the same range as before and the *F-factor* and percentage of power in the core for the fundamental core mode were calculated. Contour maps of the percentage of power in the core of the fundamental air-guided mode as a function of E are shown in Figure 4.16. As the core is enlarged,

the fundamental core mode becomes more tightly confined in the central air region (red regions of the contour maps become darker as E increases) and therefore these designs should present lower scattering loss. Figure. 4.16 clearly shows that the transmission properties (number and position of surface modes) in fibres with thick core surrounds ($T > 2$) are strongly dependent on the size of the core. Conversely, surface modes supported by fibres with thin core surrounds ($T < 0.6$) are almost independent on the core size, therefore these fibres should be more robust against structural perturbations in fabricated fibres. This behaviour is more evident when comparing the contour maps for the fibres with the smallest ($E = 94\%$) and largest ($E = 106\%$) core analyzed, shown in Figure 4.17(a)(b) respectively - which show that the lower parts of the maps remain almost unchanged while the upper parts present major differences. Independently on the size of the core all thin core wall fibres ($T \approx 0.5$) are free from surface modes crossing on the high frequency edge of the bandgap, relaxing the precise control of variations on the core size along the fibre length. However, for too expanded cores ($E = 106\%$) one surface mode starts moving into the bandgap on the low frequency edge, reducing the fibre's transmission spectrum.

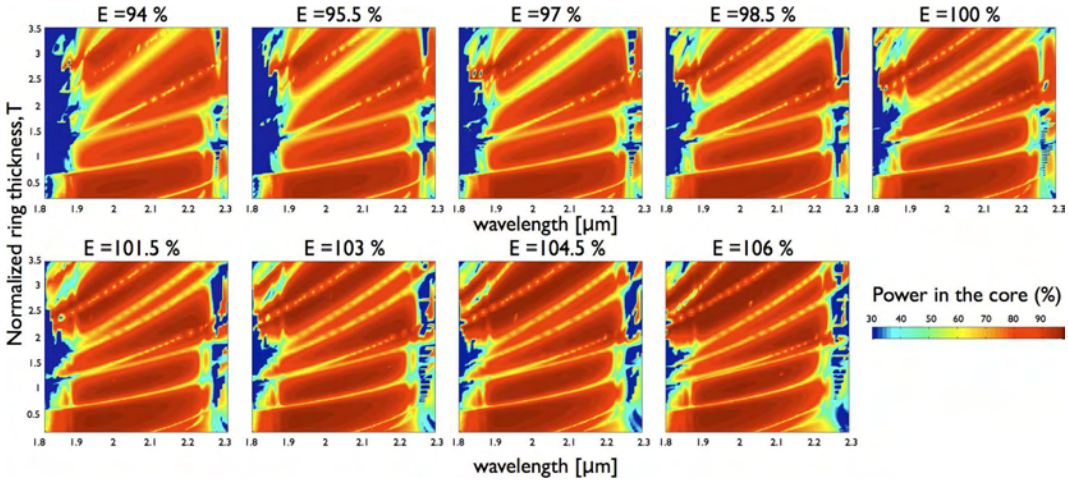

FIGURE 4.16: Contour maps of the percentage of power in the core of the fundamental air-guided mode for fibres with different core size (i.e. expansion coefficient E).

The maximum fraction of core confined energy, minimum $F\Lambda$ and useful bandwidth of fibres with different core radius are presented as a function of the normalized ring thickness in Figure 4.18(a),(b) and (c) respectively. Importantly, these changes in the core radius do not drastically shift the position of the three design regimes that maximize the mode confinement and minimize F that were found for $E = 0$. These plots also show that antiresonant core surrounds (T around 2.5) significantly assist the photonic cladding in confining core modes only for large core fibres and thus become important

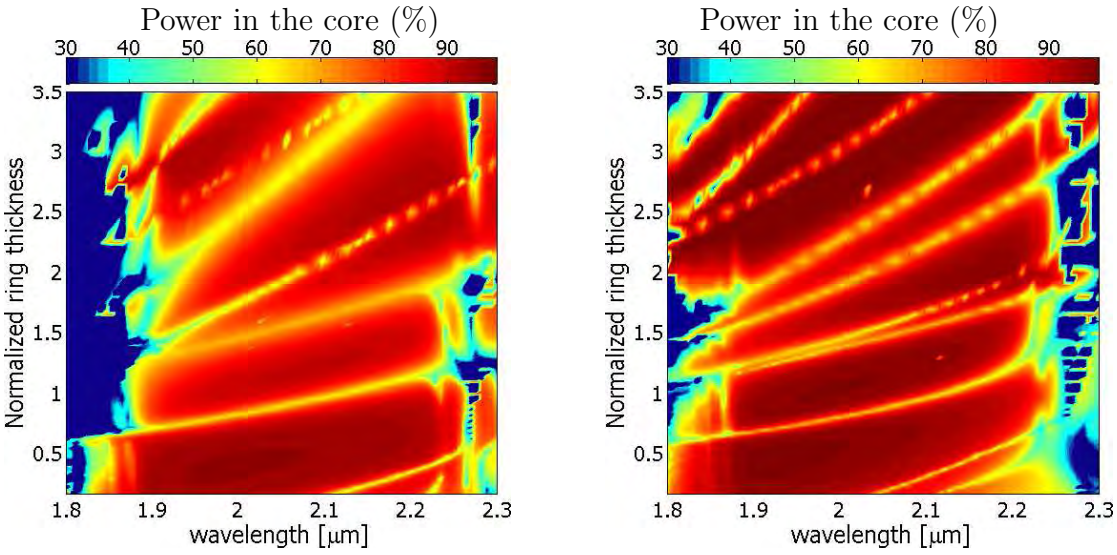

FIGURE 4.17: Contour maps of fraction of power in the core of the fundamental air-guided mode for fibres with the (a) smallest $E = 94\%$ and (b) largest $E = 106\%$ core analyzed.

for $E \geq 103\%$. Despite the presence of surface modes, fibres with large cores and antiresonant core surrounds are expected to present the lowest loss although only over very narrow spectral windows are seen in Figure 4.18(a)(c). Moreover, for these fibres the minimum achievable value of *F-factor* strongly depends in the exact core size. In contrast, the transmission properties of fibres with thin core surrounds (T around 0.5) are robust against variation in the size of the hollow-core. Therefore, unintentional changes of the core size during fabrication should not drastically affect their guidance. This is important as it is difficult to precisely control the size of the core of fabricated fibres. The inset in Figure 4.18(c) shows that variations in E produce rather small variations in the useful bandwidth of fibres in the thin core ring design regime. Finally, for all the core sizes studied, thin ring designs show superior performance than antiresonant core designs in terms of bandwidth and also present low loss. Indeed, for not too expanded cores (i.e. $E < 103\%$) thin ring designs present lower F values than designs with antiresonant core surrounds.

4.5 Conclusions

Through numerical computations it has been demonstrated that when defining the core of a HC-PBGF, the thickness of the core wall is a critical design parameter since it has a great influence on the density and frequency of surface modes which appear in the bandgap. Remarkably, it has been shown that by carefully selecting the thickness of the

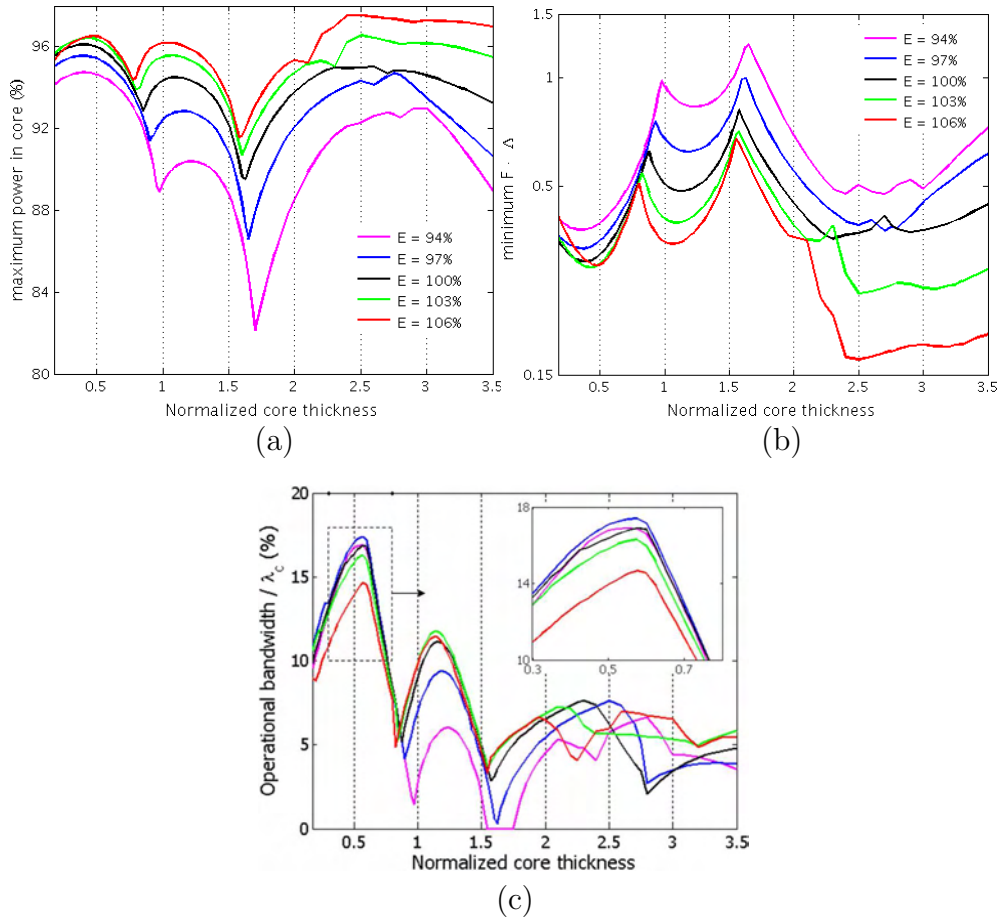

FIGURE 4.18: (a) Maximum of the core-confined energy, (b) minimum $F\Lambda$, and (c) operational bandwidth normalized with respect to the centre of the bandgap $\lambda_c = 2.05$ μm *vs.* normalized core thickness for $E = \pm 6.33\%, \pm 3.16\%$ and 0.

core wall and the size of the core, it is possible to design realistic high air filling fraction HC-PBGFs whose fundamental air-guided mode is free from anticrossings with surface modes at all wavelengths within the bandgap. The range of wavelengths that can be guided in a HC-PBGF is currently limited by the presence of surface modes and not by the width of the photonic bandgap formed in the cladding, therefore it is expected that the new fibre designs reported in this chapter will overcome this limitation.

This study found that in order to remove the impact of surface modes on the guidance, one needs to design and fabricate a fibre in which the cladding structure terminates as naturally as possible at the core-cladding interface. One way to do this is to simply form the core by terminating the cladding at the natural edge of a unit cell without the addition of extra glass. Therefore, it has been identified that fibres incorporating a silica core surround of just half the thickness of the thinnest features in the cladding, present the best transmission performance. It is important to mention that although in this chapter only a particular cladding structure was considered, these results are more general and are valid for fibres with different cladding and core designs -see chapter 5.

It has been shown that thin core wall designs ($T \approx 0.5$) offer the widest operational bandwidth and simultaneously reduce the overlap of the optical mode with the core wall. Thin core wall designs should thus be preferred when fabricating fibres for applications where broadband, low dispersion, and reduced higher order dispersion are required. Due to the absence of surface modes, this new fibre design broadens the range of wavelengths which can be transmitted in a hollow-core PBGF compare to previous designs. Also as a result of the increased bandwidth the dispersion and dispersion slope is reduced. It has been calculated that the GVD-slope can be reduced by a factor of five compared to previously studied fibre structures. Due to their superior performance, it can be anticipated that realizing these design could find applications in important areas of fibre laser technology since the high third order dispersion of previously available hollow-core PBGFs has been a profound limitation on their performance for soliton compression of high-power ultrashort pulses.

Furthermore, it was demonstrated that these new hollow-core PBGF designs are robust in eliminating surface modes and variations in the size of the core do not drastically affect their transmission performance, which eases the tolerances required for their fabrication. Although, only fibres operating at 2 μm were studied here, these results can be transposed to other wavelengths by simply scaling the structures.

Finally, these structures seem to be feasible targets for fabrication. It should be possible to fabricate them since they strongly resemble the fibres previously fabricated at our facilities. Indeed, the optimum thickness of the core surround ($T \approx 0.5$) can be obtained simply by removing the 7 central capillaries from the stacked preform without using an extra element to create the core. It is expected that extension of these designs to fibres with different core shapes promises a new range of hollow-core fibres free of surface modes with improved performance compared to those previously reported.

The next chapter extends the study presented here to bres featuring a larger core (19 cell) and a wider airguiding bandgap.

Chapter 5

Advanced designs of HC-PBGFs for low-loss, broadband and dispersion controlled operation

In the previous chapter it has been shown that by properly designing the core surround of HC-PBGFs featuring a 7 cell core and a moderately high airfilling fraction in the cladding, unwanted surface modes can be completely removed from the bandgap. In the following sections the modal properties of feasible hollow-core photonic bandgap fibres with cores formed by omitting either 7 or 19 central unit-cells and a wider air-guiding bandgap - cladding with a very high airfilling fraction of 94.2%, are studied. Firstly, fibres with thin core surrounds are analyzed and it is demonstrated that even for large cores sizes these core structures are optimum for broad-band transmission. The performance of these novel structures is compared with fibres which incorporate antiresonant core surrounds which repel the optical field from the core/cladding interface and therefore have low-loss. Trade-offs between loss and useful bandwidth are presented.

Finally, the effects that small modifications to the core surround have on the fibre's group velocity dispersion are analyzed numerically. This analysis shows that it is possible to control the group velocity dispersion of HC-PBGFs by slightly modifying the properties of the glass ring surrounding the core without incurring large loss penalties.

5.1 Introduction

As it has been previously discussed, the fundamental limiting factor for loss in hollow-core PBGFs is light scattering from surface capillary waves frozen during the fibre drawing process [79]. Thus if low-loss fibres are to be fabricated, mechanisms to reduce the light intensity at the silica interfaces must be investigated. Roberts and Mangan *et al.* showed that silica core surrounds whose thickness satisfies an antiresonant condition, repel the optical field at the core/cladding interface producing low-loss fibres [80, 15], antiresonant core surrounds which incorporate elliptical features have also been proposed [125]. However, the main drawback of these designs is that the reduction of loss comes with an increase in the number of undesirable surface modes. These surface modes exist at the same wavelength range as the core-guided air mode, but have far higher dispersion due to their large overlap with the glass. They interact with the air mode across some discrete spectral ranges, greatly increasing the attenuation and dispersion of the air mode and reducing the useable bandwidth of the fibre [76].

In chapter 4, moderately high air-filling fraction HC-PBGFs whose core is formed by omitting the 7 central unit cells were numerically studied, and it was found that in order to remove surface modes, one needs to design and fabricate fibres in which the cladding structure terminates as naturally as possible at the core/cladding interface. Therefore, feasible core surrounds that maximize the wavelength range over which the air-guided mode is free from anticrossings with surface modes should incorporate thin silica walls surrounding the core, in these structures the width of the core wall is around half the thickness of the thin silica struts of the cladding. Furthermore, it was shown that these fibre designs also offer low loss [121]. The need of designing feasible fibres with large cores and free from surface modes comes from the fact that enlarging the core is a straightforward way of reducing the overlap of the optical field with the glass structure and therefore the scattering loss, nonlinear response and GVD. Within this chapter, the study presented in chapter 4 is extended to examine 19-cell core hollow-core fibres and it is shown that the design regime identified previously for 7-cell core fibres is also valid for larger core defects, leading to novel wide bandwidth low-loss fibres. Furthermore, the fibres studied in this chapter incorporate a cladding structure with a much larger airfilling fraction in the cladding. This cladding structure is based on an idealized representation of the cladding of the low-loss fibre fabricated by the group at Corning [75, 76], which presents a very large air-guiding photonic bandgap of almost 450 nm centred at a wavelength of 1550 nm, this value is close to the maximum bandgap that can be achieved with a triangular lattice, see chapter 3.

The transmission band of HC-PBGFs always presents wavelength ranges of normal and

anomalous dispersion, due to this and their nonlinear properties, there has been a growing interest in using HC-PBGFs for re-compressing pulses in chirped pulse amplification systems [42, 126, 127, 128]. In the second part of this chapter ways of modifying the dispersion of HC-PBGFs are discussed. It is shown that it is possible to control the fibre dispersion over a reasonable wavelength range without incurring a large loss penalty.

5.2 Design of wide bandwidth low-loss HC-PBGFs

Cross sections of the analyzed 7-cell and 19-cell core air-guiding photonic bandgap fibres are shown in Figure 5.1(a)(b) respectively. These structures are idealized representations of fibres that can be manufactured by the stack-and-draw method, omitting the central capillaries to create the core and are parametrized using the model presented in Figure 3.10. The cladding parameters have been chosen to match those of the low-loss fibres reported in [75] and studied in [76, 77, 120]: relative hole size $d/\Lambda = 0.98$, curvature at the corners $d_c = 0.44\Lambda$, and distance from hole centre to hole centre $\Lambda = 4.7$ μm. The cladding's air-filling fraction is 94.2%. The silica ring surrounding the hollow-core has a normalized thickness T defined in equation (4.2), with corners rounded using circles of diameter $d_p = 0.2\Lambda$.

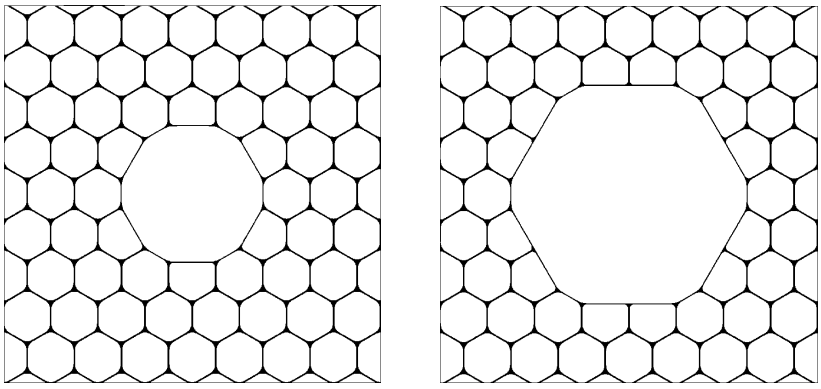

(a) (b)

FIGURE 5.1: Cross section of the analyzed hollow-core PBGFs: (a) 7-cell core, (b) 19-cell core. The structural parameters are: $d/\Lambda = 0.98$, $d_c/\Lambda = 0.44$, $d_p/\Lambda = 0.22$, $T = 1$, and $\Lambda = 4.7\mu$m.

For the 7 and 19-cells core fibres shown in Figure 5.1(a)(b), the thickness of the core surround was varied in the range $0.15 \leq T \leq 4.5$. Thicknesses at which the core surround becomes antiresonant can be approximated by considering it as an annular tube. In this case, antiresonance takes place for:

$$t_r = \frac{(2j+1)\lambda}{4\sqrt{n_s^2 - 1}}, \tag{5.1}$$

where λ is the wavelength, n_s is the glass index, and $j = 0, 1, 2, ...$ For the particular cladding studied here, antiresonance at wavelengths within the bandgap is achieved for T in the range 3 to 4.5. It is important to mention that the analysis of fibres incorporating antiresonant core surrounds is not the objective of this thesis and a complete study can be found elsewhere [80, 78, 125, 129, 130, 131]. The main objective of this chapter is to identify fibre designs with wide transmission spectra. Although broadband transmission cannot be achieved by using antiresonant core surrounds, these designs have been included in the calculations as a reference for low-loss fibres.

5.2.1 Transmission performance *vs* core design

For each T value the optical modes are numerically calculated for wavelengths within the bandgap and near the bandgap edges. Material dispersion is not considered, and the refractive index of silica and air are $n_s = 1.45$ and $n_a = 1$, respectively. Again as in chapter 4, this study only focuses on the modal properties of the fundamental air-guided mode (HE_{11}-like) and surface modes of compatible symmetry. Therefore, some higher-order modes are excluded and the computational time reduced by considering only one quarter of the fibre structure [108]. For the fundamental core mode, the power fraction in the core and the *F-factor* equation (3.3) as a function of wavelength are calculated. The transmission performance of the fibres as a function of the core shape will be evaluated by using these two parameters.

The calculated normalized interface field intensity of the fundamental air-guided mode for the various fibres is presented as a function of the normalized ring thickness and wavelength in Figure 5.2. The contour map in Figure 5.2(a) corresponds to fibres with a 7-cell core, while Figure 5.2(b) is for the large 19-cell core. In these maps, each horizontal line represents a different fibre design. The large values of the *F-factor* at wavelengths within the bandgap, diagonal yellow lines, are due to anticrossings between the fundamental air-guided mode and surface modes. At wavelengths near the anticrossing, the fundamental core mode couples to a particular surface mode and its overlap with the core surround increases and therefore the associated scattering loss also increases. Dark blue, eg. (*F-factor* Λ) ≤ 1, corresponds to regions where the fundamental air-guided mode is well confined in the air-core, has low overlap with the silica interfaces and therefore represents low-loss fibres. Finally, the rapid increases of the *F-factor* near 1350 nm and 1800 nm, correspond to the edges of the photonic bandgap.

From the maps in Figure 5.2 it is clear that the dependence of the transmission properties on T is very similar for both core sizes. However, as expected, 19-cell fibres achieve lower *F-factor* values (darker blue zones) and support more surface modes. Figure 5.2 clearly indicates that for both core sizes, fibres with core surrounds of normalized thickness

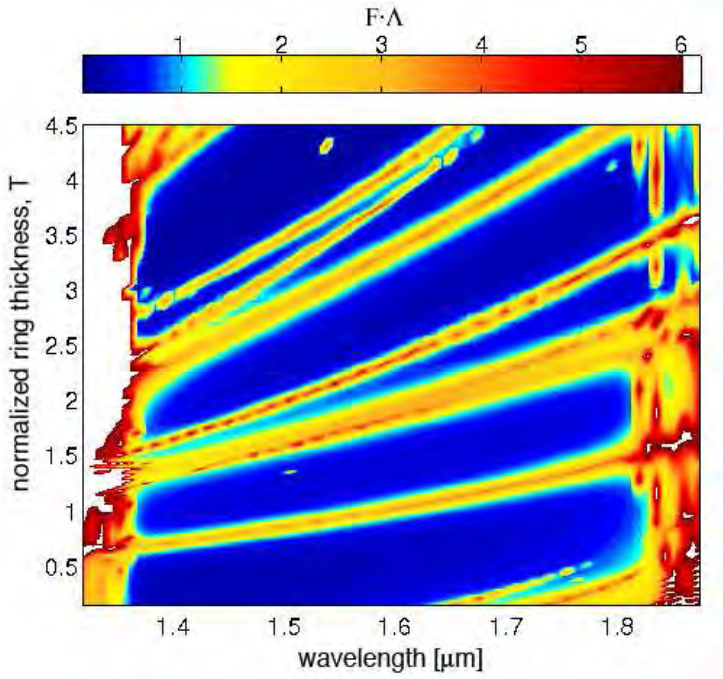

(a)

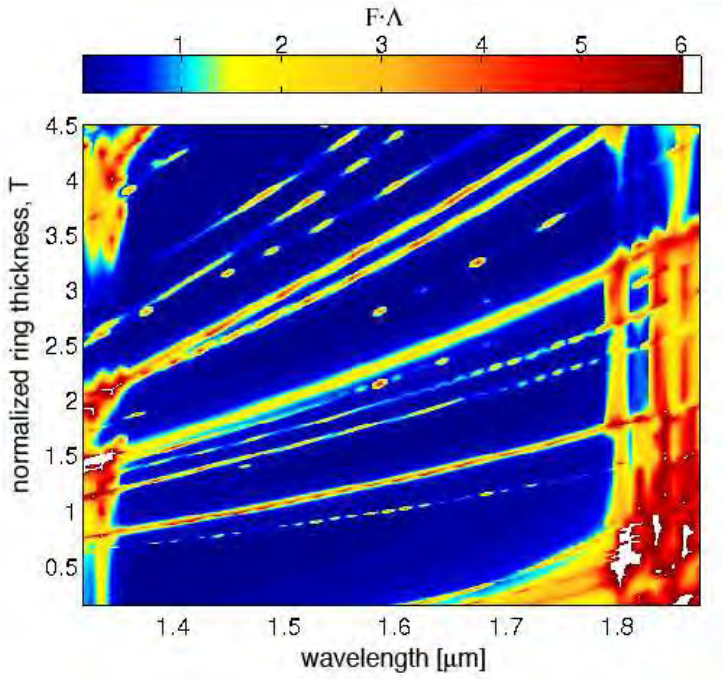

(b)

FIGURE 5.2: Normalized interface field intensity of the fundamental air-guided mode *vs*. wavelength for different values of the normalized ring thickness T. For the (a) 7-cell core fibre and (b) 19-cell core fibre. The colour scale is the same for both maps

$T \sim 0.5$ are almost free from surface modes anti-crossings and therefore maximize the wavelength range over which the light can be guided in the fibres, and at the same time provide a good confinement of the mode. These results show that thin core wall

designs should present a low-loss broadband transmission window independently of the core size. In contrast, fibres with any other thickness of the core wall support one or multiple surface modes and the useful bandwidth is reduced accordingly. Figure 5.2 also shows that fibres with thick antiresonant core surrounds, T in the range 3.5 - 4.5, present multiple surface modes and low attenuation transmission can only be achieved over narrow wavelength ranges.

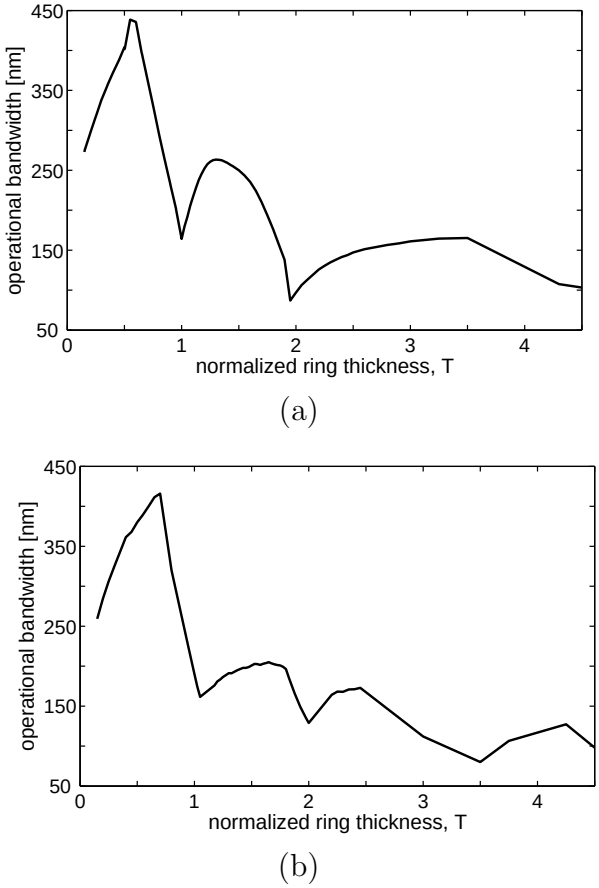

FIGURE 5.3: Calculated useful bandwidth *vs.* normalized ring thickness, (a) for the 7-cell core, and (b) 19-cell core fibres.

In order to obtain an estimation of the fibre's operational bandwidth, (*F-factor* $\Lambda < 1$) was set as the condition for maximum allowed "scattering loss" and the operational bandwidth is defined to be the maximum continuous wavelength range for which this condition is satisfied within the bandgap, see section 4.4.1.1. Using this definition, the calculated operational bandwidth as a function of T is shown in Figure 5.3(a)(b) for 7 and 19-cell core respectively. From these results it is possible to observe that for both core sizes, designs with core rings of thickness in the range of approximately $0.4 \leq T \leq 0.7$ are optimal for broadband transmission providing a wide low-loss usable bandwidth of more that 360 nm, which corresponds to $\sim 23\%$ of the central wavelength of the bandgap[2].

[2]For clarity, designs with core walls $T \approx 0.5$ are refereed to as thin core wall designs.

The low-loss wavelength range for fibres with $T = 0.5$ is 404 nm and 380 nm for 7 and 19-cell core respectively. This result is a clear indication that terminating the cladding at the natural edge of a unit cell ($T = 0.5$) induces a weak perturbation to the cladding structure and surface modes are only introduced near the long wavelength bandgap edge.

The main guidance properties of 7 and 19-cell core fibres with a thin core wall $T = 0.5$ are summarized in Figure 5.4. Figure 5.4(a,b,c,d) show the percentage of core confined energy, (*F-factor* Λ), effective mode area and the GVD of the fundamental core mode for both core sizes. From these plots it is clear that neither the 7-cell nor the 19-cell core fibre support surface modes on the high frequency edge of the bandgap. Although the peaks seen close to the low frequency bandgap edge are due to anti-crossings with surface modes, both fibres present a broad spectral range free from surface modes. Due to its larger core, as expected, the 19-cell core fibre presents lower (*F-factor* Λ), GVD and GVD-slope across the low-loss spectral range as compared to the 7-cell core.

After having identified fibre designs that provide wide band transmission, the performance of these fibres is compared in terms of loss and mode confinement against antiresonant designs. In order to do this, for each ring thickness the minimum *F-factor* value and maximum value of the power fraction in the air-core were obtained, and are plotted in Figure 5.5(a)(b) as a function of T for 7 and 19-cells core fibres respectively. These plots clearly point out that the minimum scattering loss (*F-factor*) is achieved by fibres incorporating antiresonant core surrounds. However the thicker silica core wall has led to more surface modes and the reduced loss come at the price of a reduced operational bandwidth. In contrast, thin core wall designs present somewhat higher loss but drastically improve the bandwidth of operation - see Figure 5.3.

The minimum normalized interface field intensity value achieved by the 7-cell core fibre is (*F-factor* Λ) = 0.1, for a ring thickness $T = 3.8$. This value is about 2.6 times lower than for a fibre with $T = 0.5$. For the larger core fibre (19-cells) Figure 5.5(b), the antiresonant regime becomes more important and the lowest value of (*F-factor* Λ) = 0.02 is obtained for $T = 4.25$, which is 3.3 times lower than for a fibre with $T = 0.5$. Therefore, it is expected that fibres incorporating antiresonant core surrounds should present approximately 2 to 3 times lower loss than thin core wall designs but only over narrow spectral ranges. In contrast, thin core wall designs should present higher loss but light can be transmitted with low-loss over more than 400 nm.

Comparing the normalized interface field intensity of fibres with $T = 0.5$ of different core sizes it is found that that the *F-factor* is typically about 3.2 times lower for the 19-cell fibre than for the 7-cell core, implying that the loss will be reduced by a similar factor [79], leading to novel wide bandwidth low-loss fibres.

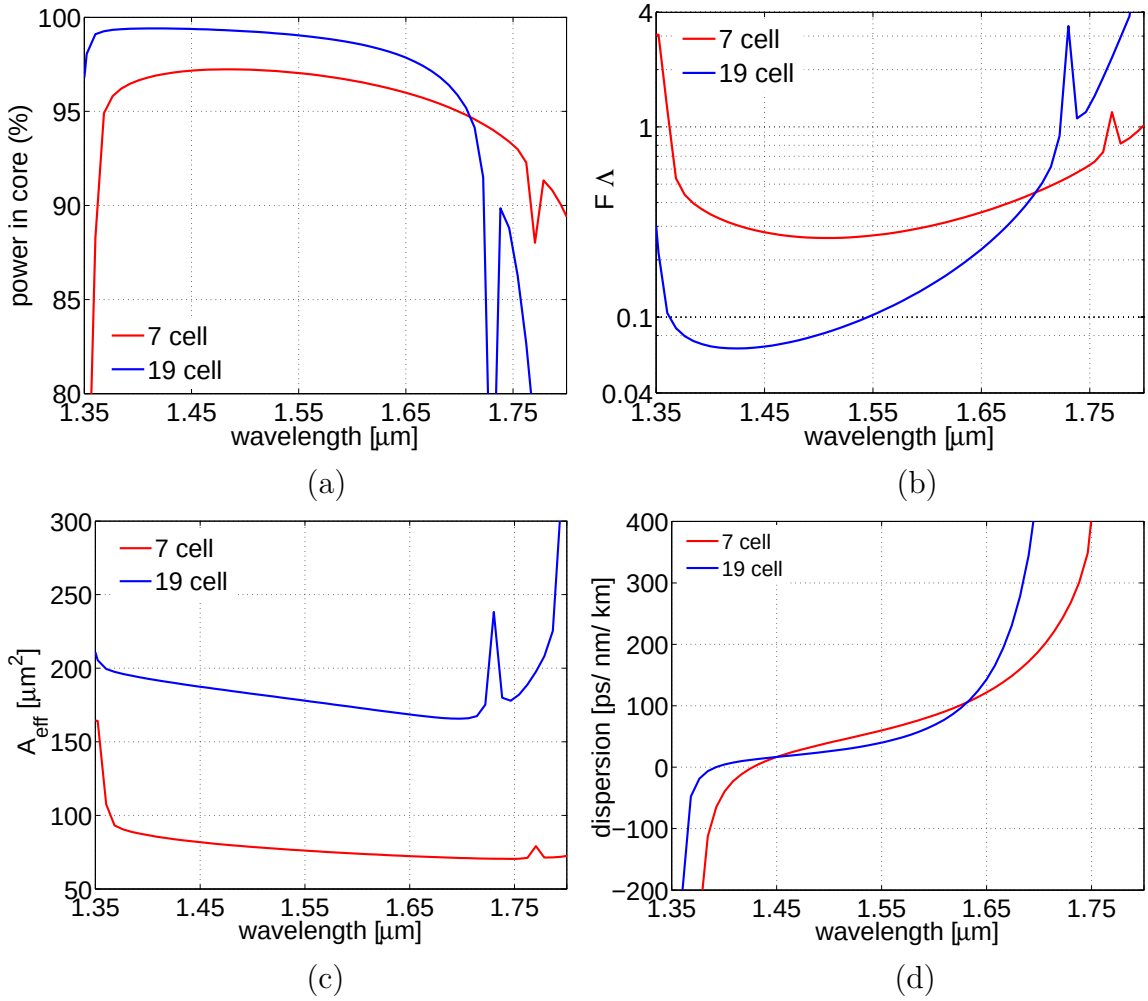

FIGURE 5.4: Main guidance properties of 7 and 19-cell core fibres with a thin core wall $T = 0.5$. Percentage of core confined energy, (*F-factor* Λ), effective mode area and the GVD of the fundamental core mode of both fibres in (a,b,c,d) respectively.

The minimum GVD-slope across the low-loss spectral range for each fibre design has been calculated and is plotted as a function of T in Figure 5.6 for the 7 and 19 cell core. As expected, due to their increased bandwidth, thin core wall designs minimize the GVD-slope of the fundamental mode.

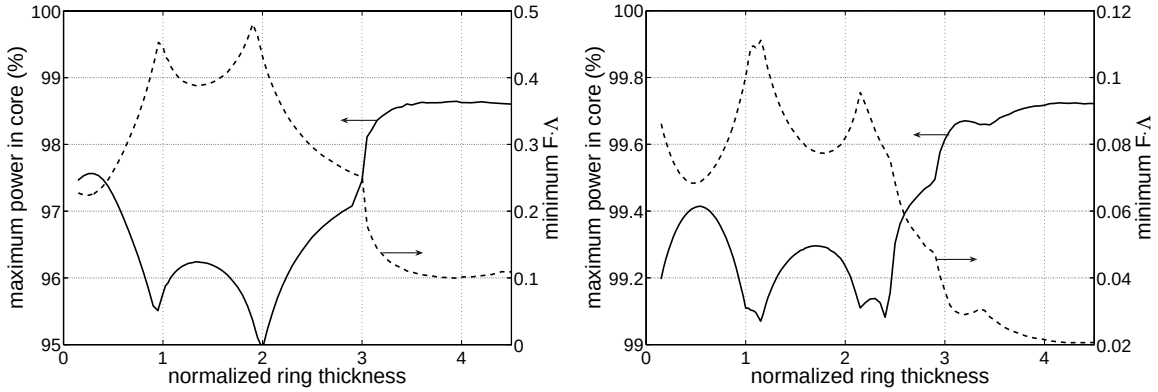

FIGURE 5.5: Maximum of the power fraction in the core (solid) and minimum of the normalized field intensity F (dashed) *vs.* normalized ring thickness, (a) for the 7-cell core, and (b) 19-cell core fibres.

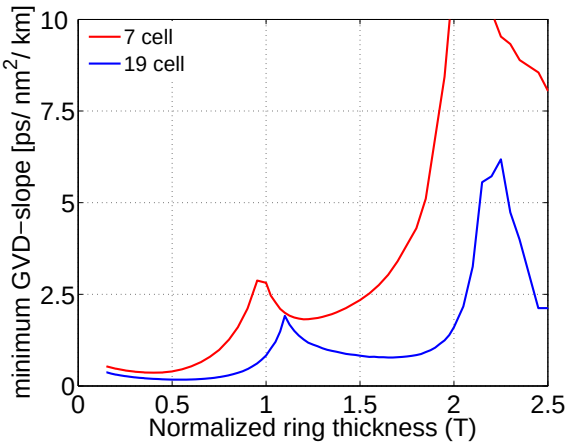

FIGURE 5.6: Minimum GVD-slope value across all wavelengths within the bandgap against the normalized core ring thickenss.

5.3 Tailoring the dispersion of hollow-core photonic bandgap fibres

5.3.1 Group velocity dispersion vs. ring thickness

In this section, a method of controlling the group velocity dispersion (GVD) in 7-cell core HC-PBGFs via small changes to the geometrical parameters of the core is presented. In this study only fibres with thin core surrounds are considered since these designs present low loss and support less surface modes and therefore should ease the precise control of the fibre properties during fabrication. In the mode calculations, material dispersion was considered and silica's refractive index was obtained from the Sellmeier equation (A.2).

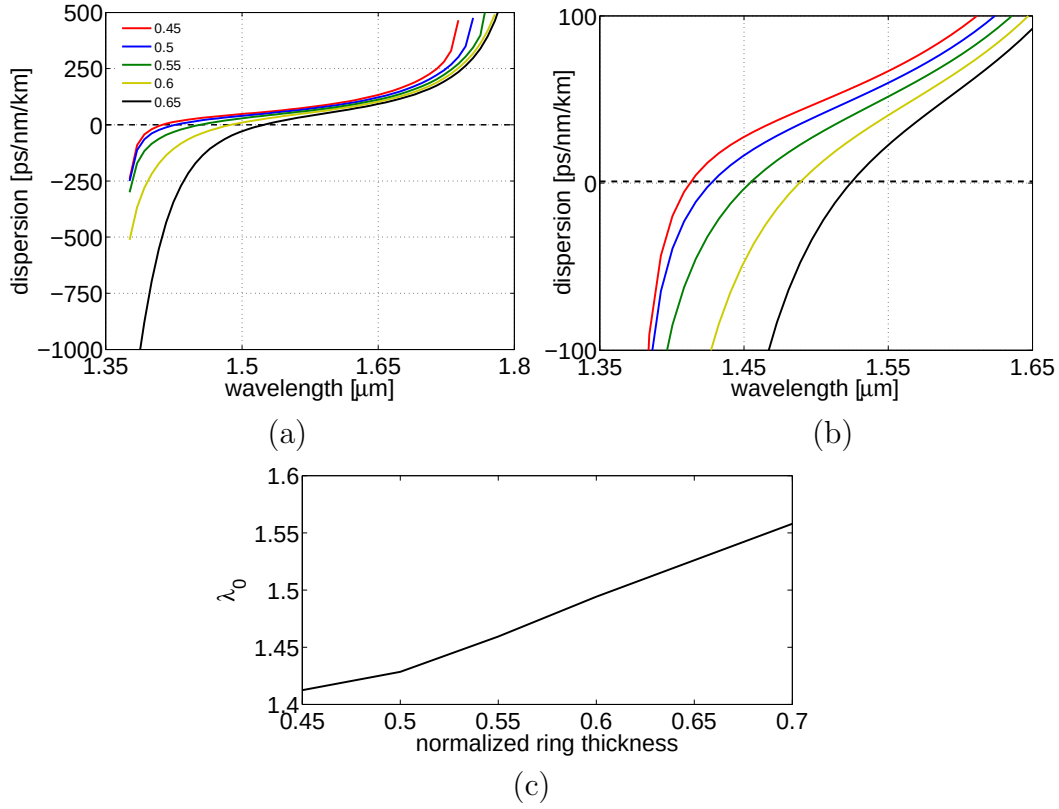

FIGURE 5.7: (a) Group velocity dispersion of the fundamental mode for a 7-cell core fibre with T = 0.45, 0.5, 0.55, 0.6, and 0.65. (b) Plot enlarged to show the zero-GVD wavelengths. (c) Zero-GVD wavelength as a function of the ring thickness.

Figure 5.7(a)(b) illustrates the calculated group velocity dispersion of the fundamental air-guided mode as a function of wavelength for the 7-cell core fibre for different thicknesses of the silica ring: T varying in the range 0.45 - 0.65. Although the changes to the core structure are rather small, tens of nanometres-scale, the effect on the GVD is quite noticeable. This is in good agreement with earlier reports of important changes in the fibre's nonlinearity [132] and birefringence [120] due to small alterations of the core boundary. Particularly interesting is that as the thickness of the core surround increases, the zero-GVD wavelength (λ_0) can be precisely shifted over ~100 nm wavelength range: λ_0 = 1.412 nm, 1.427 nm, 1.454 nm, 1.488 nm, and 1.523 nm for T = 0.45, 0.5, 0.55, 0.6, and 0.65 respectively. Moreover, as λ_0 is shifted towards longer wavelengths, larger normal dispersion values are obtained for wavelengths on the short wavelength side of λ_0. The origin of the change in the GVD can be attributed to the interaction of the fundamental air-guided mode and a surface mode that moves into the bandgap and anticrosses with the fundamental air-guided mode when the ring thickness is increased, Figure 5.2(a). This anticrossing can be easily recognized in the effective mode index against wavelength plot shown in Figure 5.8. Here, solid lines correspond to the fundamental air-guided mode, while dashed lines indicate surface modes that anticross with

the air-mode, and the shaded region represents the bandgap. The fibre with $T = 0.45$ (red), does not support surface modes guided near the short wavelength edge of the bandgap. In clear contrast, when $T = 0.65$ (black) one surface mode is guided near the short wavelength bandgap edge. This "new" surface mode and the core mode anticross and in the transition region the core mode rapidly changes it effective mode index - at around 1.38 μm the black curve presents larger dispersion than the red curve. This rapid change in refractive index produces strong GVD near the anticrossing wavelength and also the zero-GVD wavelength is shifted towards the centre of the bandgap Figure 5.7. It is important to mention that a similar shift in the anticrossing wavelength can be achieved by keeping the core wall thickness constant and slightly changing core size[3].

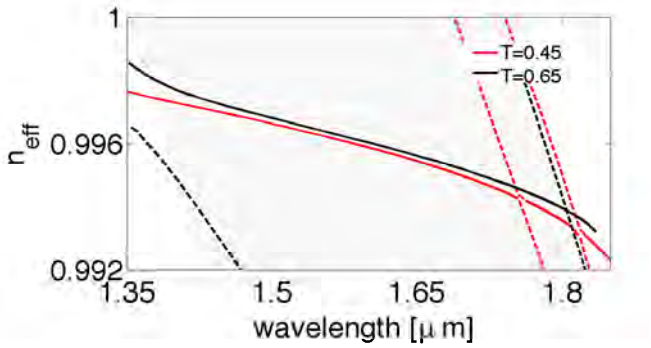

FIGURE 5.8: Calculated modal index *vs.* wavelength for $T = 0.45$ (red) and 0.65 (black). Solid lines correspond to the fundamental air-guided mode, while dashed lines correspond to surface modes.

As modifying the fibre's GVD properties involves controlling the position of surface modes within the bandgap, it is important to evaluate the increase in loss. Figure **??** shows the normalized interface field intensity of the fundamental air-guided mode against wavelength for different thicknesses of the core surround. Black circles indicate λ_0 for each fibre design. The normalized interface interface field intensity at the zero-GVD wavelength for the fibre of $T = 0.65$ is only 1.23 times larger than that for the design with $T = 0.45$. Implying that shifting λ_0 from 1.412 nm to 1.523 nm can be achieved at the expense of $\sim 23\%$ increase in loss [79]. Furthermore, the wavelength range over which the fibres have normal dispersion and the condition $F\Lambda < 1$ is satisfied has been calculated. The calculated low-loss, normal dispersion wavelength ranges are: 40 nm, 55 nm, 82 nm, 113 nm, and 111 nm for $T = 0.45$, 0.5, 0.55, 0.6, and 0.65 respectively. It is important to mention that the zero-GVD wavelength can be progressively shifted towards longer wavelengths as T is increased still further. However, this will imply an increase on the fibre loss and a reduction of the transmission bandwidth, [see Figure 5.5(a) and Figure 5.3(a)].

[3]Chapter 4 showed that by enlarging the core of an idealized 7 cell fibre, surface modes are introduced on the long wavelength bandgap edge while collapsed cores support surface modes on the short wavelength edge.

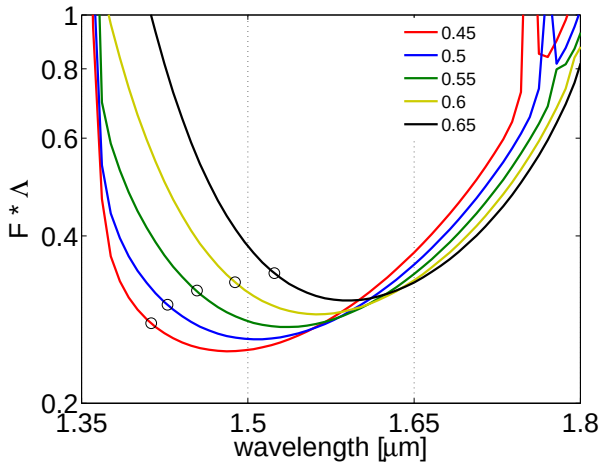

FIGURE 5.9: Normalized interface field intensity of the fundamental mode for a 7-cell core fibre with $T = 0.45$, 0.5, 0.55, 0.6, and 0.65. The black circles indicate the zero-GVD wavelength for each design.

5.3.2 Group velocity dispersion vs. refractive index of the core surround

An alternative way of modifying the fibre's transmission properties is by increasing or decreasing the refractive index of the glass region surrounding the core. It is reasonable to expect that by doing this, surface modes will be more affected than air-guided modes since these modes tightly confine energy in the core surround. Consequently, in this way it is possible to increase or decrease the effective mode index of surface modes and thus move their position inside the bandgap. In this section the effect that changes in the refractive index of the core surround have on the group velocity dispersion of HC-PBGs is studied. Figure 5.10(a) shows the cross section of the analyzed fibre: red represents the glass region for which we varied the refractive index, black corresponds to pure silica and white to air. A stack of capillaries that could be used to fabricate this kind of fibre is presented in Figure 5.10(b). For the following simulations we have calculated the refractive index of silica n_s using Sellmeier equation (A.2), and the refractive index of the silica ring (red region) is obtained by increasing the refractive index of silica as: $n_g = n_s(1+n_{increase})$.

For the 7-cell core fibre, while keeping the core thickness constant $T = 0.5$, the refractive index of the core surround is increased up to 5% in 1% intervals. Figure 5.11(a)(b) show the effect of this perturbation on the fibre's GVD. Similarly to the previous case, as the refractive index of the core surround increases, the zero-GVD wavelength is shifted towards long wavelengths. An increase in the refractive index of 5% produces a shift in λ_0 of 100 nm, from 1.427 nm to 1.527 nm. In addition, larger normal dispersion values are obtained for wavelengths on the short wavelength side of λ_0.

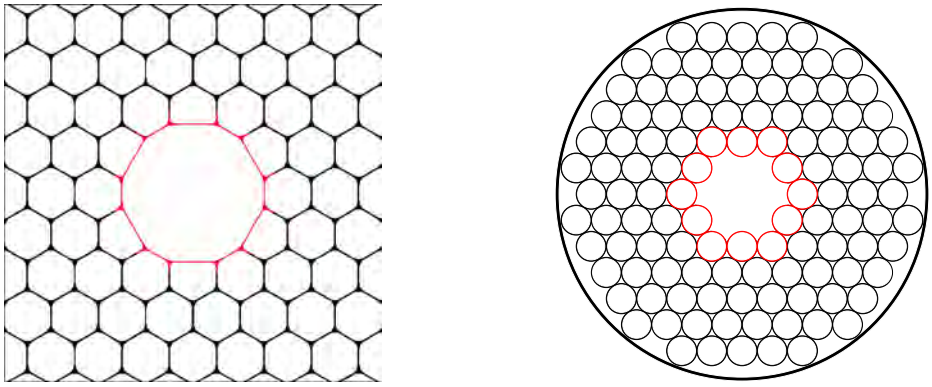

(a) (b)

FIGURE 5.10: (a) Schematic cross section of fibre with core surround of modified refractive index. (b) Stack of capillaries that can be used to fabricate the proposed fibre. Red represents glass of different refractive index, black is for silica and white air.

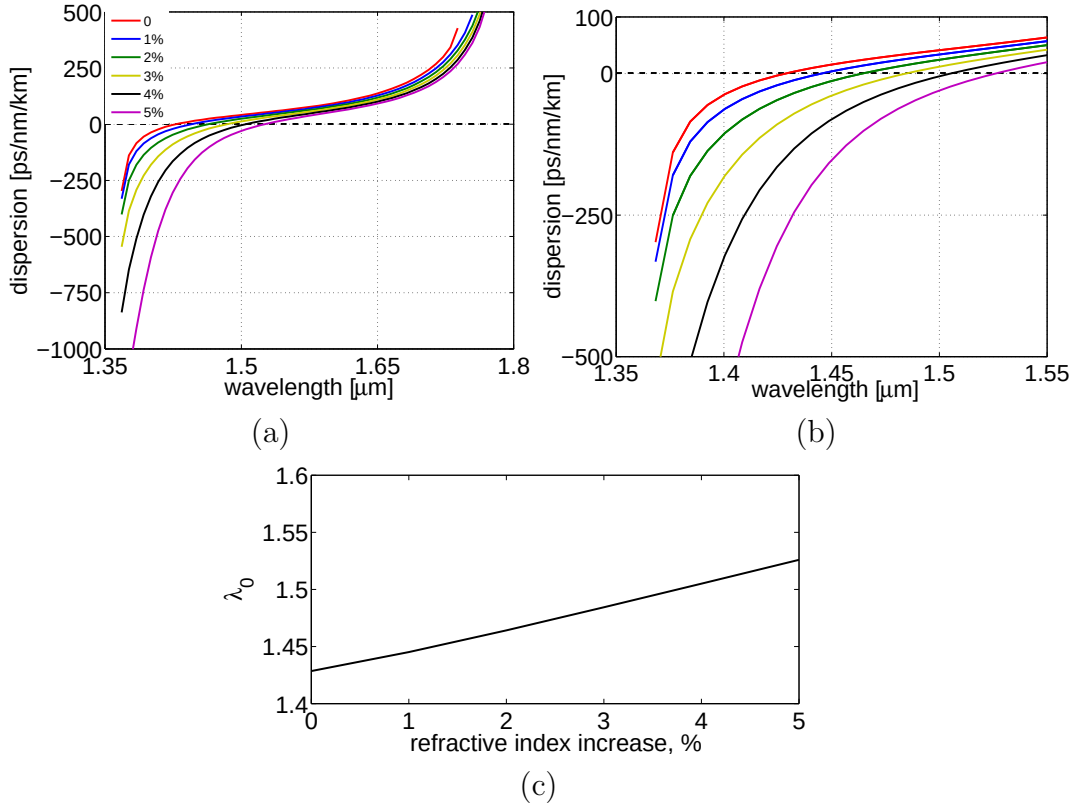

FIGURE 5.11: (a) Group velocity dispersion of the fundamental mode for a 7-cell core fibres with different refractive index of the core wall. (b) Plot enlarged to show the zero-GVD wavelengths. (c) Zero-GVD wavelength as a function of the change in the refractive index of the core surround.

Surprisingly, although the changes seen in the fibre's GVD [Figure 5.11(c)] are comparable to what can be achieved by increasing the thickness of the ring [Figure 5.7(c)], Figure 5.12 shows that in this case shifting the zero-GVD wavelength 100 nm can be achieved with less increase in loss. The normalized interface interface field intensity at

the zero-GVD wavelength when the refractive index of the core surround is increased by 5% is only 1.055 times larger than that for the original fibre, see black circles in Figure 5.12. This implies that a shift of 100 nm in λ_0 will only increase the loss at the fibre's zero-GVD by $\sim$ 5.5% [79]. A drawback of this method is that the increase in refractive index (5%) needed to achieve a shift in λ_0 of 100 nm, is quite big and might be difficult to fabricate. However, it has been showed that the use of doped elements in HC-PBGFs can be used to control the GVD properties without drastically affecting the loss.

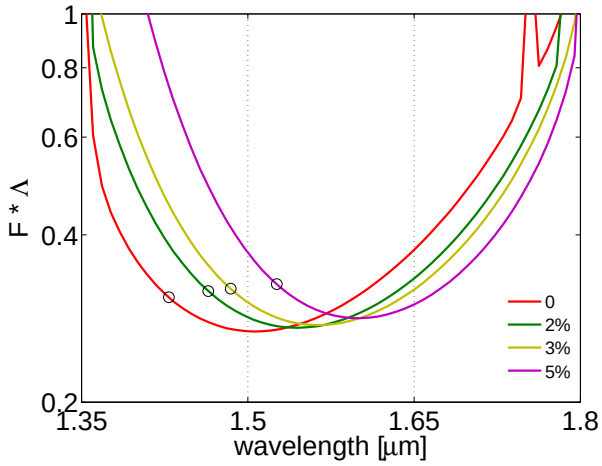

FIGURE 5.12: Normalized interface field intensity of the fundamental mode for a 7-cell core fibre with T = 0.45, 0.5, 0.55, 0.6, and 0.65. The black circles indicate the zero-GVD wavelength for each design.

Finally, the GVD in the thin core wall 19-cell fibre is similar to the GVD in the 7-cell fibre but with λ_0 shifted to even shorter wavelengths and a smaller value of anomalous dispersion in the middle of the bandgap, Figure 5.13. The strategies for tailoring the GVD presented here are applicable also to the 19-cell core case as seen in Figure 5.13 which plots the dependance of the GVD on the thickness of the core wall.

5.4 Conclusions

In chapter 4 it was demonstrated that 7-cell air-guiding PBGFs with a thin core wall are optimal for maximising the useable bandwidth while maintain low loss [121] by reducing the impact of surface modes. In this chapter the work done on 7-cell fibres has been extended to the case of larger core fibres 19-cell and showed that this design regime is robust and the principles developed for the 7-cell fibres apply here as well. In particular the bandwidth of operation of HC-PBGFs is maximized if the thickness of the silica ring surrounding the core is about half the thickness of the thin struts of the cladding independently if the core is formed by removing the central 7 or 19

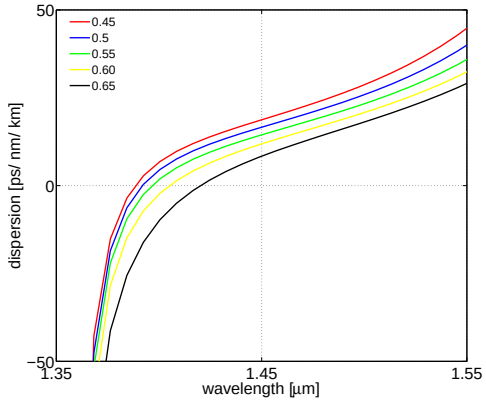

FIGURE 5.13: Group velocity dispersion of the fundamental mode for a 19-cell core fibre with $T = 0.45$, 0.5, 0.55, 0.6, and 0.65.

cells. For the cladding configuration analyzed here, the confining ability provided by fibres with antiresonant core surrounds is superior than thin core surrounds and should thus be preferred for applications requiring low-loss and low-nonlinearity over narrow wavelength ranges. However, for applications requiring relatively low-loss over a wide wavelength range, low dispersion, and low dispersion slope, a fibre featuring thin core walls and 19-cell core is to be preferred.

For core surrounds of normalized thickness $T = 0.5$, the 19-cell core fibre typically has ∼3.2 times lower loss than the 7-cell core fibre over a comparable bandwidth, leading to novel wide bandwidth low-loss fibres. Fabricating these designs would greatly extend the useable bandwidth of the fibres. The transmission spectra of previously-reported 19-cell fibres have been completely dominated by surface mode crossings, and it is anticipated the larger core size and greatly reduced dispersion slope in the new fibres would enable a new regime of ultrashort-pulse solitons and high-power beam delivery. Furthermore, since these designs are free of surface modes across a wide wavelength range, they should be more insensitive to fabrication errors.

Simulations presented here show that it is possible to control the fibre's group velocity dispersion by slightly modifying the properties of the glass ring around the core without incurring large loss penalties. Two strategies are analyzed: the first one consists of modifying the thickness of the core surround, and the second changing its refractive index. Particularly interesting is the possibility of shifting the zero dispersion wavelength over $\sim 25\%$ of the bandgap width. Although, the position of the zero dispersion wavelength can also be shifted by scaling the whole structure (moving the bandgap) the techniques studied here are important since there is no need of changing the outer diameter of the fibres. This should therefore facilitate the integration of HC-PBGFs to other fibre components in an optical system, [for example if a particular fibre outer diameter is required].

Chapter 6

Control of surface modes in low-loss hollow-core PBGFs

The work presented in this chapter has been carried out at the Centre for Photonics and Photonics Materials at the University of Bath in collaboration with Dr. Frédéric Gérôme, Dr. Sergio Leon Saval, Prof. Jonathan Knight and Prof. Tim Birks. The author would like to thank Steve Renshaw and Alan George for their help in the fabrication and assistance for this work. The fibres presented here are based on the numerical calculations presented in previous chapters which show that if the core walls have just half the thickness of the thinnest features of the cladding, then surface mode interference can be suppressed.

In the following sections the fabrication and characterization of hollow-core photonic bandgap fibres that do not suffer from surface mode coupling within the photonic bandgap of the cladding is presented. The elimination of surface modes enables low attenuation over the full spectral width of the bandgap - a minimum loss of 15 dB/km and less than 50 dB/km over 300 nm for a fibre operating at 1550 nm has been measured. Thanks to these developments it is for the first time possible to achieve core-confined guidance with low attenuation over the full bandgap of the photonic crystal cladding. As a result of the increased bandwidth, the fibre has reduced dispersion and dispersion slope - by a factor of almost 2 compared to previous fibres. These features are important for several applications in high-power ultrashort pulse compression and delivery. Realizing these advances has been possible due to development of a modified fabrication process which makes the production of low-loss hollow-core fibres both simpler and quicker than previously.

6.1 Fibre fabrication

HC-PBGFs with a core formed by the omission of seven unit cells which presents no sign of surface modes interactions within the bandgap have been fabricated. As a result of the absence of surface modes crossings, the fibres have wider bandwidth and approximately halved dispersion and dispersion slope compared to previous fibres. The fibre design is based on the numerical computations presented in chapter 4 and chapter 5 which show that if the core walls have just half the thickness of the thinnest features of the cladding, then surface mode interference can be suppressed [121, 122]. The hexagonal stack of capillaries represented schematically in Figure 6.1 shows that when the central 7 capillaries are removed and no extra elements are added to form the core, then the cladding terminates at the edges of complete unit cells and the thickness of the core wall is half the thickness of the cladding struts. Fabricating such a structure represents a challenge which has been overcome using a modified fabrication procedure that allows for the production of low-loss HC-PBGFs from scratch within a single day.

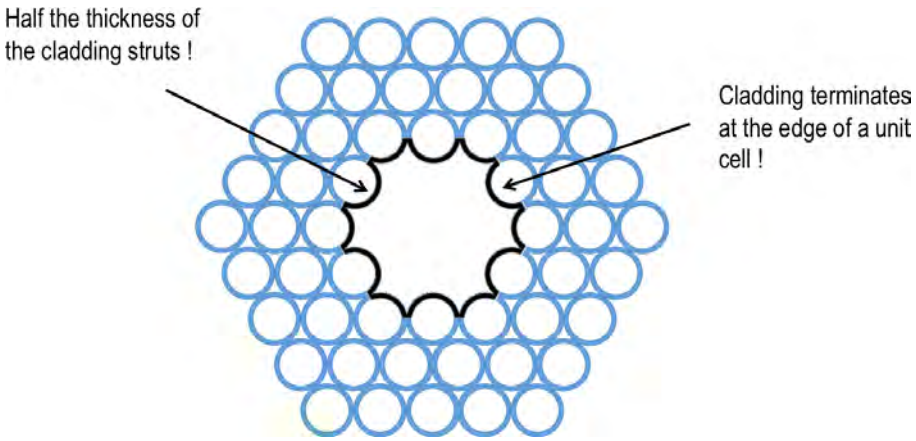

FIGURE 6.1: Hexagonal stack of capillaries where the central 7 capillaries are removed to form the central defect.

The fibres reported here were fabricated entirely from high-purity synthetic silica glass (F300 from Heraeus Quarzglas) using the stack-and-draw technique. Previous low-loss hollow-core fibres [79] were formed using a two-dimensional array of tubes stacked around a thin-walled core tube. The core tube replaced the several capillaries omitted during the stack, preventing the cladding capillaries from falling into the core. The cladding tubes fuse together and their bores become the cladding holes needed in the final fibre. In order to end up with the required cladding structure that presents wide bandgaps, the capillaries used need to be thin-walled. However, this means that there is not enough glass at the joint between three cladding tubes and additional solid rods (in the form of thin fibres) were inserted into the interstitial holes in the stack to create the

required array of strands of glass, joined and supported by thin silica webs in the final fibre [83] - see section 3.2.1.1 and Figure 6.2 which shows an example of a cladding unitcell that supports a wide bandgap. Then when drawing the stack down to canes (see section 2.2), the spaces between capillaries were evacuated and the relative scale of the whole structure was roughly preserved in drawing the preform down to a fibre.

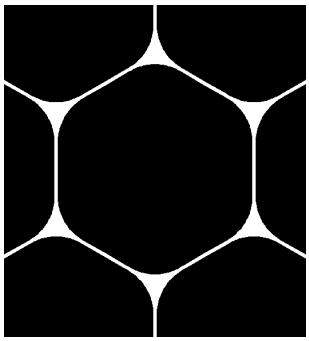

FIGURE 6.2: Example of a cladding unitcell required to form a bandgap. In the final fibre an array of glass nodes are joined and supported by thin silica webs.

In contrast, the fibres being reported here were drawn from a stack with neither core tube nor the addition of extra glass in the interstitials. Circular capillaries with thicker walls (relative to their diameters) than required in the final fibre were used to form a stack in which the core was created by simply omitting 7 central capillaries without using an extra tube. Short capillaries were used at both ends of the stack to support the core defect which is unsupported in the middle, as schematically shown in Figure 6.3.

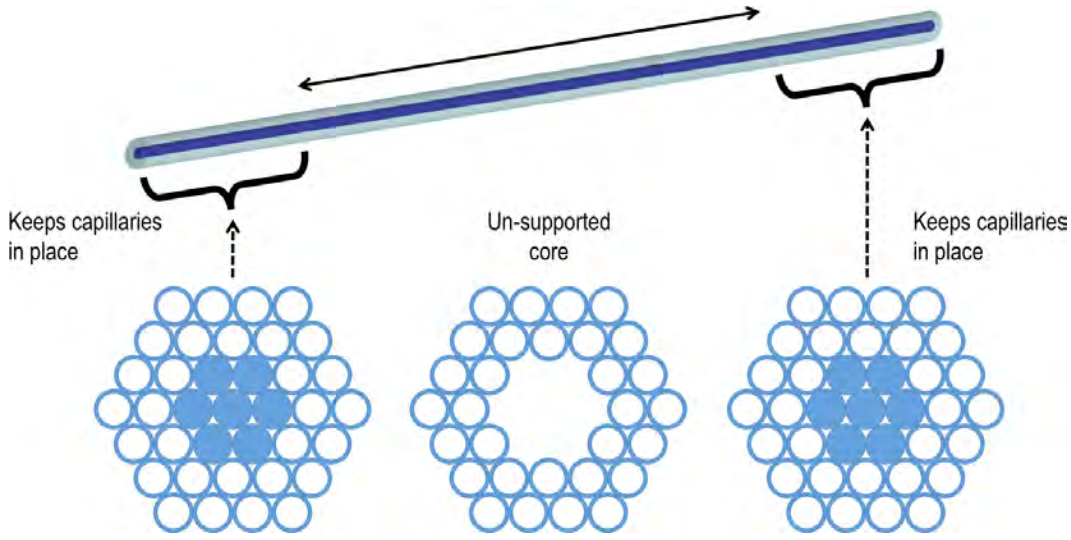

FIGURE 6.3: Schematic of a stack of capillaries in which the core is formed by simply omitting the 7 central capillaries and is supported at each end of the preform using much shorter capillaries, and is unsupported in the middle.

Omitting the core tube resulted in a core wall thickness just half that of the struts in the cladding, as required to suppress surface modes. The stack was drawn to fibre in two

drawing stages, with pressure applied at the top of the preform being used to inflate the structure to a high air fraction during the final draw. During drawing, inflation leaves bigger strands at the interstitial sites joined by thinner webs - without the need of filling the intertitials holes with thin rods. A typical SEM image of one of the canes before the final draw to fibre is shown in Figure 6.4. Comparing Figure 6.1 it is clearly seen that the deformation at the core boundary of the fabricated cane is small.

This process allows for easy and very rapid fabrication of fibres with a core wall thickness close to the thickness required to eliminate surface modes, and having both broadband operation and state-of-the-art attenuation. The simplicity of the process makes it possible to draw a hollow-core fibre from scratch, within a single day.

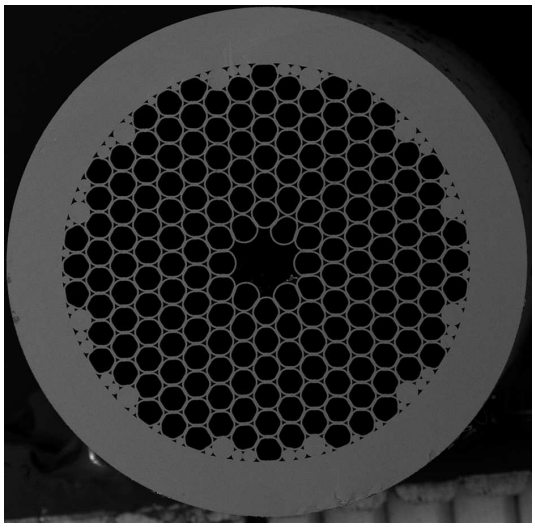

FIGURE 6.4: Typical SEM image of a cane used to draw the fibres. The outer diameter shown is 3.3 millimetres, and an addition silica jacket has yet to be added during the final draw to fibre.

6.2 HC-PBGF free from surface modes

An optical microscope image and a scanning electron microscopy (SEM) image of the fabricated thin core wall fibre are shown in Figure 6.5 (a)(b) respectively. The thin core wall fibre features a 7-cell core surrounded by 6 rings of cladding holes plus one incomplete ring to facilitate the stacking. Detailed structural analysis was performed by SEM which allowed verification that the thickness of the core wall was within the regime for eliminating surface mode resonances within the bandgap. The core geometry of the fibre is slightly different to the core designs previously studied in chapter 4 and chapter 5 and [121, 122], because during the fabrication process the fibre's core and the ring of holes immediately surrounding it have further been experimentally optimized in order to reduce loss and maximize the transmission bandwidth.

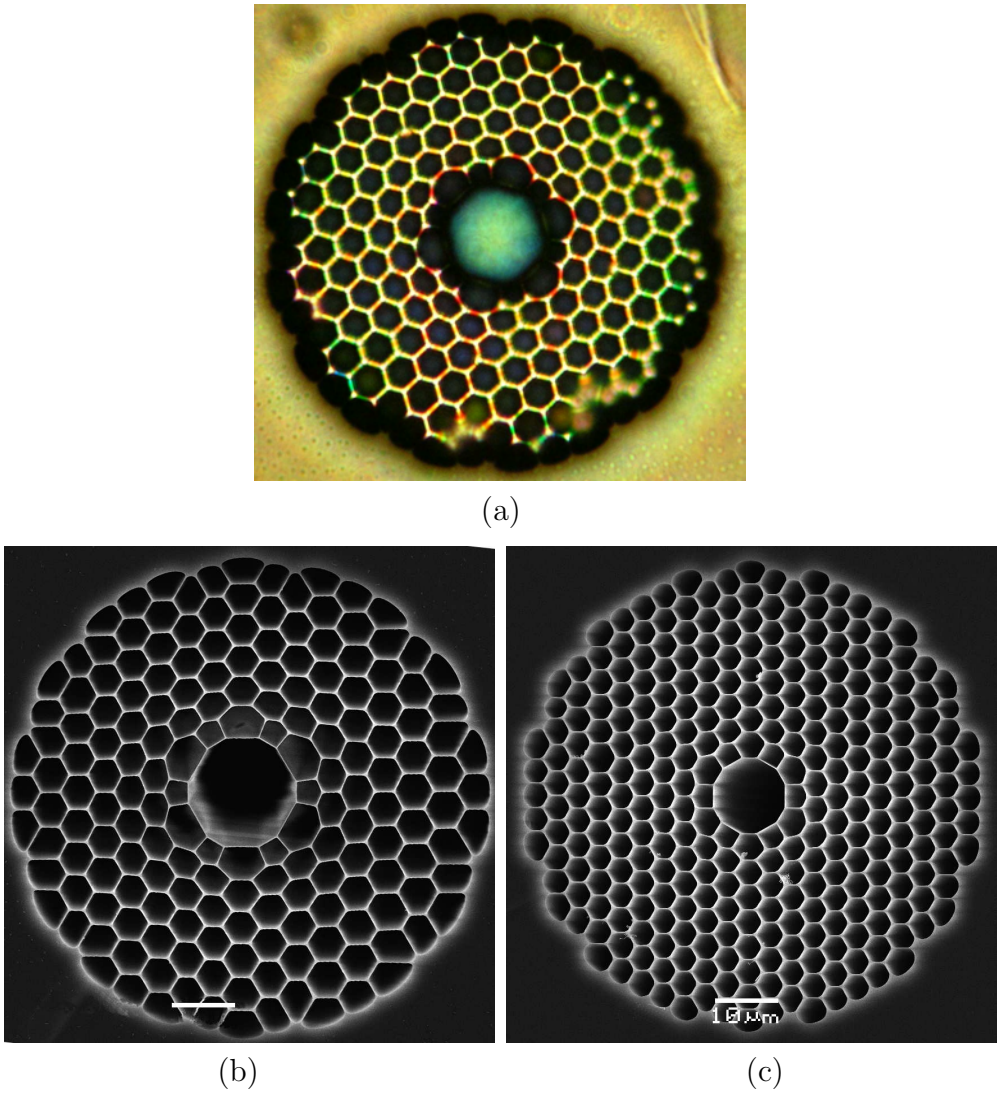

(a)

(b) (c)

FIGURE 6.5: (a) Optical microscope image of thin core wall 7-cell HC-PBGF. SEM micrographs of 7-cell HC-PBGF designed to operate at 1550 nm, to the same scale: (b) Fibre incorporating a thin core wall, and (c) conventional HC-PBGF similar to that available commercially. Scale bars correspond to 10 μm.

For comparison, Figure 6.5(b) shows an SEM image of a fibre similar to those commercially available and designed for 1550 nm transmission - in what follows it will be referred to as "old fibre". Note that although the size of the microstructured region is almost the same for the two fibres, the thin core wall fibre has two fewer rings of cladding holes than the old fibre.

The photonic crystal cladding of the thin core wall fibre has a pitch $\Lambda = 5.2$ μm and an air filling fraction of $\sim 96\%$ that give rise to a photonic bandgap centred approximately at 1550 nm. The high air-filling fraction in the cladding enables the formation of a wide photonic bandgap crossing the airline, which covers around 22% of the central bandgap wavelength. The cladding pitch of previously-reported HC-PBGFs designed

for transmission at 1550 nm has typically been between 4 μm to 4.8 μm [75, 79, 15]. Due to its large pitch, the thin core fibre features a larger core than previous designs (see Figure 6.5), which in general can be expected to result in reduced interaction of the air-guided mode with the core-cladding interface, reduced effect of waveguide dispersion and lower nonlinear response. The core diameter of the thin core wall fibre is ≈ 16.3 μm in contrast to ≈ 10.9 μm for the old fibre.

6.2.1 Attenuation spectrum

The optical attenuation of the thin core wall 7-cell HC-PBGF was measured using the cut-back technique. A sample of 270 m was cut back to 50 m and a fibre-based supercontinuum was used as the light source. The measured attenuation spectrum is shown in Figure 6.6(red curve). Remarkably, the loss remains low over a wide bandwidth and there are no sharp peaks indicating the presence of surface modes anticrossings. The sharp increases in loss below 1450 nm and at around 1750 nm indicate the edges of the photonic bandgap and are not due to surface mode coupling. Consequently, low loss is achieved over a broad spectral range; from 1450 nm to 1750 nm, covering the full spectral width of the photonic bandgap formed in the cladding. The minimum attenuation is 15 dB/km and remains below 50 dB/km over approximately 300 nm. This is the first time to our knowledge that light can be transmitted in a HC-PBGF with low loss over such a wide spectral window.

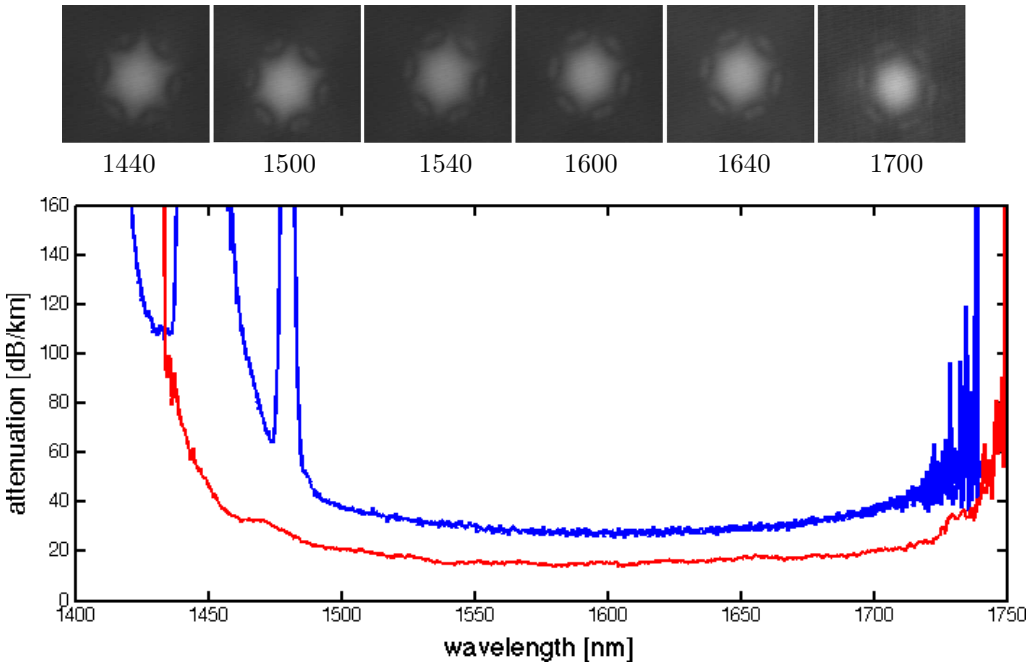

FIGURE 6.6: Measured attenuation spectrum of (red) our thin core wall fibre, and (blue) old fibre. (top) Near field images of the "fundamental" air-guided mode after 50 m of our fibre at different wavelengths within the bandgap.

The near field images shown at the top of Figure 6.6 were recorded after 50 m of the thin core wall fibre by using 10 nm bandpass filters in the wavelength range from 1440 nm to 1700 nm. These mode images confirm that light propagates in a single mode which does not couple to surface modes. In addition, the mode field patterns do not vary significantly across the transmission window.

In contrast, the attenuation spectrum of the old fibre (Figure 6.6 blue curve) shows that while both the thin core wall fibre and the old fibre have a photonic bandgap centred at almost the same wavelength, the attenuation spectrum of the old fibre is not a smooth curve but presents distinct attenuation peaks. These high loss regions are due to surface mode anticrossings occurring near the short wavelength edge of the bandgap, at around 1450 nm and at around 1480 nm. At these wavelengths surface modes couple with the core-guided mode increasing the loss and thus decreasing the effective bandwidth of the fibre [76]. Therefore, by eliminating surface modes it has been possible to increase the effective bandwidth by approximately 70 nm.

6.2.2 Group velocity dispersion

The variation of group index with wavelength was measured by low-coherence interferometery on 25 cm of fibre. Light from a supercontinuum source was launched into the fibre while ensuring that only the fundamental core mode was excited. The group velocity dispersion (GVD) for one polarization of the thin core wall fibre, together with the transmission spectrum of 50 m of the fibre, are given in Figure 6.7(a). For the second polarization similar dispersion values were found, indicating the very good structural homogeneity of the fibre. The inset Figure 6.7(a) shows the calculated modal field profile which is almost constant for all wavelengths within the low-loss transmission window.

Again as before, neither the transmission spectrum nor the GVD of the thin core wall fibre present signs of surface modes anticrossings, resulting in smooth curves right across the bandgap Figure 6.7(a). The chromatic dispersion goes from normal to anomalous with 20 ps/nm/km at the central bandgap wavelength. The dispersion slope is found to be approximately 0.3 ps/nm^2/km over a broad 200 nm spectral range from 1490 nm to 1690 nm. This is the lowest dispersion slope yet reported for a HC-PBGF and represents a factor of almost two reduction compared to the previous state-of-the-art. For the old fibre, dispersion at the central wavelength is equal to 52 ps/nm/km with a steeper GVD-slope of 0.54 ps/nm^2/km over less than 130 nm, as can be seen from Figure 6.7(b). It is worth noting that the third order dispersion of previously available HC-PBGF has been a profound limitation on their performance for at least one important application: soliton compression of high-power ultrashort pulses [67, 66].

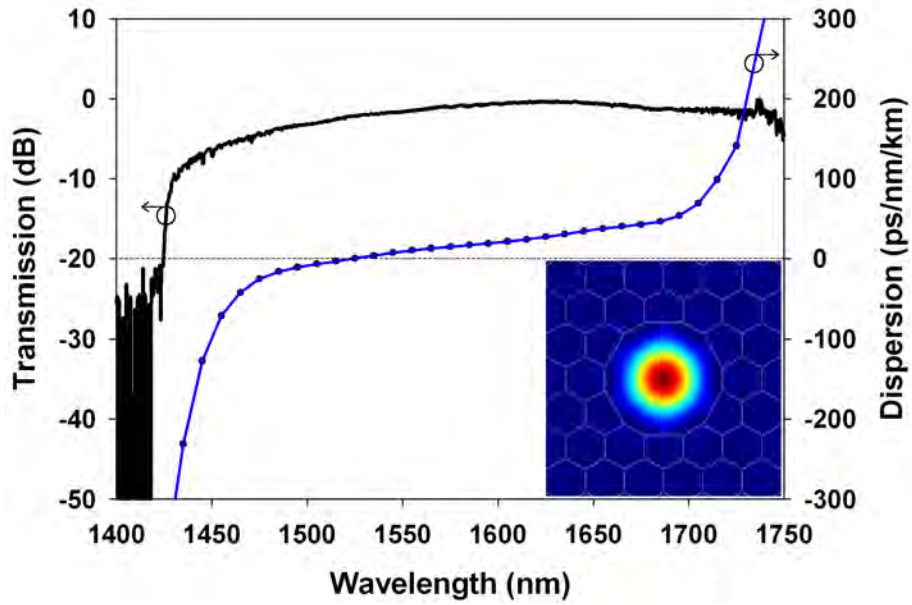

(a)

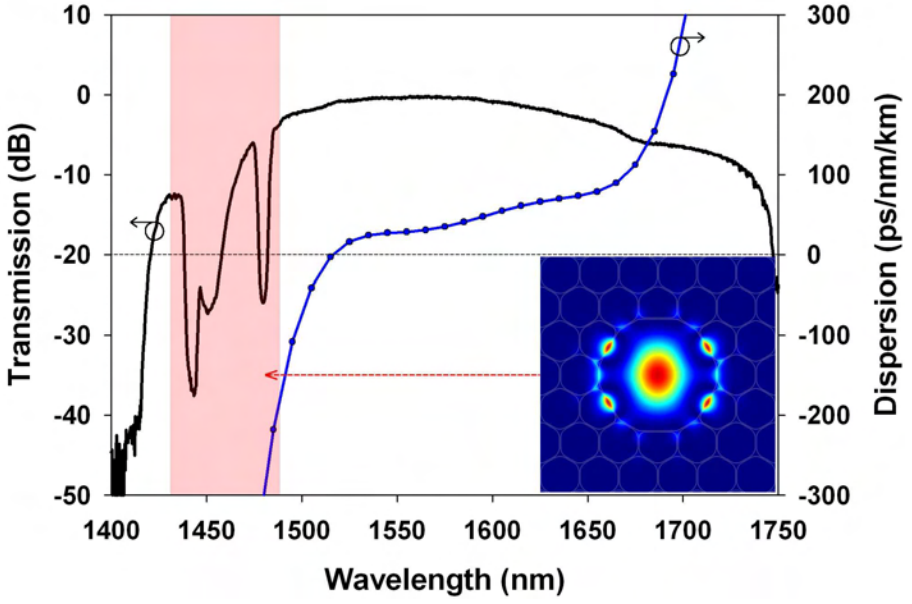

(b)

FIGURE 6.7: Group velocity dispersion measured on 25 cm of fibre and normalized transmission through 50 m of fibre. (a) Thin core wall fibre, and (b) Old fibre. Insets show results of numerical simulations for the modal field profiles in old and new fibre designs

6.3 Low attenuation (9.5 dB/km) in thin-core-wall 7-cell HC-PBGF

Figure 6.8(a) shows an SEM image of a different thin-core-wall fibre, designed for transmission at wavelengths around 1650 nm. Note that the differences between this fibre and the fibre shown in Figure 6.5(a,b) are very small and difficult to dertermine even from SEM images. However the fibre presented in this section should have a lower air-filling fraction in the cladding which results in a shift of the bandgap towards longer wavelengths as the pitch size for both fibres is almost the same. The measured attenuation spectrum in Figure 6.8(b) shows that the low loss transmission window starts at around 1560 nm. The long wavelength edge of the bandgap region could not be determined due to the limited spectral range of the optical spectrum analyzer used for the measurements. The minimum loss is 9.5 dB/km, and is almost constant over more than 100 nm. This is the lowest loss value ever reported for a 7 cell hollow core fibre (although still somewhat above the 1.2 dB/km reported in 19-cell fibres [79]). The apparent increase in loss after 1720 nm is due to the limitations of our measurement equipment and not due to surface mode anticrossings nor to the bandgap edge, and it is expected that the low loss transmission window should extend to around 1800 nm. The reduced attenuation compared to previous 7-cell fibres is at least partly due to the use of a longer wavelength and the larger core size, but the thinner core wall is expected to reduce the scattering loss, see 4 and Chapter 5. The low attenuation is strong evidence that the revised fabrication process can produce structures with sufficient regularity and integrity to compare with the previous state-of-the-art.

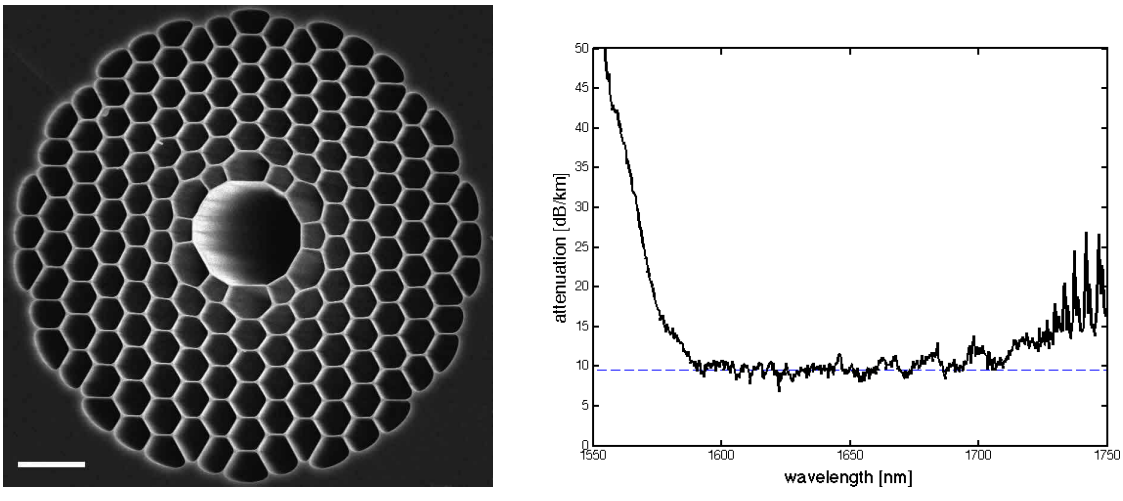

(a) (b)

FIGURE 6.8: (a) SEM image of a low attenuation 7-cell HC-PBGF designed for transmission at around 1650 nm, (bar, 10 μm). (b) Attenuation spectrum obtained from a cut-back measurement using a sample of 300 m cut back to 100 m.

6.4 Conclusions

In this chapter the fabrication and characterization of a 7 cell HC-PBGF with a novel core geometry incorporating a thin core/cladding interface has been presented. Experimental studies indicated that the fibres are able to guide light over a broader spectral window and with comparable or lower attenuation than previous state-of-the-art HC-PBGF. This is a consequence of the elimination of surface mode resonances within the bandgap. The fibre also presents the lowest dispersion slope yet reported for a HC-PBGF - a factor of almost two reduction compared to the prior state-of-the-art. The fibre design is based on the numerical computations presented in previous chapters which show that by presicely controling the thickness of the core wall and the size of the core surface mode interference can be suppressed [121, 122].

In addition, the revised fabrication process enables the production of low-loss HC-PBGFs in less than a day and offers flexibility for further optimization of the cladding structure for the formation of broader bandgaps. From the results of chapter 5 it is expected that a low loss transmission window of approximately 350 to 400 nm for a bandgap centred at 1550 nm can be obtained [122].

Although all the fibres presented here were designed to operate around the 1550 nm telecommunications window, due the ease of comparison with commercially available fibres, several fibres with operational wavelengths from 1064 nm to 1750nm which, like the fibres reported here, also do not exhibit surface modes crossings have been fabricated. This technique could also be applied to the fabrication of 19-cell HC-PBGFs, where it would greatly extend the useable bandwidth of the fibres. The transmission spectra of previously-reported 19-cell fibres have been completely dominated by surface mode crossings, and so it can be anticipated that the larger core size and greatly reduced dispersion slope in the new fibres would enable a new regime of ultrashort-pulse solitons and high-power beam delivery.

Chapter 7

Guiding mechanisms in Kagome photonic crystal fibres

In this chapter a numerical analysis of Kagome hollow-core photonic crystal fibres is presented. It is shown that although the Kagome structure does not present significant bandgaps crossing the airline, it can be very efficient at confining and guiding light in a hollow-core over a extremely broad spectral range. This is due to a strong isolation of the core guided modes from the cladding modes which inhibits the coupling of energy from the core to the cladding. A key aspect of the guidance in these fibres is the weak modal overlap between core modes and cladding modes due to rapid field spatial oscillations of the cladding modes. Two different types of cladding modes have been identified, the first type concentrates most of its energy in the cladding air regions while the second are in the silica struts. Core modes do not strongly couple to these two kinds of cladding modes either because of their large propagation mismatch or their small spatial overlap. However, for certain wavelength ranges hybrid cladding modes, whose energy is extended into both regions, exist. These modes have a high spatial overlap and small propagation constant mismatch with the fundamental core mode (they can have the same propagation constant), enabling the coupling of light from the core to the cladding and thus increasing loss. Therefore, only when anticrossings exist between the different cladding modes which leads to the existence of hybrid cladding modes can coupling between the core mode and cladding modes occur.

7.1 Introduction

Essentially there are two single material fibre geometries that have successfully demonstrated light guidance in a hollow core. The first kind, hollow-core photonic bandgap

fibres, have a synthetic photonic bandgap material surrounding the hollow core. Light introduced into the core is then unable to escape from it thanks to the bandgap that prohibits the propagation of light in the cladding region under certain conditions. In the previous chapters of this thesis the fabrication, design, and linear properties of HC-PBGFs have been extensively discussed. Since the first demonstration of a HC-PBGF [14], they have become increasingly important in many areas of optical fibre research. Hollow-core bandgap fibres can have very low loss, for example 1.2 dB/km at 1550 nm has been demonstrated for a fibre with a 19-cell core [79] and a fibre with 9.5 dB/km at 1600 nm and a 7-cell core was fabricated within this PhD project. However, the widest bandgap of the cladding of a HC-PBGF and therefore the maximum transmission bandwidth of these fibres is $\sim 40\%$ of the central wavelength of the bandgap (see chapter 3). Furthermore, interactions between the core mode and surface modes which lead to enhanced loss over particular spectral ranges reducing the useful bandwidth of most fabricated fibres. The fibres presented in chapter 6 demonstrate for the first time, core-confined guidance with low attenuation over the full bandgap of the photonic crystal cladding and with improvements to the cladding structure it should be possible to further increase the transmission bandwidth of new HC-PBGFs to 450 nm for fibres operating at a central wavelength of 1550 nm. However, for several nonlinear gas-phase optics experiments, fibres which are able to guide light in a hollow-core over a extremelly broad spectrum are desirable -even if the losses are higher compared to HC-PBGF.

A second fibre structure which guides light in a hollow-core is the Kagome fibre. In fact, the first demonstration of nonlinear propagation hollow-core PCF were carried out by Benabid *et al.* [70], who generated Raman Stokes and anti-Stokes sidebands in an hydrogen filled Kagome fibre. Recently Couny *et al.* improved the fabrication process of Kagome fibres and demonstrated air-guidance over more than 1000 nm [63, 133] which is a much broader transmission spectral range than that theoretically possible in a triangular HC-PBGF. In a very impressive result Couny *et al.* [133] used a high performance Kagome fibre to generate a Raman comb spanning from UV to IR wavelengths. Clearly this result would not have been possible to obtain in a HC-PBGF. It is also important to mention that Kagome fibres present attenuation on the order of 1 dB/km for UV/visible wavelengths [63, 133] which is similar to the minimum loss value that has been achieved with HC-PBGF for the same wavelengths [79, 84]. Although Kagome fibres have been around for several years [70], the mechanisms by which they guide have not been fully understood until very recently [134, 61, 133].

In a Kagome fibre the cladding is a periodical arrangement known as a Star of David which does not have bandgaps crossing the air line [61]. Air guidance has previously been attributed to a low density of photonic states in the cladding [61, 134, 135] and low overlap of the core mode and cladding modes [134]. Here, the cladding modes of

hollow-core kagome fibres are examined and it is shown that they fall into three distinct categories, only one of which can effectively couple to the core mode and so the core mode is effectively isolated and thus exhibits low loss.

Before discussing the modes of a Kagome fibre it is worth revisiting HC-PBGFs to look at possible loss mechanisms there and understand the differences with Kagome fibres. HC-PBGFs support three distinct mode classes: core modes, surface modes and a broad continuum of cladding modes. For the first two classes energy is localised near or in the core while the continuum modes are delocalized and energy coupled into these modes is effectively lost during propagation. Core modes can only exist for particular wavelength ranges and values of the propagation constant (i.e. within the bandgap region). Within the bandgap region, the cladding does not support modes at all and therefore light from the core cannot couple to the cladding directly. Although ideally all modes are orthogonal and do not couple, the presence of surface imperfections can lead to mode coupling which is highest between the surface modes and cladding modes. Thus any light which get coupled from the core mode to a surface mode quickly couples to the cladding modes and is lost [76]. This two fold coupling process (core mode $\rightarrow$ surface mode $\rightarrow$ cladding modes) is a dominant loss mechanism within the bandgap of the fibres and can be seen experimentally as sharp peaks in the loss spectrum of fabricated fibres [76, 15]. Instead a Kagome structure does not present a bandgap, therefore one would expect that light introcuded into the core will rapidly couple to the continium of cladding modes. However, as we will see, Kagome fibres have a variety of cladding modes which importantly present very rapid spatial oscilations. Conversely core modes are localized and present slow spatial variations thus light launched into the core mode will not strongly couple to these cladding modes leading to guidance.

In the next section the modes of a uniform Kagome structure are analyzed before introducing a low refractive index defect (hollow-core) and looking at its effects on the mode structure. Finally, the results and understanding obtained are compared to those published by Argyros *et al.* [134] and Pearce *et al.* [61] who have looked at the guidance mechanisms in Kagome fibres.

7.2 Uniform Kagome structure

The unit cell for the Kagome lattice is shown in Figure 7.1(a). In this diagram, black regions are silica with refractive index $n = 1.45$ and white regions are air. For the study presented here the period is $\Lambda = 10$ μm while the strut thickness is $T = 0.5$ μm. These parameters closely match the cladding of the fibres fabricated by Couny *etal.* [63]. Note that this structure does not support a bandgap in the wavelength range studied here

($0.4\ \mu\text{m} \leq \lambda \leq 1.8\ \mu\text{m}$) [61] and instead, to understand the guidance mechanism, it is required to analyze the different classes of cladding modes. In order to investigate the modes of the infinitely periodic structure, Maxwell's equations were solved on a unit cell with periodic boundary conditions using a finite element technique. The finite element approach is particularly suited for these fibres since the mesh size can be adapted to provide high resolution within the struts where the field present rapid variations. Since this study focuses in the coupling between the core mode and the continuum of cladding modes we have only looked at modes with an effective index close to one ($n_{eff} \approx 1$) since these are the only ones that could be expected to couple to the core mode given realistic perturbations.

Typical results of the simulations are shown in Figure 7.1(b)-(f) which shows several different modes. These can be classified into three distinct classes. Firstly there are the "airly modes" which have the power concentrated in the central hole Figure 7.1(b). The second class of modes have their energy concentrated in the silica struts and importantly, present rapid transverse variations of the optical field [see Figure 7.1(c)]. Finally, the third class of modes are hybrid modes which are a combination of both modes and are due to anticrossings between strut and airly modes. A range of these modes can be seen in Figure 7.1(d)-(f). Importantly it needs to be noted that for a particular wavelength the unit cell may not support all three mode classes. In particular, the hybrid modes only occur over limited wavelength bands.

The main argument for this study is as follows - if the cladding supports no modes that can couple to core guided modes then light could be effectively isolated from the cladding and guided with relatively low confinement loss even if their propagation constant mismatch ($\Delta\beta = k\Delta n_{eff}$) is small. Therefore, for this study the important aspect of the unit cell modes is their probability of efficiently coupling to core guided modes in a fibre. Light from the core can only be effectively coupled to cladding modes due to realistic perturbations if the interacting modes spatially overlap and present small mismatch in their propagation constants. Strut modes exist both above and below the airline and it is expected that they will present small (or even zero) propagation constant mismatch with core modes. However, these modes have rapid transverse variations of intensity along the struts [see Figure 7.1(c)(f)] resulting in a very low spatial overlap with core guided modes so light from the core can only weakly couple to these modes. Then, it is expected that airly modes would be separated from core modes in n_{eff} since the cladding holes are smaller than the core. Therefore, the coupling from core to airly modes will also be weak due to the large $\Delta\beta$ mismatch. Finally, hybrid modes are spatially extended and could have small $\Delta\beta$ with core modes which as we will see enables them to couple effectively to the core mode.

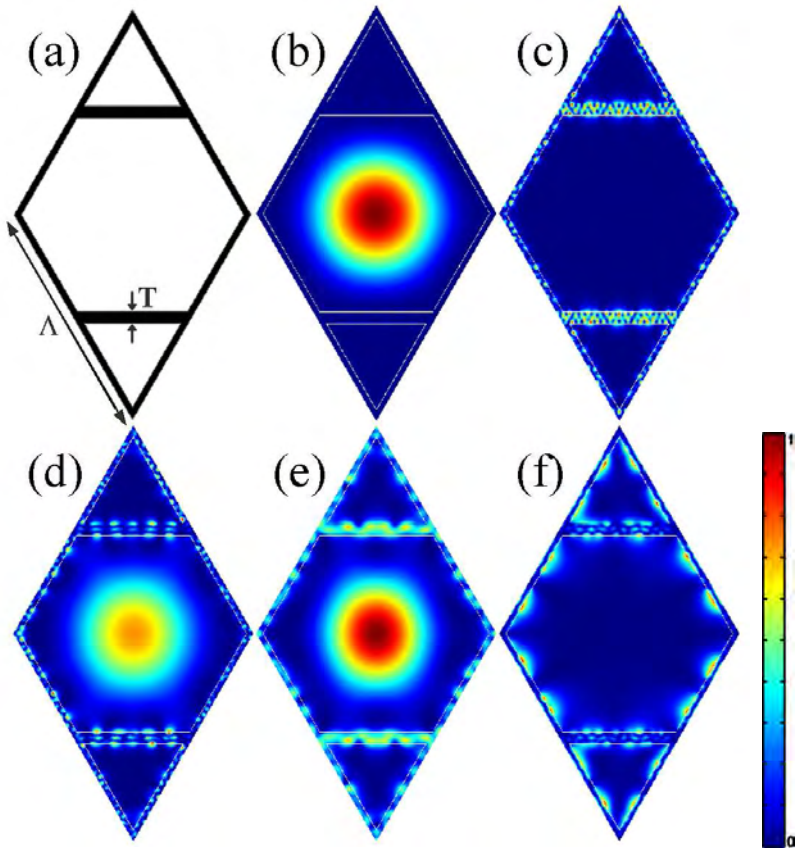

FIGURE 7.1: (a) Kagome unit cell. Examples of modes with $n_{eff} \approx 1$ of an infinitely periodic Kagome structure for different wavelengths: (b) airly mode, (c) strut mode, and (d, e, f) hybrid modes.

Thus from our knowledge of the mode structure of the unit cell we can make the following prediction about the loss structure of Kagome fibres. Such fibres could only have low loss in the frequency regions where no hybrid modes exist and should exhibit high loss in the regions where hybrid modes do exist. Note that this argument is different from the low density guidance [61, 134] in which regions where the density of states of the cladding modes are low correspond to low loss regions. To see if this argument is valid now fibre with a core defect will be studied.

7.3 Defect modes in a Kagome lattice

Turning now to the actual fibre structure itself, the single cell Kagome fibre with two rings of air holes shown in Figure 7.2(a) has been modelled, with $\Lambda = 10$ μm and $T = 0.5$ μm. As before a finite element technique with perfectly matched layers (PML) has been used to simulate the effects of a finite structure rather than a periodic boundary. We use the percentage of power in the core as a useful measure for determining the

wavelength range over which such fibres can guide light since for HC-PBGFs this has been shown to be well correlated with the loss. Unlike a HC-PBGF the guidance of a Kagome fibre does not depend on the presence of a bandgap and thus we only need to consider structures with a few rings of holes.

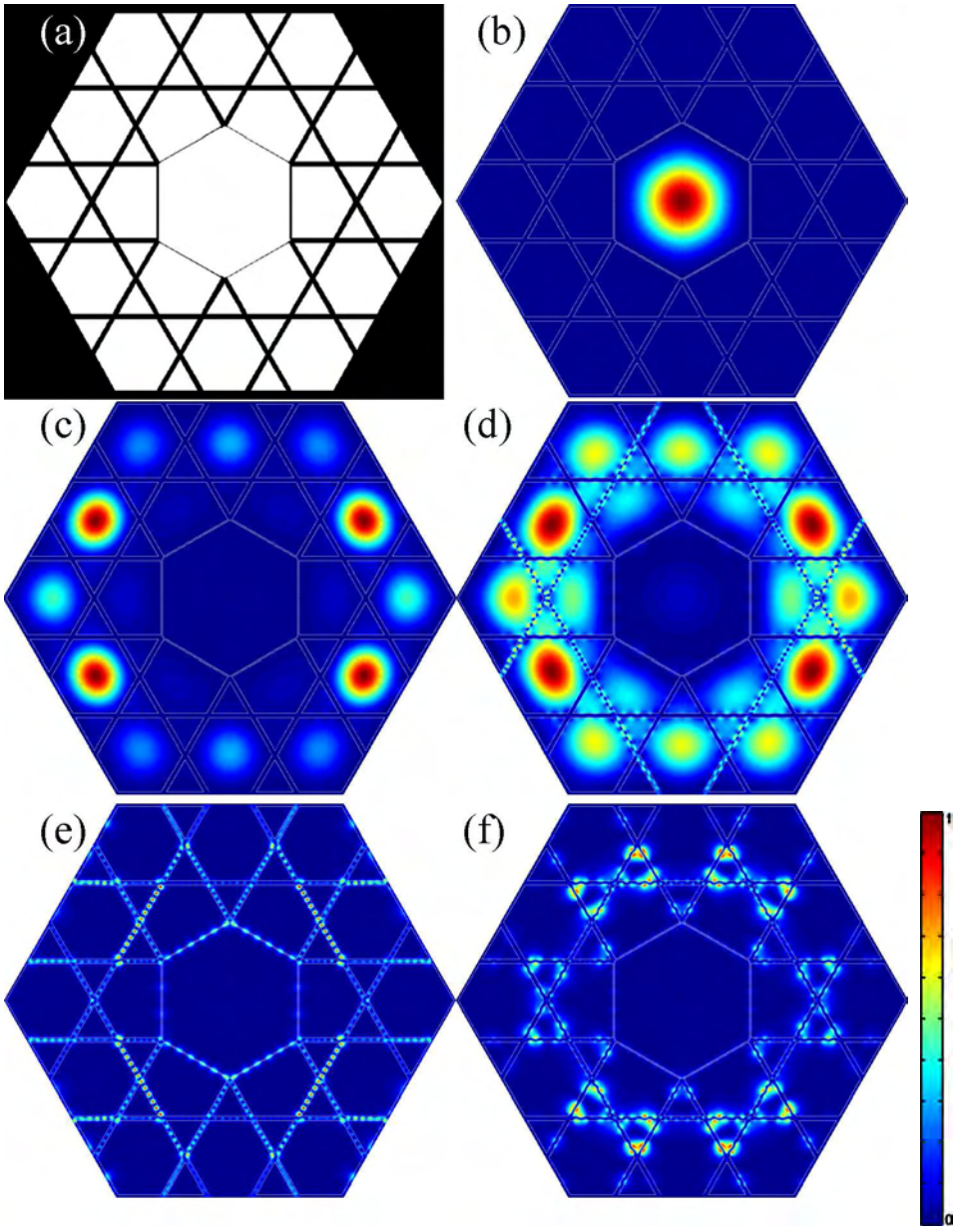

FIGURE 7.2: (a) Cross section of the analyzed single cell-core kagome fibre. (b) Mode profile of fundamental core mode. Examples of cladding modes: (c) airly mode, (d) hybrid airly mode, (e) strut mode, and (f) extended strut mode.

Figure 7.2(b)-(f) shows the variety of modes that can exist in the fibre with an effective index close to the air line. By convention the mode in Figure 7.2(b) is called fundamental core mode whilst the other modes are all cladding modes. Again there are distinct cladding modes types corresponding to the mode classes identified for the unit cell. Again as before not all of these mode types exist for a particular frequency. In order to

look at the effect of these modes in Figure 7.3(a) the different mode classes are shown in different colours: the fundamental mode in blue (solid line), airly modes in red, strut modes in black, hybrid cladding modes in green, and higher order core modes blue (dotted lines). As expected the airly cladding modes have an effective index below the air line ($n_{eff} = 1$) while the strut modes with most of the power in the silica regions extend above and below the airline. This plot shows that there are no bandgaps formed in the cladding (there are no regions without cladding modes). However, there are broad wavelength ranges where the fundamental mode only intersects with spatially complex strut modes (black): $\lambda = 0.55$ μm to 0.8 μm and 1.1 μm to 1.8 μm. Although in these regions, the propagation constant mismatch ($\Delta\beta = k\Delta n_{eff}$) between core and strut modes is small, light cannot effectively couple from the core to strut cladding modes due to their low spatial overlap. Also it is important to notice that in these regions (mainly for high frequencies) the calculated percentage of core confined energy of the fundamental mode is very large which indicates that the core mode does not extend into the cladding as shown in Figure 7.3. This is in part due to the large Λ and large core size.

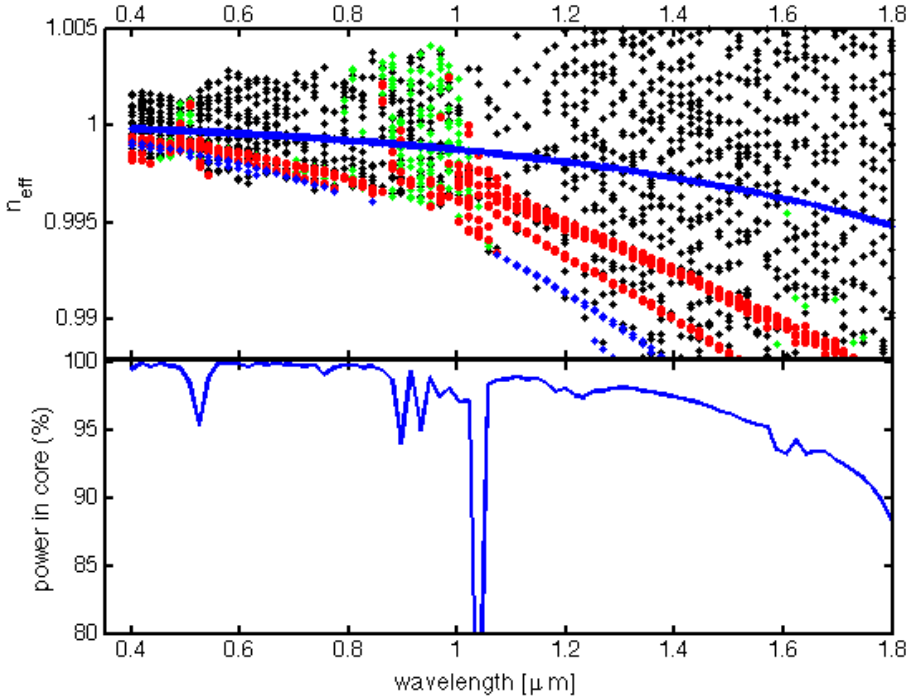

FIGURE 7.3: Calculated effective mode index *vs* wavelength the solid blue line corresponds to the fundamental mode, (blue dots) higher order core modes, (black) strut cladding modes, (green) hybrid cladding modes, and (red) airly cladding modes. (b) Percentage of power in the core of the fundamental mode *vs* wavelength.

Since the cladding air regions are smaller than the core, for most of the scan the airly cladding modes are well separated in effective index from the fundamental mode. However, at particular wavelength ranges airly modes anticross with strut modes. Such

interaction increases the effective mode index of airly modes, reducing the propagation constant mismatch with the fundamental mode. From Figure 7.3(a) we can clearly see that these anticrossings between cladding modes occur at two frequency ranges: the first one in the range 0.8 μm to 1 μm and the second at around 0.5 μm. This interaction between mode is seen as bends in the dispersion curves of the airly cladding modes. In Figure 7.2(c) we show an airly mode well before the anticrossing i.e. $\lambda = 1.4$ μm and Figure 7.2(d) shows the same mode near the anticrossing $\lambda = 1.1$ μm. This shows that airly modes away from anticrossing regions are well confined in the cladding holes therefore the fundamental core mode has a low probability of coupling into airly cladding modes due to a large $\Delta\beta$ mismatch. However, when anticrossings occur, airly modes extend into the glass struts. This certainly increases their effective index and thus the probability of coupling with the fundamental mode increases. Similarly hybrid modes as the one shown in Figure 7.2(d) represented with green dots in Figure 7.3(a) also have a high overlap with core modes and small $\Delta\beta$ mismatch. Thus in a real fibre we would expect higher losses in the frequency region with the hybrid modes (green dots) due to the enhanced coupling there. There are two high-loss regions found in this way: from $\lambda = 0.48$ μm to 0.55 μm and from 0.9 μm to 1.05 μm this is in very good agreement with transmission spectra of the fibres fabricated by Couny et.al. [63].

In conjunction with Figure 7.3(a), Figure 7.3(b) shows the percentage of light in the core for the fundamental mode. Importantly as expected the power in the core remains high except for frequencies where hybrid modes exist. In these wavelength regions the percentage of power in core of fundamental mode presents sharp drops that are due to mode anticrossings. Also compared to a HC-PBGF the power in the core remains high over a wide bandwidth and there is no sharp drop-off indicating the presence of a photonic bandgap.

7.4 Conclusions

In this chapter the loss mechanisms of a Kagome fibre in relationship to the presence or absence of particular cladding modes have been discussed. By looking at the different types of cladding modes it is possible to predict the frequency regions where a Kagome fibre will be able to guide light. The results are in very good agreement with transmission measurements of fabricated fibres [63].

The broad guidance in Kagome fibres is due to the particular structure of the modes of the cladding which are either highly spatially structured and present high frequency spatial oscillations within the thin glass struts or are well separated in propagation constant from the fundamental mode and so cannot effectively couple to the fundamental

core mode. Only when anticrossings exist between these two different cladding modes which leads to the existence of "hybrid" cladding modes, can coupling between the core mode and the cladding occur.

Recently Pearce *et al.* examined the loss properties of Kagome fibres using two simplified models and a Kagome fibre structure [61]. They were able to predict the frequencies over which a Kagome fibre can guide. However, they did not look at the structure of cladding modes which is fundamental for understanding why these fibres can guide light. Here an explanation of the cladding modes structure that allows the guidance is presented. Our understanding of the guidance in Kagome fibres is very similar to that of Couny *et al.* [133]. Combining these results one can thus gain a more complete understanding of the guidance mechanism of Kagome fibres.

Chapter 8

Bandgap guided modes in large mode area photonic crystal fibres

Differently to previous chapters, the work presented in this chapter focuses on the study of silica photonic crystal fibres in which light is guided in a solid core. Although most solid core PCF guide light by a modified form of total internal reflection, it has recently been shown that the periodic structure of the cladding of these fibres can lead to the guidance of additional higher-order core modes due to bandgaps formed in the cladding. Numerical calculations presented here show that these additional modes have effective indices below the average cladding index and are located within bandgap regions. Additionally, it is demonstrated that these higher-order core modes can exist even when the cladding does not present a bandgap. In this case, the modes lie in regions with low density of optical states in the cladding. Remarkably, such modes can be present in silica PCFs with $d/\Lambda < 0.4$ that would be considered to be single-mode by index guiding considerations alone.

Excellent agreement between theoretical predictions and experimental observations is demonstrated. These higher-order modes can be visible in metre lengths of fibre with input power of few mW. The fraction of power propagating in these higher-order modes can be effectively minimized by optimizing the coupling conditions for the fundamental mode and also by bending the fibre. However, the presence of these bandgap guided modes may detrimentally impact the application of standard PCF designs where control over the fibre input is limited and where mode quality is important, such as modal filtering [136].

The work presented here was carried out in conjunction with Dr. Joanne Flanagan, my contribution to this work was on the calculation of the optical DOS used for understanding the guidance of these additional modes.

8.1 Introduction

Several studies have shown solid core silica photonic crystal fibres to be an attractive alternative to conventional step-index designs in the large core single-mode regime, with particular advantages in applications such as wide bandwidth data transmission, dual-wavelength single-mode power delivery and broadband wavefront filtering [136, 137, 138, 139]. However, in the vast majority of previous work on large mode area photonic crystal fiibres, only a subset of the core modes guided by these fibres has been considered. Here it is demonstrated that the periodicity of the cladding structure itself can lead to additional higher-order modes with relatively low losses.

The optical properties of index guiding PCFs (at any given wavelength) are generally assumed to be analogous to those of step-index fibres; i.e. the guided core modes possess effective indices (n_{eff}) that lie between an average cladding index (n_{clad}) and the core index (n_{core}), i.e. $n_{clad} < (n_{eff} = \beta/k) \leq n_{core}$, where β is the propagation constant of the mode, λ is the wavelength of light and $k = 2\pi/\lambda$ [12] (see chapter 2).

However, index-guided PCFs typically possess a cladding defined by a highly regular triangular lattice of air holes with a hole-to-hole spacing (Λ) and a relative hole size (d/Λ). It is well known that large air holes ($d/\Lambda > 0.8$) in this configuration can be used to create bandgaps that permit guided modes to be trapped with low loss within a hollow core [14]. It is perhaps less well remembered that this cladding structure also gives rise to bandgaps at smaller hole sizes more typically associated with single-mode index-guiding photonic crystal fibres (for which d/Λ is typically in the range of 0.4 - 0.5) [10]. However, theoretical work has clearly shown that silica PCFs with high-index defect cores and $d/\lambda \approx 0.5 - 0.6$ are capable of supporting core localized modes with $n_{eff} < n_{clad}$ via bandgap effects, in addition to index-guided modes with $n_{clad} < n_{eff} < n_{core}$ [140, 141]. So far, these studies have only considered PCFs with small structure scales relative to the wavelength of light ($\Lambda/\lambda \approx 1.0$) and the additional bandgap modes in this instance are predicted to have extremely high confinement losses (in excess of 500 dB/m for 8 rings of air holes) [141]. However, since the confinement losses of guided modes in PCFs are known to decrease as Λ/λ increases, these studies raise important questions about the nature of true single-mode guidance at larger structure scales: i.e. in large mode area silica PCFs, where Λ/λ is roughly an order of magnitude larger.

Furthermore, it is also known that a bandgap is not necessary in order to create relatively low loss guidance (as for the Kagome fibre [63, 61, 134] analyzed in Chapter 7); defect modes with relatively low propagation losses can be localized within a region of low density of cladding modes [142, 61, 134, 133]. Here it is demonstrated that it is necessary to consider the DOS and not just those regions where the DOS is zero (i.e. the bandgaps) in order to explain all the modes guided in large mode area solid core PCFs.

The aim of the study presented here is to investigate both numerically and experimentally the guidance properties of large mode area silica PCFs (with $\Lambda/\lambda \approx 10$), looking specifically at core localized modes whose guidance mechanism results directly from the presence of bandgaps and regions of low DOS in the cladding. All the fibres considered here comprise a triangular lattice of air holes in silica glass with a core formed by the omission of a single air hole. Within the following sections numerical and experimental evidence for core localized modes with $n_{eff} < n_{clad}$ in index-guiding single-material PCFs is presented. These bandgap guided modes can be observed over a broad range of wavelengths and are sufficiently well confined to be apparent in metre lengths of fibre. In addition, similar modes in solid core PCFs that do not result from a bandgap are also observed. These modes exist in regions of low DOS formed in the cladding.

8.2 Numerical methods

A brief description of the numerical methods used here to evaluate guidance properties in large mode area holey fibres is presented in this section. The key properties considered here are: the density of states (DOS) in the infinite cladding, the effective index of the fundamental space filling mode (FSM) of the infinite cladding and the modal properties of the defect states (i.e. the core modes) for a finite structure. The effective index of the FSM (n_{FSM}) can be thought of as an 'average' cladding index, such that all modes with $n_{eff} > n_{FSM}$ are defined to be index-guided modes. The density of states (DOS) is the number of allowed modes of the infinite cladding with a given frequency ω and is defined by the integral in equation 3.4.

In order to evaluate the integral in equation 3.4 the linear tetrahedron method in its corrected symmetry form, presented in [142] was used. The values of $\omega_n(k)$ were calculated using a full vector FEM with periodic boundary conditions, at 66 k points in the irreducible Brillioun zone. The DOS presented here are normalized against the vacuum DOS. Note that the DOS are mapped onto plots of wavelength *vs.* effective mode index as these are most relevant parameters in terms of intuitively understanding the guidance properties of PCFs. Example DOS maps for an infinite triangular lattice of circular air holes in silica glass ($n = 1.44$) are shown in Figure 8.1 for four different values of d/Λ, where the dotted black line in each case corresponds to the n_{FSM} (also calculated using the same full vector FEM). The values of λ/Λ shown here correspond to the large mode area regime for visible to near-infrared wavelengths. Index-guided modes of the core are located within the white region above n_{FSM}, while all cladding modes are located below n_{FSM}. The plots in Figure 8.1 clearly show that there are several bands of zero, or near zero values of DOS, in which core modes could potentially be localized, even for very small values of d/Λ.

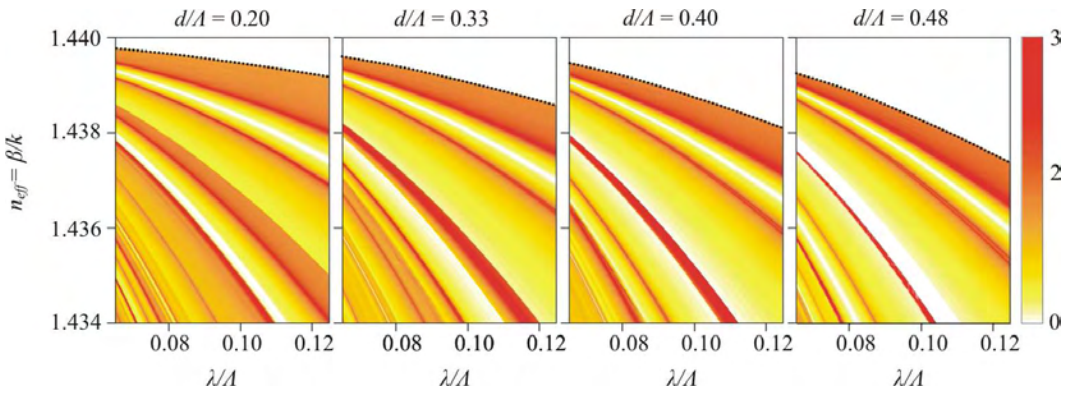

FIGURE 8.1: DOS maps for an infinite triangular lattice of circular air holes in silica glass (n = 1.44) with (a) $d/\Lambda = 0.20$, (b) $d/\lambda = 0.33$, (c) $d/\Lambda = 0.40$ and (d) $d/\Lambda = 0.48$.

The modes supported by the different fibres are modelled using the FEM modal solver described in section 3.3.2, using PMLs to allow the confinement losses (C_{loss}) to be evaluated. When considering real fibres, idealized refractive index profiles with the parameters Λ, d/Λ and N extracted from SEM images are used - where N is the number of rings of air holes. In all the following calculations, no material dispersion is consider and the refractive index of silica is assumed to be 1.44 at all wavelengths. Core localized modes are identified by evaluating the percentage of power in the core (P_{core}), defined as the percentage of power within the first two rings of air holes.

8.3 Results

In this section the guided modes of the two large mode area PCFs shown in Figure 8.1 are studied. Based on index-guiding considerations alone, the first fibre is defined as endlessly single mode (fibre A) and the second is defined as effectively singlemode (fibre B). The term 'endlessly singlemode' is historically associated with values of $d/\Lambda \lesssim 0.40$ and is based upon considerations of the cut-off of the LP_{11}-like mode [13, 143]. Fibres with a d/λ slightly larger than this value (up to $d/\Lambda \approx 0.5$) are also generally considered to be effectively single-mode in practice. Indeed, most commercially available large mode area PCFs described as single-mode have values of d/Λ slightly larger than the strict theoretical minimum [143, 84]. The justification for this is that the higher-order modes tend not to be observed in practice, particularly in applications involving several metres of curved fibre with a near-Gaussian input beam. In such cases, low coupling efficiency to the higher-order modes combined with a greater susceptibility to bend induced loss (relative to the fundamental mode) typically results in an output beam with a negligible higher-order mode component. The larger values of d/Λ are prefered as they lessen the

effects of bend induced attenuation, which represents the main limiting factor on mode size in the single-mode (and near single-mode) regime [144].

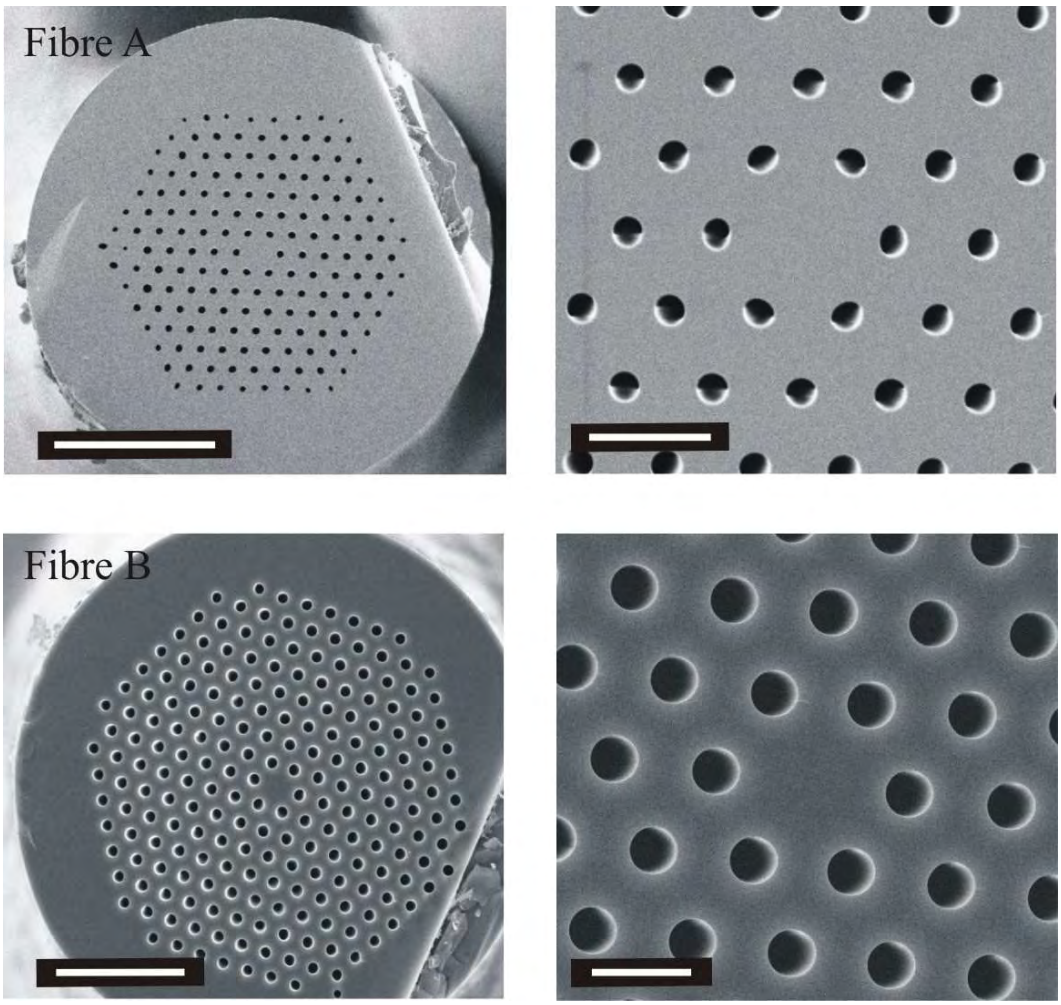

FIGURE 8.2: Top: SEM micrographs of fibre A: scale bars are 100 μm (left hand side) and 20 μm (right hand side), $\Lambda = 11.7\,\mu$m, $d/\Lambda = 0.33$, $N = 7$. Bottom: SEM micrographs of fibre B: scale bars are 100 μm and 10 μm (right and left image respectively) $\Lambda = 10\,\mu$m, $d/\Lambda = 0.48$, $N \sim 8$.

Both fibres A and B are made entirely from a single grade of synthetic silica glass (F300 from Hereaus) and were fabricated at the ORC using the stack-and-draw approach. The cladding region in these fibres is formed by a triangular lattice of air holes and the solid core is surrounded by at least 7 complete rings of holes. SEM images of these fibres are shown in Figure 8.2. Theoretical predictions of the modal properties of these two fibres are shown together with the results from experimental characterization in the following sections.

8.3.1 Modal properties of fibres A and B

8.3.1.1 Fibre A: $\Lambda = 11.7\,\mu$m, $d/\Lambda = 0.33$

The guidance properties of fibre A, calculated using the techniques outlined in Section 8.2, are summarized in Figure 8.3. The main property map in Figure 8.3 shows the DOS plotted as a function of n_{eff} *vs.* λ. Red shading indicates regions where the periodic cladding has a high density of modes, while regions of pale yellow correspond to low density of modes of the periodic cladding. White areas correspond to photonic bandgaps in which the cladding does not support modes at all (i.e. DOS = 0). Grey shaded regions indicate parameters outside the computational domain. The dotted black line shows n_{FSM} and the dashed blue lines correspond to core localized modes with $P_{core} > 25\%$ - modes that satisfy this condition will be refereed as core (defect) modes. Intensity profiles typical of each distinct mode group are shown on the right hand side of the main plot (size of computational box shown = 50×50 μm). These results show that in addition to the fundamental mode fibre A supports at least five distinct core localized mode groups with $n_{eff} < n_{FSM}$, labelled *i*, *ii*, *a*, *b* and *iii*. This nomenclature has been chosen to reflect the fact that modes *a* and *b* become located within a bandgap as d/Λ increases. See Section 8.3.1.2 for more details.

Via symmetry arguments it was found that all modes except those of type *a* consist of a degenerate pair, while the modes in group *a* comprises two non-degenerate modes and one degenerate mode pair. Note that core modes with $n_{eff} < n_{FSM}$ are located near a local minimum in the DOS, which demonstrates that the DOS is a useful technique for predicting the general location of defect modes. It should also be appreciated that DOS > 0 for all modes with $n_{eff} < n_{FSM}$ in this fibre.

Selected properties for the defect modes shown in Figure 8.3 are presented in table 8.1 for $\lambda = 1.064\,\mu$m, where n_{min} is an estimate of the minimum coupling loss it is possible to achieve with a Gaussian input. This value is calculated by evaluating the field overlap for an input Gaussian beam that is centered on the highest peak in the modal intensity profile, scaled to a similar width. T_{max} is the theoretical maximum power transmitted over 50 cm length, assuming loss contributions from mode confinement and coupling efficiency only. By considering the properties shown in Table 1, it can be seen why certain modes are visible in practice, while others are not. For example, it is clearly seen that with such large values of C_{loss}, modes *i*, *ii and a* will almost certainly be undetectable for the length scales ($50 - 100$ cm) and input power levels (few 100 mW maximum) considered here. However, the values of T_{max} for modes of type *b* and iii suggest that these modes may be visible in practice.

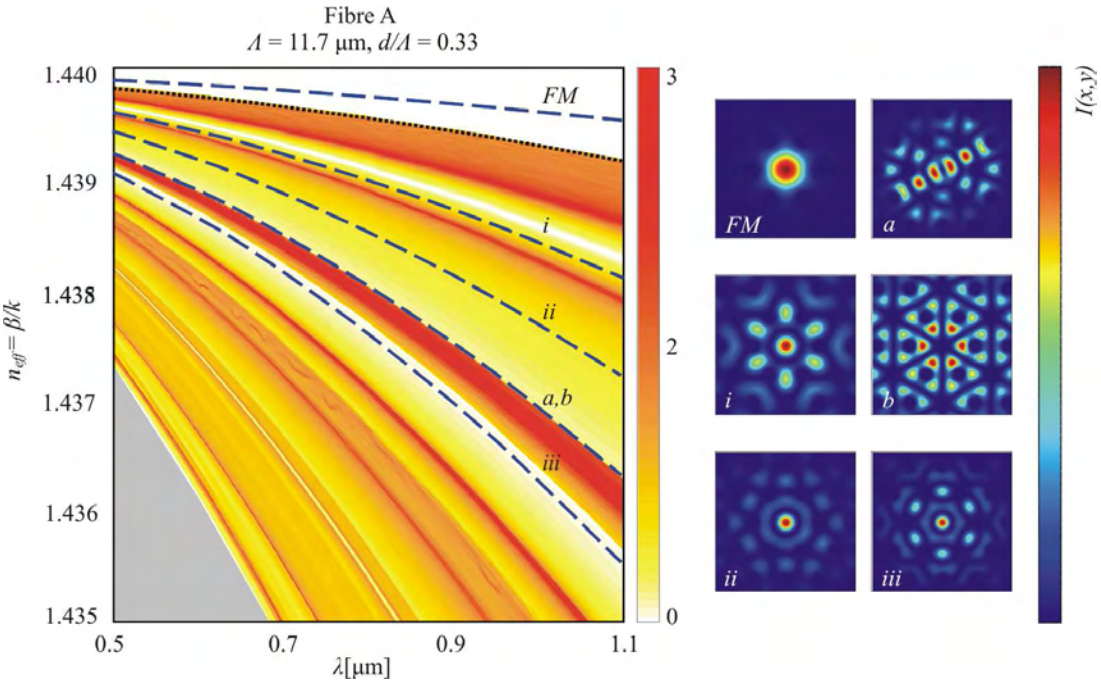

FIGURE 8.3: Main plot: colour shading shows the density of states for a triangular lattice of air holes with $\Lambda = 11.7\,\mu$m and $d/\lambda = 0.33$ in silica glass (n = 1.44). Dotted black line corresponds to n_{FSM}. Dashed blue lines indicate positions of core localized (defect) modes, shown to the right of the main plot for $\lambda = 1.064\,\mu$m.

Mode Type	n_{eff}	P_{core}%	C_{loss} [dB/m]	η_{min} [dB]	T_{max} % (50 cm)	Observed
FM	1.43960 1.43960	100	$\sim 10^{-9}$	0.13	~ 97	Yes
i	1.438219 1.438217	58	$\sim 10^{2}$	11.3	$\sim 10^{-18}$	No
ii	1.437362 1.437359	36	$\sim 10^{3}$	11.5	$> 10^{-50}$	No
a	1.436563 1.436565 1.436565 1.436567	90	~ 140	11.0	$\sim 10^{-8}$	No
b	1.436504 1.436500	63	~ 7	14.4	~ 2	No
iii	1.435816 1.436500	90	~ 8	9.9	~ 4	Yes

TABLE 8.1: Mode parameters for $\Lambda = 11.7\,\mu$m, $d/\Lambda = 0.33$ at $1.064\,\mu$m (n=1.44)

Experimental characterization was performed at $\lambda = 1.064\,\mu$m using a single-mode Nd:YAG laser with an output power of $\sim 100\,$mW, coupled into a short length of fibre A ($\approx 50\,$cm) using a single input lens. The various different modes guided were

explored by varying the launch conditions (i.e. input beam width, choice and position of input lens) and were recorded by imaging the near-field output of the fibre onto a CCD camera. As expected, characterization reveals core localized modes with spatial profiles far more complex than the FM of the fibre. Detailed investigation shows that intensity profiles with similar spatial structure to that of mode *iii* can be clearly isolated for certain off-axis launch conditions [shown in Figure 8.4(a)]. However, no contribution from mode type *b* was detected (despite similar values of T_{max} to mode *iii*). There are several possible reasons for this; in this fibre mode *b* is significantly larger than mode *iii*, with $> 40\%$ of power distributed beyond the second ring of holes. In addition, the DOS surrounding mode *b* is also larger than that around mode *iii* in this instance, see Figure 8.3. As a result, one would expect that losses from coupling to highly leaky cladding modes due to perturbations (i.e. micro and macro bends and fibre irregularities) to be larger for mode *b* than mode *iii*.

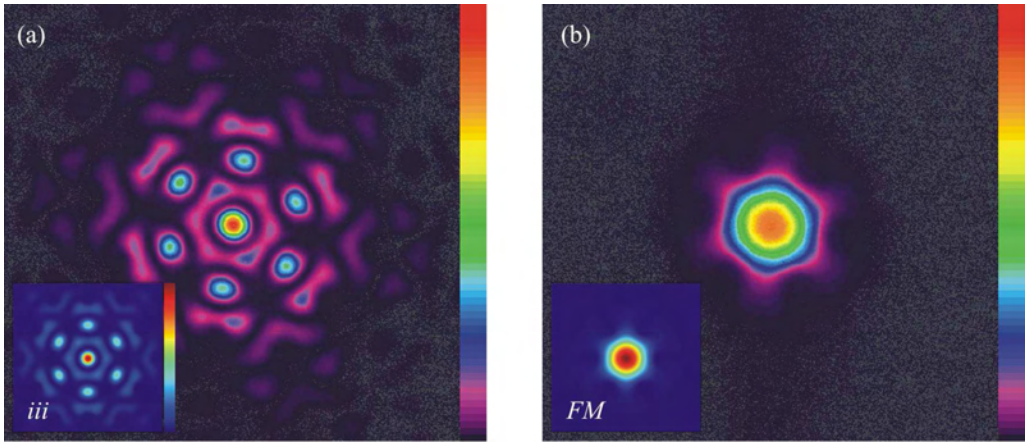

FIGURE 8.4: Example near-field output intensity profile from a 50 cm straight length of fibre A at $\lambda = 1.064\,\mu$m for (a) optimized (on-axis) launch conditions and (b) detuned (off-axis) launch conditions. Corresponding predicted mode profiles are shown in inset.

Example near-field intensity profiles observed in this fibre for $\lambda = 1.064$ μm are shown in Figure 8.4. The corresponding predicted intensity profiles (shown inset in (a) and (b) for mode *iii* and the FM, respectively), demonstrate excellent agreement between theoretical calculations and observations. This fibre was also characterized at a range of wavelengths between $\lambda = 457$ and 633 nm by launching collimated light from tunable single-mode Argon-ion and helium-neon lasers (output power in the range of $5-70$ mW). Mode *iii* was observed at all wavelengths within this range and, other than the FM, is the only mode observed in this fibre. Using a singlemode input beam, we find that it is only possible to isolate mode *iii* (shown in Figure 8.3(a)) by reducing the beam size far below that which is optimal for coupling into the FM and by using off-axis launch conditions. From this study, it is estimated that it is possible to couple $< 5\%$ of the incident power into mode *iii* in isolation (which agrees well with theoretical estimations,

shown in table 8.1). For single-mode launch conditions that are well matched to the fundamental, it was found that it is not possible to detect any higher-order component in the fibre output (based solely on visual inspection of the near and far-field output beam profile). Furthermore, bend induced losses of the fundamental mode and mode *iii* are sufficiently disparate to enable an effectively single-mode output to be achieved for certain bend conditions, independent of the launch parameters.

8.3.1.2 Fibre B: $\Lambda = 10.0\,\mu$m, $d/\lambda = 0.48$

As before, the main property map for this fibre (shown in Figure 8.5) shows the DOS, together with the dispersion curves for the fundamental space filling mode (dotted black line) and core localized modes (dashed blue lines) as a function of n_{eff} vs. λ. There is a large degree of similarity between this plot and the one shown in Figure 8.3 for fibre A. At first glance, the main differences are that a photonic bandgap (DOS = 0) has opened up around the position of modes *a* and *b* and that additional higher-order modes are present, both above and below n_{FSM}.

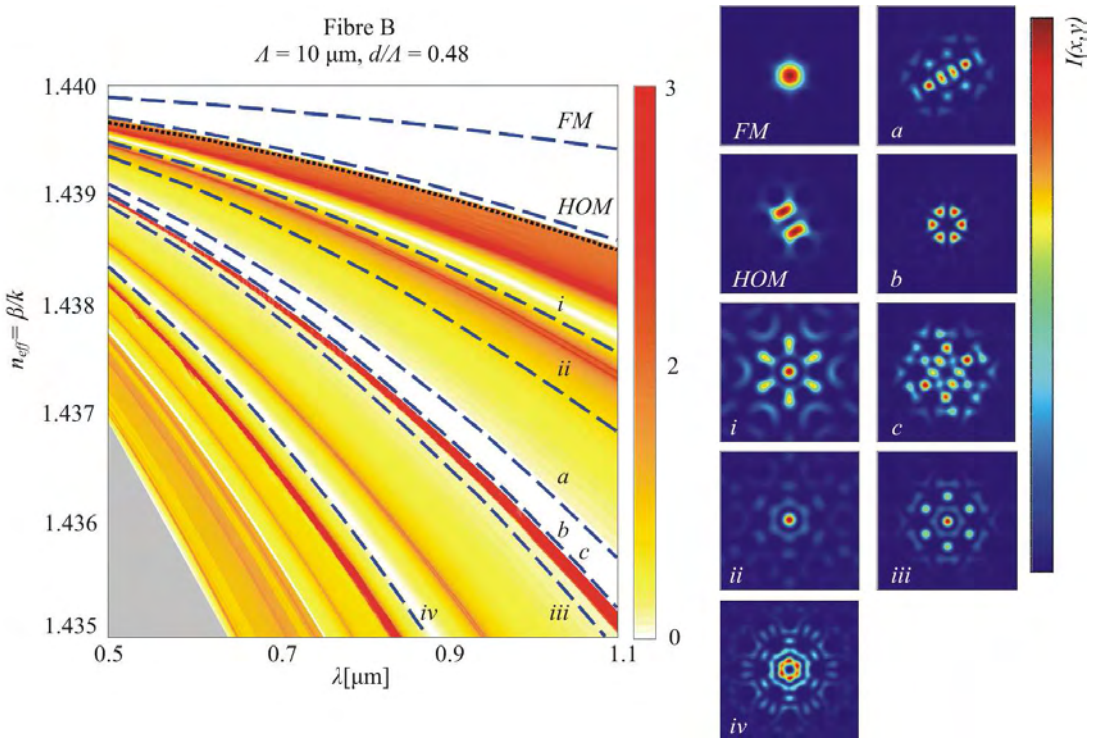

FIGURE 8.5: (a) Colour shading shows the density of states (DOS) for a triangular lattice of air holes with $\Lambda = 10.0\,\mu$m and $d/\lambda = 0.48$ in silica glass. Dotted black line corresponds to n_{FSM}. Dashed blue lines indicate positions of core localized modes, shown to the right of the main plot for $\lambda = 1.064\,\mu$m.

The calculations presented in Figure 8.5 show that within the domain of index-guidance, fibre B supports the first higher-order multiplet (*HOM*), in addition to the fundamental

mode (FM) pair. These modes are equivalent to the HE_{11}, TE_{01}, TM_{01} and HE_{21} modes of a step index fibre. These calculations also show that fibre B supports at least seven additional mode groups for $n_{eff} < n_{FSM}$. Representative intensity profiles for all modes indicated on the property map in Figure 8.5 are shown to the right hand side of this plot (size of computational box shown = $50 \times 50\,\mu$m) and selected properties for these defect modes at $\lambda = 1.064$ μm are presented in table 8.2. Once again, based on symmetry analysis, it was found that sets i, ii and b comprise a degenerate mode pair while sets a, c and iv each comprise two non-degenerate modes and one degenerate mode pair. The first two mode groups with $n_{eff} < n_{FSM}$ (modes of type i and ii), possess similar properties to those seen previously in fibre A, with a relatively low degree of core localization and high values of confinement loss. As such, these modes are not expected to be observed for the length scales (50 − 100 cm) and input powers (few 100 mW maximum) considered in this study. The same is also true for mode type iv. However, as can be seen from table 8.2, the predicted values of T_{max} for mode groups a, b, c and iii are of similar magnitude to those modes with $n_{eff} < n_{FSM}$ observed in fibre A, and thus it is expected these modes to be visible in practice. Note that modes a, b and c lay on zero density of state regions, thus these modes are defined as bandgap guided modes.

By comparing the maps in Figure 8.3 and Figure 8.5 it is possible to understand some differences between modes of type a and b for both fibres. The cladding of fibre A does not present a bandgap around the position of core modes a and b exist. However, as d/Λ increases to 0.48 (as in fibre B), a bandgap opens up and these core modes are more isolated from cladding modes. As the bandgap opens up it also prevents core modes from extending into the cladding and results in a large increase in the core confined energy for modes of type b (from 63% in fibre A to 98% in fibre B) and a decrease in leakage loss for both mode types.

Again as before, characterization of the guided modes at $\lambda = 1.064$ μm reveals the presence of modes with spatial profiles far more complex than the FM or the first HOM of this fibre. On more detailed investigation it was found that output intensity profiles with similar spatial structure to the modes of type a, b and c can be observed, and in some cases isolated, for certain off-axis launch conditions. However, no contribution from mode type iii was detected - the possible reasons for this are discussed later in this section. A selection of the various near-field intensity profiles observed in this fibre for $\lambda = 1.064\,\mu$m are shown in Figure 8.6. Comparison with the intensity profiles shown previously in Figure 8.5 demonstrates that there is good agreement between the observed fibre output and the predicted mode shapes, particularly in Figure 8.6(a,b,c), which clearly correspond to the FM, type a and type b modes respectively. The intensity profiles shown in Figure 8.6(d,e) are not as simple to classify as these profiles probably

Mode Type	n_{eff}	P_{core}%	C_{loss} [dB/m]	η_{min} [dB]	T_{max} % (50 cm)	Observed
FM	1.439230 1.439230	100	$\sim 10^{-12}$	0.10	~ 98	Yes
HOM	1.438148 1.438149 1.438151 1.438152	99	$\sim 4 \times 10^{-4}$	4.5	~ 36	Yes
i	1.436823 1.436820	67	$\sim 2 \times 10^{2}$	11.9	$\sim 10^{-18}$	No
ii	1.435875 1.435873	24	$\sim 4 \times 10^{2}$	12.6	$> 10^{-50}$	No
a	1.434402 1.434404 1.434406 1.434408	98	~ 8	9.0	~ 5	Yes
b	1.433826 1.433819	99	~ 0.001	12.9	~ 5	Yes
c	1.433800 1.433795 1.433791	97	~ 10	10.6	~ 3	Yes
iii	1.433319 1.433323	96	~ 1	10.1	~ 9	No
iv	1.429828 1.429827 1.429814 1.429794	65	$\sim 1 \times 10^{3}$	15.6	$> 10^{-50}$	No

TABLE 8.2: Mode parameters for $\Lambda = 10.0\,\mu$m, $d/\Lambda = 0.48$ at $1.064\,\mu$m (n=1.44)

result from a superposition of multiple modes. However, symmetry similarities between these intensity profiles and the type c mode shown in Figure 8.5 are present.

As seen previously for fibre A, it is only possible to observe contributions from bandgap modes by reducing the beam size far below that which is optimal for coupling into the fundamental and by using off-axis launch conditions. However, for single-mode launch conditions that are well matched to the fundamental mode, it is not possible to detect any higher-order component in the fibre output (based solely on visual inspection of the near and far-field output beam profile). Furthermore, the bend induced losses of the fundamental mode and all other modes of fibre B are sufficiently disparate to enable an effectively single-mode output to be achieved for certain bend conditions, independent of the launch parameters.

This fibre was also characterized at a range of wavelengths between $\lambda = 543$ and 633 nm by launching collimated light from a tunable helium-neon laser (output power in

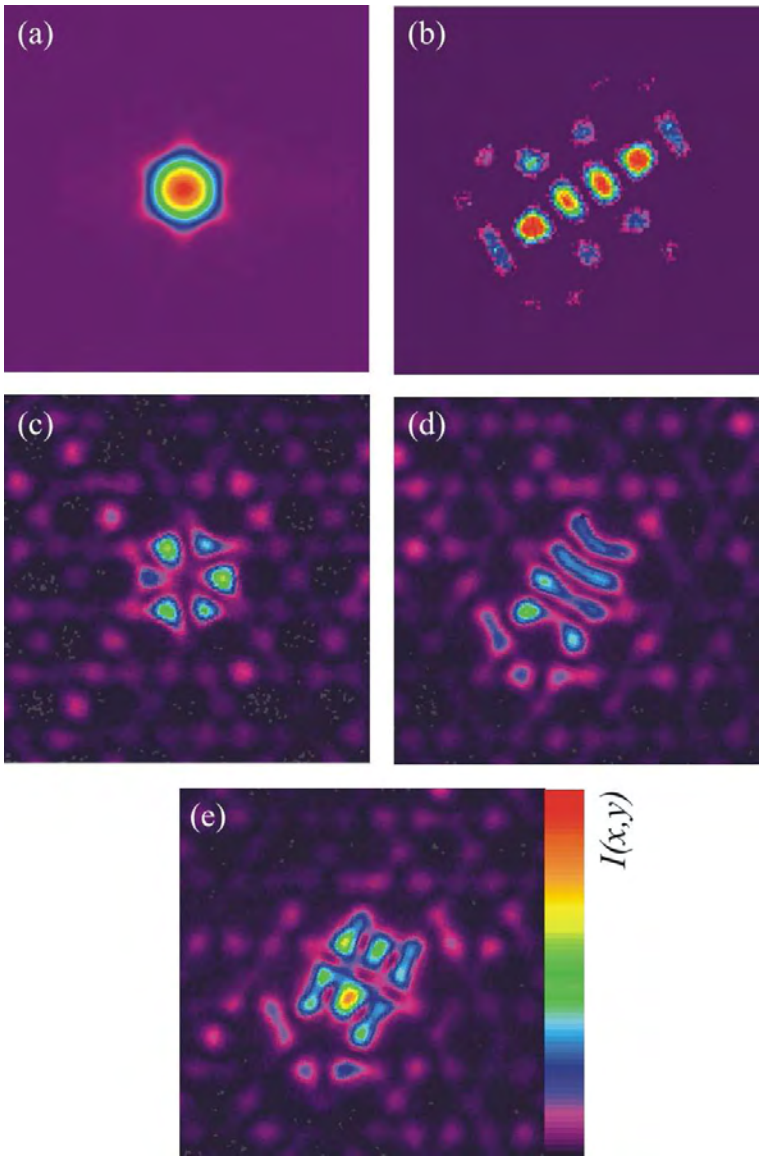

FIGURE 8.6: Experimental observations at $\lambda = 1.064\,\mu$m: near-field intensity profiles of fibre B for varying launch conditions. (a) bend radius ≈ 20 cm, length ≈ 1 m, (b) straight fibre, length ≈ 1 m, (c) - (e) straight fibre, length ≈ 25 cm.

the range of 1 - 5 mW). Similar results to those at $1.064\,\mu$m were achieved: while contributions from modes of type *a*, *b* and c were apparent at all wavelengths considered, no spatial similarities with mode type *iii* were observed in the fibre output profile. A possible reason for this becomes apparent by looking at the detail of the DOS for this type of structure close to the position of mode *iii*.

Figure 8.7 shows the DOS around $\lambda/\Lambda = 0.1$ (wich correspond to $\lambda \approx 1064$ μm for fibres A and B) for an infinite triangular lattice of circular air holes in silica glass ($n = 1.44$) with four different values of d/Λ. The blue dashed lines on each plot indicate the position of mode type *iii*. As can be seen from these plots, both the position of mode *iii* and the pattern of the DOS in this region change with hole size; as d/Λ increases,

the n_{eff} of mode *iii* falls, while the local minima in the DOS moves to higher values of n_{eff}. Mode *iii* is positioned in lower DOS regions for values of d/Λ between 0.33 and 0.40. For values of d/Λ either side this of range the DOS increases at the position of mode *iii*, which suggests that this mode may only be apparent under the experimental conditions considered here from a narrow range of structures. This is in agreement with observations; mode *iii* has not been observed in large-mode-area photonic crystal fibres with $d/\Lambda < 0.2$ or in those with $d/\Lambda < 0.46$ (i.e. fibre B) but has been observed in fibre A ($d/\Lambda = 0.33$).

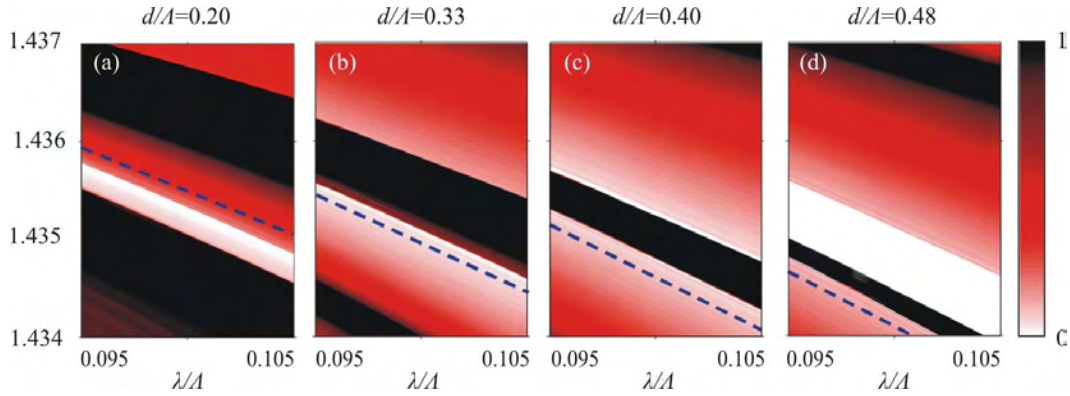

FIGURE 8.7: DOS maps for an infinite triangular lattice of circular air holes in silica glass with (a) $d/\Lambda = 0.20$, (b) $d/\Lambda = 0.33$, (c) $d/\Lambda = 0.40$ and (d) $d/\Lambda = 0.48$ (shown on a smaller scale than in previous figures). Dashed blue lines correspond to mode type *iii*.

8.4 Conclusion

The effects of the cladding periodicity on the defect modes guided by large-mode-area silica microstructured fibres (PCFs) were investigated. The results presented here show that when the dielectric structure of the fibre cladding forms a photonic crystal (in this case, from a triangular lattice of air holes), additional defect modes whose guidance can not be explained by average index effects can be localized in the fibre core. Numerical calculations show that these additional modes have effective indices below the average cladding index and are located within bandgap regions and local minima in the density of states (DOS). This theoretical work also shows that such modes can be present to a significant degree in silica PCFs with $d/\Lambda < 0.40$ that would be considered to be single-mode by index guiding considerations alone. Experimental observations presented here confirm this, demonstrating that these higher-order modes can be visible in metre lengths of fibre with moderate input power (few mW). The fraction of power propagating in these higher-order modes can be effectively minimized by optimizing the coupling conditions for the fundamental mode and also by bending the fibre (with a moderate loss penalty

in the latter case). However, it is important to note that the presence of higher-order modes guided by periodic effects may detrimentally impact the application of standard PCF designs where control over the fibre input is limited and where mode quality is important, such as modal filtering [136].

Chapter 9

Summary and future directions

This thesis targets the design and fabrication of silica hollow-core photonic bandgap fibres free from coupling with surface modes. A detailed numerical study on the impact of the core geometry on the transmission performance of realistic hollow-core fibres designs was carried out. It was found that when defining the core of HC-PBGFs, the choice of the core wall thickness is critical due to its influence on the surface modes. Core surrounds incorporating a thin core wall were proposed as to reduce the impact of surface modes. A modified fabrication technique which allows for the fabrication of these new core designs was developed. These developments resulted in the fabrication of fibres which does not present surface mode crossings over the full spectral width of the photonic bandgap and present state-of-the-art attenuations.

9.1 Summary of results

This research has identified that in order to remove surface modes, one needs to design and fabricate fibers in which the cladding structure terminates as naturally as possible at the core/cladding interface. One way to do this is to form the core by terminating the cladding at the natural edge of a unit cell without the addition or removal of extra glass. Therefore, it has been identified that fibres incorporating a silica core surround of just half the thickness of the thinnest features in the cladding, are able to remove surface modes form the bandgap, improving the performance of the fibre in several ways. Most obviously by eliminating surface modes the range of wavelengths which can be transmitted with low attenuation is increased. As a result of the increased bandwidth, the rate that the properties of the core mode change with wavelength is decreased, so the group velocity dispersion and dispersion slope also decrease.

Firstly, the evolution of surface modes as a function of the core wall thickness of a HC-PBGF with a 7 cell core was numerically studied. Contour plots summarizing the transmission properties of the fibre with the different core surrounds were produced. These contour plots are an original way of analyzing bandgap fibres and clearly show the changes on the density of surface modes and their frequency shift as a function of the design parameter. It was found that for most values of the core wall thickness multiple surface modes appear within the bandgap. However, if the thickness of the core/cladding interface is just half the thickness of the thinnest features in the cladding, then surface modes are eliminated. This design offer the widest operational bandwidth and should therefore be targeted when fabricating fibres for broadband operation. Thin core wall surrounds at the same time reduce the optical overlap with the glass boundaries and therefore the fibre attenuation is also reduced. However, the precise control of the thickness of the core wall is fundamental because if the core wall becomes thinner (thicker) than the optimum value, new surface modes appear close to the low (high) frequency bandgap edge reducing the transmission bandwidth of the fibre. The effects of slightly expanding and compressing the core where studied and it was demonstrated that the suggested thin core wall designs are robust in eliminating surface modes, as variations in the core size affect their operational bandwidth only marginally.

The work on 7-cell core fibres was extend to the case of fibres with a larger 19-cell core, and showed the thin core wall surround design regime is robust and the principles developed for the 7-cell fibres apply here as well. In particular, the density of surface modes is minimized independently if the core is formed by removing the central 7 or 19 cells. Clearly by enlarging the core, the attenuation of the fundamental is reduced; from the numerical computations, it is expected that the 19-cell core fibre should have $\sim$3 times lower optical loss than the 7-cell core fibre over a comparable spectral bandwidth, leading to novel wide bandwidth low-loss fibres. Although different core shapes were not studied, these results suggest that thin core wall designs should reduce the impact of surface modes on the guidance of hollow-core fibres. Possibly, different core shapes could be used to tailor the nonlinearity, dispersion or polarization properties of HC-PBGFs improving the performance of the fibres for particular applications.

The fabrication of thin core wall fibres was then targeted. However, the core walls required are around 100 nm thick, making it difficult to fabricate such structures. In order to overcome the problems on forming such a thin core wall, a modified fabrication process was developed, which allows for the production of low-loss HC-PBGFs a lot quicker than before. Experimental confirmation of the theoretical results has come after characterizing the fabricated thin core wall fibres. Experimental studies indicated that the fibres do not present signs of surface mode crossings and are able to guide light over a broader spectral window and with comparable or lower attenuation than previous

state-of-the-art HC-PBGF. The elimination of surface modes enables low attenuation over the full spectral width of the bandgap - a minimum loss of 15 dB/km and less than 50 dB/km over 300 nm for a fibre operating at 1550 nm has been measured. Also as predicted numerically, the fibres present the lowest dispersion slope yet reported for a HC-PBGF - a factor of almost two reduction compared to the prior state-of-the-art.

In a second part of this thesis, the mode structure of a Kagome fibre was modelled in order to understand why these fibres are able to guide light in a hollow-core. It was shown that although the Kagome structure does not present significant bandgaps crossing the airline, it can be very efficient at confining and guiding light in a hollow-core over a extremely broad spectral range. It has been identified that this is due to a strong isolation of the core guided modes from the cladding modes which inhibits the coupling of energy from the core to the cladding. A key aspect of the guidance in these fibres is the weak modal overlap between core modes and cladding modes due to rapid field spatial oscillations of the cladding modes. Two different types of cladding modes have been identified, the first type concentrates most of its energy in the cladding air regions while the second are in the silica struts. Core modes do not strongly couple to these two kinds of cladding modes either because their large propagation mismatch or their small spatial overlap. However, for certain wavelength ranges hybrid cladding modes, whose energy is extended into both regions, exist. These modes have a large spatial overlap and small propagation constant mismatch with the fundamental core mode (they can have the same propagation constant), enabling the coupling of light from the core to the cladding and thus increasing fibre loss.

Finally, index guiding photonic crystal fibres were studied in order to understand some experimentally observed higher order modes. Although most solid core PCF guide light by a modified form of total internal reflection, it has been demonstrated that higher-order core modes can be guided due to bandgaps of the periodic cladding structure. Numerical calculations presented here show that these additional modes have effective indices below the average cladding index and are located within bandgap regions. Additionally, it is demonstrated that these higher-order core modes can exist even when the cladding does not present a bandgap. In this case, the modes lie in regions with low density of optical states in the cladding. Remarkably, such modes can be present in silica PCFs with $d/\Lambda < 0.4$ that would be considered to be single-mode by index guiding considerations alone. Excellent agreement between theoretical predictions and experimental observations is demonstrated.

9.2 Future work

Further improvements to the fibre fabrication technique presented in this thesis will certainly be required for realizing fibres with lower attenuation. Improved fibres are also envisioned by further optimization of the cladding and core designs. Fabricating 19-cell HC-PBGFs free of surface modes would greatly extend the useable bandwidth compared to previous 19-cell fibre designs. The transmission spectra of previously-reported low-loss 19-cell fibres have been completely dominated by surface mode crossings, and so it can be anticipated that the larger core size and greatly reduced dispersion slope in the new fibres would enable a new regime of ultrashort-pulse solitons and high-power beam delivery.

Hollow-core photonic bandgap have unique transmission properties that make them ideal for a range of applications such as delivery of ultrashort pulses, soliton pulse delivery, and re-compression of pulses in chirped pulse amplification laser systems. The ability of fabricating fibres with tailored nonlinear response and dispersion properties will definitely have a great impact on all these areas. Although a numerical investigation of ways of modifying the dispersion properties of HC-PBGFs has been presented in this thesis, more detailed studies analyzing fibres with different core shapes will be carried out in the near future.

Appendix A

Sellmeier Dispersion Formula

The refractive index of optical materials can be accurately fitted by the Sellmeier formula, which is given by

$$n^2 = 1 + \sum_j \frac{A_j \lambda^2}{\lambda^2 - {\lambda_j}^2} \tag{A.1}$$

where n is the real part of the refractive index, and wavelengths of maximum absorption are denoted by λ_j. The refractive index of silica glass is normally fitted to the three-term Sellmeier equation [8]

$$n^2 - 1 = \frac{A_1 \lambda^2}{\lambda^2 - {\lambda_1}^2} + \frac{A_2 \lambda^2}{\lambda^2 - {\lambda_2}^2} + \frac{A_3 \lambda^2}{\lambda^2 - {\lambda_3}^2} \tag{A.2}$$

for bulk fused silica these parameters are:

$A_1 = 0.6961663$,

$A_2 = 0.4079426$,

$A_3 = 0.8974794$,

$\lambda_1 = 0.0684043$ μm,

$\lambda_2 = 0.1162414$ μm,

$\lambda_3 = 9.896161$ μm.

Appendix B

List of Publications

Journal Publications

1. **The effect of periodicity on the defect modes of large mode area microstructured fibres.**
   Joanne C. Flanagan, R. Amezcua-Correa, F. Poletti, J.R. Hayes, N.G.R. Broderick and D. J. Richardson, **16**, 18631, (2008).

2. **Control of surface modes in low loss hollow-core photonic bandgap fibers.**
   R. Amezcua-Correa, F. Gerome, S. G. Leon-Saval, N. G. Broderick, T. A. Birks and J. C. Knight, *Optics Express*, **16**, 1142, (2008).

3. **Optimizing the usable bandwidth and loss through core design in realistic hollow-core photonic bandgap fibers.**
   R. Amezcua-Correa, N. G. Broderick, M. N. Petrovich, F. Poletti and D. J. Richardson, *Optics Express*, **14**, 7974, (2006).

4. **Design of 7 and 19 cells core air-guiding photonic crystal fibers for low-loss, wide bandwidth and dispersion controlled operation.**
   R. Amezcua-Correa, N. G. Broderick, M. N. Petrovich, F. Poletti and D. J. Richardson, *Optics Express*, **15**, 17577, (2007).

Conference Publications

1. **Comparison of mode properties of 7 and 19 cells core hollow-core photonic crystal fibers.**
   R. Amezcua-Correa, N. G. R. Broderick, M. N. Petrovich and D. J. Richardson, in *OFC*, Anaheim, 2007.

2. **Parasitic modes in large mode area microstructured fibers.**
   J.C. Flanagan, R. Amezcua-Correa, F. Poletti, J.R. Hayes, N.G.R. Broderick and D.J. Richardson, in *OFC*, Anaheim, 2007.

3. **Possible future applications of photonic bandgap fiber in non-repeatered transmission.**
   K. Mukasa, F. Poletti, M.N. Petrovich, N.G.R. Broderick, R. Amezcua-Correa, M.A.F. Roelens and D.J. Richardson, in *OFC*, Anaheim, 2007.

4. **Future opportunities for photonic bandgap fibers (PBGFs) in DWDM transmission.**
   K. Mukasa, M.N. Petrovich, F. Poletti, N.G.R. Broderick, R. Amezcua-Correa, M.A.F. Roelens, K. Imamura, T. Yagi and D.J. Richardson, in *OFC*, Anaheim, 2007.

5. **Photonic band gap fibres: The new way of guiding light.**
   R. Amezcua-Correa, N.G.R. Broderick, M.N. Petrovich and D.J. Richardson, in *SET for Britain*, London, 2006.

6. **Modelling applications of photonic bandgap fibres.**
   N.G.R. Broderick, R. Amezcua-Correa, F. Poletti, J.C. Flanagan, M.N. Petrovich and D.J. Richardson, in *Photonics 2006*, Hyderabad, 2006, Invited Paper.

7. **Designing hollow-core photonic bandgap fibres free of surface modes.**
   R. Amezcua-Correa, N.G.R. Broderick, M.N. Petrovich and D.J. Richardson, in *Rank Prize Funds: Metamaterials in Nature and technology*, Lake Windermere, 2006.

8. **Broadband infrared transmission in a hollow-core photonic bandgap fibre free of surface modes.**
   R. Amezcua-Correa, M.N. Petrovich, N.G. Broderick, D.J. Richardson, T. Delmonte, M.A. Watson and E.J. O'Driscoll, in *ECOC*, Cannes, 2006.

9. **Realistic designs of silica hollow-core photonic bandgap fibers free of surface modes.**
   R. Amezcua-Correa, N.G. Broderick, M.N. Petrovich, F. Poletti, D.J. Richardson, V. Finazzi and T.M. Monro, in *OFC*, Anaheim, 2006.

10. **Advances and limitations in the modelling of fabricated photonic bandgap fibers.**
    F. Poletti, M.N. Petrovich, R. Amezcua-Correa, N.G. Broderick, T.M. Monro and D.J. Richardson, in *OFC*, Anaheim, 2006.

11. **Applications of microstructured fibre technology in aerospace and defence.**
    E.J.O'Driscoll, T. Delmonte, M.A. Watson, M.N. Petrovich, R. Amezcua-Correa, F. Poletti and D.J. Richardson, in *EMRS-DTC Technical Conference*, Edinburgh, 2006.

12. **Photonic bandgap fibres for broadband transmission of SWIR wavelengths.**
    M.N. Petrovich. R. Amezcua-Correa, N.G. Broderick, D.J. Richardson, T. Delmonte, M.A. Watson and E.J.O'Driscoll, in *EMRS-DTC Technical Conference*, Edinburgh, 2006.

13. **Novel fabrication method of highly-nonlinear silica holey fibres.**
    K. Mukasa, M.N. Petrovich, F. Poletti, A. Webb, J. Hayes, A. van Brakel, R. Amezcua-Correa, L. Provost, J.K. Sahu, P. Petropoulos and D.J. Richardson, in *CLEO/QELS*, Long Beach, 2006.

Bibliography

[1] P. Russell. Photonic crystal fibers. *Science*, 299(5605):358–362, 2003.

[2] P. S. J. Russell. Photonic-crystal fibers. *Journal of Lightwave Technology*, 24(12):4729–4749, 2006.

[3] P. Kaiser, E. A. J. Marcatili, and S.E. Miller. A new optical fiber. *Bell Systems Technical Journal*, 52(2):265–269, 1973.

[4] P. Kaiser and H. W. Astle. Low-loss single material fibers made from pure fused silica. *Bell Systems Technical Journal*, 53:1021–1039, 1974.

[5] J. B. MacChesney, P. B. O'Connor, and H. M. Presby. A new technique for preparation of low-loss and graded index optical fibers. *Proceedings of the IEEE*, 62:1278–1279, 1974.

[6] W. G. French, J. B. Macchesney, and A. D. Pearson. Glass fibers for optical communications. *Annual Review of Materials Science*, 5:373–394, 1975.

[7] W. Hermann and D. U. Wiechert. Refractive-index of doped and undoped pcvd bulk silica. *Materials Research Bulletin*, 24(9):1083–1097, 1989.

[8] G. P. Agrawal. *Nonlinear fiber optics*. Academic Press, San Diego, 3rd edition, 2001.

[9] S. R. Nagel, J. B. Macchesney, and K. L. Walker. An overview of the modified chemical vapor-deposition (MCVD) process and performance. *IEEE Journal of Quantum Electronics*, 18(4):459–476, 1982.

[10] T. A. Birks, P. J. Roberts, P. S. J. Russell, D. M. Atkin, and T. J. Shepherd. Full 2-D photonic bandgaps in silica/air structures. *Electronics Letters*, 31(22):1941–1943, 1995.

[11] J. C. Knight. Photonic crystal fibres. *Nature*, 424(6950):847–851, 2003.

[12] J. C. Knight, T. A. Birks, P. S. Russell, and D. M. Atkin. All-silica single-mode optical fiber with photonic crystal cladding. *Optics Letters*, 21(19):1547–1549, 1996.

[13] T. A. Birks, J. C. Knight, and P. S. Russell. Endlessly single-mode photonic crystal fiber. *Optics Letters*, 22(13):961–963, 1997.

[14] R. F. Cregan, B. J. Mangan, J. C. Knight, T. A. Birks, P. S. Russell, P. J. Roberts, and D. C. Allan. Single-mode photonic band gap guidance of light in air. *Science*, 285(5433):1537–1539, 1999.

[15] B.J. Mangan, L. Farr, A. Langford, P.J. Roberts, D.P. Williams, F. Couny, M. Lawman, M. Mason, S. Coupland, R. Flea, H. Sabert, T.A. Birks, J.C. Knight, and P.St.J. Russell. Low loss (1.7 db/km) hollow core photonic bandgap fiber. *Optical Fiber Communication Conference, 2004. OFC 2004*, 2:3 pp. vol.2–, Feb. 2004.

[16] R. Amezcua-Correa, F. Gerome, S. G. Leon-Saval, N. G. R. Broderick, T. A. Birks, and J. C. Knight. Control of surface modes in low loss hollow-core photonic bandgap fibers. *Optics Express*, 16(2):1142–1149, 2008.

[17] J. K. Ranka, R. S. Windeler, and A. J. Stentz. Visible continuum generation in air-silica microstructure optical fibers with anomalous dispersion at 800 nm. *Optics Letters*, 25(1):25–27, 2000.

[18] M. D. Nielsen and N. A. Mortensen. Photonic crystal fiber design based on the V-parameter. *Optics Express*, 11(21):2762–2768, 2003.

[19] D. Mogilevtsev, T. A. Birks, and P. S. Russell. Group-velocity dispersion in photonic crystal fibers. *Optics Letters*, 23(21):1662–1664, 1998.

[20] N. G. R. Broderick, T. M. Monro, P. J. Bennett, and D. J. Richardson. Nonlinearity in holey optical fibers: measurement and future opportunities. *Optics Letters*, 24(20):1395–1397, 1999.

[21] J. C. Knight, J. Arriaga, T. A. Birks, A. Ortigosa-Blanch, W. J. Wadsworth, and P. S. Russell. Anomalous dispersion in photonic crystal fiber. *IEEE Photonics Technology Letters*, 12(7):807–809, 2000.

[22] A. Ferrando, E. Silvestre, J. J. Miret, and P. Andres. Nearly zero ultraflattened dispersion in photonic crystal fibers. *Optics Letters*, 25(11):790–792, 2000.

[23] W. H. Reeves, D. V. Skryabin, F. Biancalana, J. C. Knight, P. S. Russell, F. G. Omenetto, A. Efimov, and A. J. Taylor. Transformation and control of ultra-short pulses in dispersion-engineered photonic crystal fibres. *Nature*, 424(6948):511–515, 2003.

[24] K. Nagayama, M. Kakui, M. Matsui, I. Saitoh, and Y. Chigusa. Ultra-low-loss (0.1484 db/km) pure silics core fibre and extension of transmission distance. *Electronics Letters*, 38(4):1168–1169, 2002.

[25] J. C. Knight, J. Broeng, T. A. Birks, and P. S. J. Russel. Photonic band cap guidance in optical fibers. *Science*, 282(5393):1476–1478, 1998.

[26] S. M. Sze. *Semiconductor devices, physics and technology.* Wiley, New York, 2nd edition, 2002.

[27] C. Kittel. *Introduction to solid state physics.* Wiley, New York, 7th edition, 1996.

[28] E. Yablonovitch. Inhibited spontaneous emission in solid-state physics and electronics. *Physical Review Letters*, 58(20):2059–2062, 1987.

[29] S. John. Strong localization of photons in certain disordered dielectric superlattices. *Physical Review Letters*, 58(23):2486–2489, 1987.

[30] S. John. Electromagnetic absorption in a disordered medium near a photon mobility edge. *Physical Review Letters*, 53(22):2169–2172, 1984.

[31] O. Painter, R. K. Lee, A. Scherer, A. Yariv, J. D. O'Brien, P. D. Dapkus, and I. Kim. Two-dimensional photonic band-gap defect mode laser. *Science*, 284(5421):1819–1821, 1999.

[32] J. D. Joannopoulos, Robert D. Meade, and Joshua N. Winn. *Photonic crystals : molding the flow of light.* Princeton University Press, Princeton, N.J., 1995.

[33] H. P. Myers. *Introductory solid state physics.* Taylor and Francis, London, 2nd edition, 1997.

[34] R.T. Bise and D.J. Trevor. Sol-gel derived microstructured fiber: fabrication and characterization. *Optical Fiber Communication Conference, 2005. Technical Digest. OFC/NFOEC*, 3:3 pp. Vol. 3–, March 2005.

[35] K Mukasa, M. N. Petrovich, F. Poletti, A. Webb, J. Hayes, A. van Brakel, R. Amezcua-Correa, L. Provost, J.K. Sahu, P. Petropoulos, and D.J. Richardson. Novel fabrication method of highly-nonlinear silica holey fibres. *Lasers and Electro-Optics, 2006. (CLEO). Conference on*, May 2006.

[36] X. Feng, T.M. Monro, V. Finazzi, R.C. Moore, K. Frampton, P. Petropoulos, and D.J. Richardson. Extruded singlemode, high-nonlinearity, tellurite glass holey fibre. *Electronics Letters*, 41(15):835–837, July 2005.

[37] B. Temelkuran, S. D. Hart, G. Benoit, J. D. Joannopoulos, and Y. Fink. Wavelength-scalable hollow optical fibres with large photonic bandgaps for CO_2 laser transmission. *Nature*, 420(6916):650–653, 2002.

[38] S. K. Varshney, M. P. Singh, and R. K. Sinha. Propagation characteristics of photonic crystal fibers. *Journal of Optical Communications*, 24, 2002.

[39] Allan W. Snyder and John D. Love. *Optical waveguide theory.* Chapman and Hall, London ; New York, 1983.

[40] J. C. Knight, T. A. Birks, R. F. Cregan, P. S. Russell, and J. P. de Sandro. Large mode area photonic crystal fibre. *Electronics Letters*, 34(13):1347–1348, 1998.

[41] W. J. Wadsworth, R. M. Percival, G. Bouwmans, J. C. Knight, and P. S. J. Russel. High power air-clad photonic crystal fibre laser. *Optics Express*, 11(1):48–53, 2003.

[42] J. Limpert, T. Schreiber, S. Nolte, H. Zellmer, A. Tunnermann, R. Iliew, F. Lederer, J. Broeng, G. Vienne, A. Petersson, and C. Jakobsen. High-power air-clad large-mode-area photonic crystal fiber laser. *Optics Express*, 11(7):818–823, 2003.

[43] W. H. Reeves, J. C. Knight, P. S. J. Russell, and P. J. Roberts. Demonstration of ultra-flattened dispersion in photonic crystal fibers. *Optics Express*, 10(14):609–613, 2002.

[44] Z. Yusoff, J. H. Lee, W. Belardi, T. M. Monro, P. C. Teh, and D. J. Richardson. Raman effects in a highly nonlinear holey fiber: amplification and modulation. *Optics Letters*, 27(6):424–426, 2002.

[45] J. E. Sharping, M. Fiorentino, P. Kumar, and R. S. Windeler. All-optical switching based on cross-phase modulation in microstructure fiber. *IEEE Photonics Technology Letters*, 14(1):77–79, 2002.

[46] P. Petropoulos, T. M. Monro, W. Belardi, K. Furusawa, J. H. Lee, and D. J. Richardson. 2R-regenerative all-optical switch based on a highly nonlinear holey fiber. *Optics Letters*, 26(16):1233–1235, 2001.

[47] J. E. Sharping, M. Fiorentino, P. Kumar, and R. S. Windeler. Optical parametric oscillator based on four-wave mixing in microstructure fiber. *Optics Letters*, 27(19):1675–1677, 2002.

[48] X. Liu, C. Xu, W. H. Knox, J. K. Chandalia, B. J. Eggleton, S. G. Kosinski, and R. S. Windeler. Soliton self-frequency shift in a short tapered air-silica microstructure fiber. *Optics Letters*, 26(6):358–360, 2001.

[49] M. Fiorentino, J. E. Sharping, P. Kumar, A. Porzio, and R. S. Windeler. Soliton squeezing in microstructure fiber. *Optics Letters*, 27(8):649–651, 2002.

[50] J. Herrmann, U. Griebner, N. Zhavoronkov, A. Husakou, D. Nickel, J. C. Knight, W. J. Wadsworth, P. S. J. Russell, and G. Korn. Experimental evidence for supercontinuum generation by fission of higher-order solitons in photonic fibers. *Physical Review Letters*, 88(17):173901, 2002.

[51] A. V. Husakou and J. Herrmann. Supercontinuum generation of higher-order solitons by fission in photonic crystal fibers. *Physical Review Letters*, 8720(20):203901, 2001.

[52] W. J. Wadsworth, A. Ortigosa-Blanch, J. C. Knight, T. A. Birks, T. P. M. Man, and P. S. Russell. Supercontinuum generation in photonic crystal fibers and optical fiber tapers: a novel light source. *Journal of the Optical Society of America B-Optical Physics*, 19(9):2148–2155, 2002.

[53] S. Coen, A. H. L. Chan, R. Leonhardt, J. D. Harvey, J. C. Knight, W. J. Wadsworth, and P. S. J. Russell. White-light supercontinuum generation with 60-ps pump pulses in a photonic crystal fiber. *Optics Letters*, 26(17):1356–1358, 2001.

[54] J. M. Dudley, G. Genty, and S. Coen. Supercontinuum generation in photonic crystal fiber. *Reviews of Modern Physics*, 78(4):1135–1184, 2006.

[55] P. Yeh, A. Yariv, and E. Marom. Theory of Bragg fiber. *Journal of the Optical Society of America*, 68(9):1196–1201, 1978.

[56] F. Brechet, P. Roy, J. Marcou, and D. Pagnoux. Singlemode propagation into depressed-core-index photonic-bandgap fibre designed for zero-dispersion propagation at short wavelengths. *Electronics Letters*, 36(6):514–515, 2000.

[57] M. Ibanescu, Y. Fink, S. Fan, E. L. Thomas, and J. D. Joannopoulos. An all-dielectric coaxial waveguide. *Science*, 289(5478):415–419, 2000.

[58] K. Kuriki, O. Shapira, S. D. Hart, G. Benoit, Y. Kuriki, J. F. Viens, M. Bayindir, J. D. Joannopoulos, and Y. Fink. Hollow multilayer photonic bandgap fibers for NIR applications. *Optics Express*, 12(8):1510–1517, 2004.

[59] Y. Fink, J. N. Winn, S. H. Fan, C. P. Chen, J. Michel, J. D. Joannopoulos, and E. L. Thomas. A dielectric omnidirectional reflector. *Science*, 282(5394):1679–1682, 1998.

[60] G. Vienne, Y. Xu, C. Jakobsen, H.J. Deyerl, T.P. Hansen, B.H. Larsen, J.B. Jensen, T. Sorensen, M. Terrel, Y. Huang, R. Lee, N.A. Mortensen, J. Broeng, H. Simonsen, A. Bjarklev, and A. Yariv. First demonstration of air-silica bragg fiber. *Optical Fiber Communication Conference, 2004. OFC 2004*, 2, Feb. 2004.

[61] G. J. Pearce, G. S. Wiederhecker, C. G. Poulton, S. Burger, and P. S. J. Russell. Models for guidance in kagome-structured hollow-core photonic crystal fibres. *Optics Express*, 15(20):12680–12685, 2007.

[62] F. Couny, F. Benabid, P. J. Roberts, M. T. Burnett, and S. A. Maier. Identification of bloch-modes in hollow-core photonic crystal fiber cladding. *Optics Express*, 15(2):325–338, 2007.

[63] F. Couny, F. Benabid, and P. S. Light. Large-pitch kagome-structured hollow-core photonic crystal fiber. *Optics Letters*, 31(24):3574–3576, 2006.

[64] D. G. Ouzounov, F. R. Ahmad, D. Muller, N. Venkataraman, M. T. Gallagher, M. G. Thomas, J. Silcox, K. W. Koch, and A. L. Gaeta. Generation of megawatt optical solitons in hollow-core photonic band-gap fibers. *Science*, 301(5640):1702–1704, 2003.

[65] F. Luan, J. C. Knight, P. S. Russell, S. Campbell, D. Xiao, D. T. Reid, B. J. Mangan, D. P. Williams, and P. J. Roberts. Femtosecond soliton pulse delivery at 800nm wavelength in hollow-core photonic bandgap fibers. *Optics Express*, 12(5):835–840, 2004.

[66] D. G. Ouzounov, C. J. Hensley, A. L. Gaeta, N. Venkateraman, M. T. Gallagher, and K. W. Koch. Soliton pulse compression in photonic band-gap fibers. *Optics Express*, 13(16):6153–6159, 2005.

[67] F. Gerome, K. Cook, A. K. George, W. J. Wadsworth, and J. C. Knight. Delivery of sub-100fs pulses through 8m of hollow-core fiber using soliton compression. *Optics Express*, 15(12):7126–7131, 2007.

[68] J. D. Shephard, J. D. C. Jones, D. P. Hand, G. Bouwmans, J. C. Knight, P. S. Russell, and B. J. Mangan. High energy nanosecond laser pulses delivered single-mode through hollow-core pbg fibers. *Optics Express*, 12(4):717–723, 2004.

[69] A. M. Cubillas, M. Silva-Lopez, J. M. Lazaro, O. M. Conde, M. N. Petrovich, and J. M. Lopez-Higuera. Methane detection at 1670-nm band using a hollow-core photonic bandgap fiber and a multiline algorithm. *Optics Express*, 15(26):17570–17576, 2007.

[70] F. Benabid, J. C. Knight, G. Antonopoulos, and P. S. J. Russell. Stimulated Raman scattering in hydrogen-filled hollow-core photonic crystal fiber. *Science*, 298(5592):399–402, 2002.

[71] F. Benabid, F. Couny, J. C. Knight, T. A. Birks, and P. S. Russell. Compact, stable and efficient all-fibre gas cells using hollow-core photonic crystal fibres. *Nature*, 434(7032):488–491, 2005.

[72] F. Benabid, G. Antonopoulos, J. C. Knight, and P. S. Russell. Stokes amplification regimes in quasi-cw pumped hydrogen-filled hollow-core photonic crystal fiber. *Physical Review Letters*, 95(21), 2005.

[73] S. Ghosh, A. R. Bhagwat, C. K. Renshaw, S. Goh, A. L. Gaeta, and B. J. Kirby. Low-light-level optical interactions with rubidium vapor in a photonic band-gap fiber. *Physical Review Letters*, 97(2):–, 2006.

[74] S. Ghosh, J. E. Sharping, D. G. Ouzounov, and A. L. Gaeta. Resonant optical interactions with molecules confined in photonic band-gap fibers. *Physical Review Letters*, 94(9):–, 2005.

[75] C. M. Smith, N. Venkataraman, M. T. Gallagher, D. Muller, J. A. West, N. F. Borrelli, D. C. Allan, and K. W. Koch. Low-loss hollow-core silica/air photonic bandgap fibre. *Nature*, 424(6949):657–659, 2003.

[76] J. A. West, C. M. Smith, N. F. Borrelli, D. C. Allan, and K. W. Koch. Surface modes in air-core photonic band-gap fibers. *Optics Express*, 12(8):1485–1496, 2004.

[77] K. Saitoh, N. A. Mortensen, and M. Koshiba. Air-core photonic band-gap fibers: the impact of surface modes. *Optics Express*, 12(3):394–400, 2004.

[78] P.J. Roberts, F. Couny, T.A. Birks, J.C. Knight, P.J. St Russell, B.J. Mangan, H. Sabert, D.P. Williams, and L. Farr. Achieving low loss and low nonlinearity in hollow core photonic crystal fibers. *Lasers and Electro-Optics, 2005. (CLEO). Conference on*, 2:1240–1242 Vol. 2, May 2005.

[79] P. J. Roberts, F. Couny, H. Sabert, B. J. Mangan, D. P. Williams, L. Farr, M. W. Mason, A. Tomlinson, T. A. Birks, J. C. Knight, and P. S. J. Russell. Ultimate low loss of hollow-core photonic crystal fibres. *Optics Express*, 13(1):236–244, 2005.

[80] P. J. Roberts, D. P. Williams, B. J. Mangan, H. Sabert, F. Couny, W. J. Wadsworth, T. A. Birks, J. C. Knight, and P. S. J. Russell. Realizing low loss air core photonic crystal fibers by exploiting an antiresonant core surround. *Optics Express*, 13(20):8277–8285, 2005.

[81] P. J. Roberts, F. Couny, H. Sabert, B. J. Mangan, T. A. Birks, J. C. Knight, and P. S. Russell. Loss in solid-core photonic crystal fibers due to interface roughness scattering. *Optics Express*, 13(20):7779–7793, 2005.

[82] J. M. Pottage, D. M. Bird, T. D. Hedley, T. A. Birks, J. C. Knight, P. S. Russell, and P. J. Roberts. Robust photonic band gaps for hollow core guidance in pcf made from high index glass. *Optics Express*, 11(22):2854–2861, 2003.

[83] N. A. Mortensen and M. D. Nielsen. Modeling of realistic cladding structures for air-core photonic bandgap fibers. *Optics Letters*, 29(4):349–351, 2004.

[84] http://www.crystal-fibre.com/.

[85] M. Yan, P. Shum, and J. Hu. Design of air-guiding honeycomb photonic bandgap fiber. *Optics Letters*, 30(5):465–467, 2005.

[86] M. Yan and P. Shum. Air guiding with honeycomb photonic bandgap fiber. *IEEE Photonics Technology Letters*, 17(1):64–66, 2005.

[87] M. Y. Chen and R. J. Yu. Analysis of photonic bandgaps in modified honeycomb structures. *IEEE Photonics Technology Letters*, 16(3):819–821, 2004.

[88] L. Vincetti, F. Poli, and S. Selleri. Confinement loss and nonlinearity analysis of air-guiding modified honeycomb photonic bandgap fibers. *IEEE Photonics Technology Letters*, 18(1-4):508–510, 2006.

[89] M. Y. Chen and R. J. Yu. Square-structured photonic bandgap fibers. *Optics Communications*, 235(1-3):63–67, 2004.

[90] F. Poletti and D. J. Richardson. Hollow-core photonic bandgap fibers based on a square lattice cladding. *Optics Letters*, 32(16):2282–2284, 2007.

[91] Steven G. Johnson and J. D. Joannopoulos. Block-iterative frequency-domain methods for Maxwell's equations in a planewave basis. *Optics Express*, 8(3):173–190, 2001.

[92] A. Bjarklev, J. Broeng, S. Barkou, and A. S. Bjarklev. *Photonic Crystals Fibres*. Klumeer Academic Publishers, Boston, MA., 2003.

[93] F. Zolla, G. Renversez, A. Nicolet, B. Kuhlmey, S. Guenneau, and D. Felbacq. *Foundations of Photonic Crystals Fibres*. Imperial College Press, London, UK., 2005.

[94] Z. Zhang and S. Satpathy. Electromagnetic-wave propagation in periodic structures - bloch wave solution of maxwell equations. *Physical Review Letters*, 65(21):2650–2653, 1999.

[95] K. M. Ho, C. T. Chan, and C. M. Soukoulis. Existence of a photonic gap in periodic dielectric structures. *Physical Review Letters*, 65(25):3152–3155, 1990.

[96] A. A. Maradudin and A. R. Mcgurn. Out-of-plane propagation of electromagnetic-waves in a 2-dimensional periodic dielectric medium. *Journal of Modern Optics*, 41(2):275–284, 1994.

[97] P. R. Villeneuve and M. Piche. Photonic band-gaps in 2-dimensional square and hexagonal lattices. *Physical Review B*, 46(8):4969–4972, 1992.

[98] J. B. Pendry. Photonic band structures. *Journal of Modern Optics*, 41(2):209–229, 1994.

[99] R. D. Meade, A. M. Rappe, K. D. Brommer, J. D. Joannopoulos, and O. L. Alerhand. Accurate theoretical-analysis of photonic band-gap materials. *Physical Review B*, 48(11):8434–8437, 1993.

[100] G. J. Pearce, T. D. Hedley, and D. M. Bird. Adaptive curvilinear coordinates in a plane-wave solution of Maxwell's equations in photonic crystals. *Physical Review B*, 71(19):–, 2005.

[101] J. Broeng, S. E. Barkou, T. Sondergaard, and A. Bjarklev. Analysis of air-guiding photonic bandgap fibers. *Optics Letters*, 25(2):96–98, 2000.

[102] M. J. Steel, T. P. White, C. M. de Sterke, R. C. McPhedran, and L. C. Botten. Symmetry and degeneracy in microstructured optical fibers. *Optics Letters*, 26(8):488–490, 2001.

[103] J. Jin. *The finite element method in electromagnetics*. John Wiley & Sons, New York, 2002.

[104] http://www.comsol.com/.

[105] P. R. Mcisaac. Symmetry-induced modal characteristics of uniform waveguides .1. summary of results. *IEEE Transactions on Microwave Theory and Techniques*, Mt23(5):421–429, 1975.

[106] P. R. Mcisaac. Symmetry-induced modal characteristics of uniform waveguides .2. theory. *IEEE Transactions on Microwave Theory and Techniques*, Mt23(5):429–433, 1975.

[107] T. P. White, B. T. Kuhlmey, R. C. McPhedran, D. Maystre, G. Renversez, C. M. de Sterke, and L. C. Botten. Multipole method for microstructured optical fibers. I. Formulation. *Journal of the Optical Society of America B-Optical Physics*, 19(10):2322–2330, 2002.

[108] Ren Guobin, Wang Zhi, Lou Shuqin, and Jian Shuisheng. Mode classification and degeneracy in photonic crystal fibers. *Optics Express*, 11(11):1310–1321, 2003.

[109] K. Saitoh and M. Koshiba. Leakage loss and group velocity dispersion in air-core photonic bandgap fibers. *Optics Express*, 11(23):3100–3109, 2003.

[110] K. Saitoh, M. Koshiba, T. Hasegawa, and E. Sasaoka. Chromatic dispersion control in photonic crystal fibers: application to ultra-flattened dispersion. *Optics Express*, 11(8), 2003.

[111] J. P. Berenger. A perfectly matched layer for the absorption of electromagnetic-waves. *Journal of Computational Physics*, 114(2):185–200, 1994.

[112] Z. S. Sacks, D. M. Kingsland, R. Lee, and J. F. Lee. A perfectly matched anisotropic absorber for use as an absorbing boundary condition. *IEEE Transactions on Antennas and Propagation*, 43(12):1460–1463, 1995.

[113] A. Cucinotta, G. Pelosi, S. Selleri, L. Vincetti, and M. Zoboli. Perfectly matched anisotropic layers for optical waveguide analysis through the finite-element beam-propagation method. *Microwave and Optical Technology Letters*, 23(2):67–69, 1999.

[114] K. Saitoh and M. Koshiba. Full-vectorial finite element beam propagation method with perfectly matched layers for anisotropic optical waveguides. *Journal of Lightwave Technology*, 19(3):405–413, 2001.

[115] J. Limpert, T. Schreiber, S. Nolte, H. Zellmer, and A. Tunnermann. All fiber chirped-pulse amplification system based on compression in air-guiding photonic bandgap fiber. *Optics Express*, 11(24):3332–3337, 2003.

[116] B. Kibler, C. Billet, P. A. Lacourt, R. Ferriere, and J. M. Dudley. All-fiber source of 20-fs pulses at 1550 nm using two-stage linear-nonlinear compression of parabolic similaritons. *IEEE Photonics Technology Letters*, 18(17-20):1831–1833, 2006.

[117] H. K. Kim, M. J. F. Digonnet, G. S. Kino, J. W. Shin, and S. H. Fan. Simulations of the effect of the core ring on surface and air-core modes in photonic bandgap fibers. *Optics Express*, 12(15):3436–3442, 2004.

[118] H. K. Kim, J. Shin, S. H. Fan, M. J. F. Digonnet, and G. S. Kino. Designing air-core photonic-bandgap fibers free of surface modes. *IEEE Journal of Quantum Electronics*, 40(5):551–556, 2004.

[119] M. J. F. Digonnet, H. K. Kim, J. Shin, S. H. Fan, and G. S. Kino. Simple geometric criterion to predict the existence of surface modes in air-core photonic-bandgap fibers. *Optics Express*, 12(9):1864–1872, 2004.

[120] F. Poletti, N. G. R. Broderick, D. J. Richardson, and T. M. Monro. The effect of core asymmetries on the polarization properties of hollow core photonic band gap fibers. *Optics Express*, 13(22):9115–9124, 2005.

[121] R. Amezcua-Correa, N. G. R. Broderick, M. N. Petrovich, F. Poletti, and D. J. Richardson. Optimizing the usable bandwidth and loss through core design in realistic hollow-core photonic bandgap fibers. *Optics Express*, 14(17):7974–7985, 2006.

[122] R. Amezcua-Correa, N. G. R. Broderick, M. N. Petrovich, F. Poletti, and D. J. Richardson. Design of 7 and 19 cells core air-guiding photonic crystal fibers for low-loss, wide bandwidth and dispersion controlled operation. *Optics Express*, 15(26):17577–17586, 2007.

[123] G. J. Pearce, J. M. Pottage, D. M. Bird, P. J. Roberts, J. C. Knight, and P. S. J. Russell. Hollow-core PCF for guidance in the mid to far infra-red. *Optics Express*, 13(18):6937–6946, 2005.

[124] T. D. Engeness, M. Ibanescu, S. G. Johnson, O. Weisberg, M. Skorobogatiy, S. Jacobs, and Y. Fink. Dispersion tailoring and compensation by modal interactions in omniguide fibers. *Optics Express*, 11(10):1175–1196, 2003.

[125] P. J. Roberts, D. P. Williams, H. Sabert, B. J. Mangan, D. M. Bird, T. A. Birks, J. C. Knight, and P. S. Russell. Design of low-loss and highly birefringent hollow-core photonic crystal fiber. *Optics Express*, 14(16):7329–7341, 2006.

[126] C. J. S. de Matos, J. R. Taylor, T. P. Hansen, K. P. Hansen, and J. Broeng. All-fiber chirped pulse amplification using highly-dispersive air-core photonic bandgap fiber. *Optics Express*, 11(22):2832–2837, 2003.

[127] C. J. S. de Matos, S. V. Popov, A. B. Rulkov, J. R. Taylor, J. Broeng, T. P. Hansen, and V. P. Gapontsev. All-fiber format compression of frequency chirped pulses in air-guiding photonic crystal fibers. *Physical Review Letters*, 93(10):–, 2004.

[128] F. Gerome, P. Dupriez, J. Clowes, J. C. Knight, and W. J. Wadsworth. High power tunable femtosecond soliton source using hollow-core photonic bandgap fiber, and its use for frequency doubling. *Optics Express*, 16(4):2381–2386, 2008.

[129] N. M. Litchinitser, A. K. Abeeluck, C. Headley, and B. J. Eggleton. Antiresonant reflecting photonic crystal optical waveguides. *Optics Letters*, 27(18):1592–1594, 2002.

[130] N. M. Litchinitser, S. C. Dunn, B. Usner, B. J. Eggleton, T. P. White, R. C. McPhedran, and C. M. de Sterke. Resonances in microstructured optical waveguides. *Optics Express*, 11(10):1243–1251, 2003.

[131] T. P. White, R. C. McPhedran, C. M. de Sterke, N. M. Litchinitser, and B. J. Eggleton. Resonance and scattering in microstructured optical fibers. *Optics Letters*, 27(22):1977–1979, 2002.

[132] C. J. Hensley, D. G. Ouzounov, A. L. Gaeta, N. Venkataraman, M. T. Gallagher, and K. W. Koch. Silica-glass contribution to the effective nonlinearity of hollow-core photonic band-gap fibers. *Optics Express*, 15(6):3507–3512, 2007.

[133] F. Couny, F. Benabid, P. J. Roberts, P. S. Light, and M. G. Raymer. Generation and photonic guidance of multi-octave optical-frequency combs. *Science*, 318(5853):1118–1121, 2007.

[134] A. Argyros and J. Pla. Hollow-core polymer fibres with a Kagome lattice: potential for transmission in the infrared. *Optics Express*, 15(12):7713–7719, 2007.

[135] T.D. Hedley, D.M. Bird, F. Benabid, J.C. Knight, and P.St.J. Russell. Modelling of a novel hollow-core photonic crystal fibre. *Quantum Electronics and Laser Science, 2003. QELS. Postconference Digest*, pages 2 pp.–, June 2003.

[136] J. C. Flanagan, D. J. Richardson, M. J. Foster, and I. Bakalski. Microstructured fibers for broadband wavefront filtering in the mid-IR. *Optics Express*, 14(24):11773–11786, 2006.

[137] K. Nakajima, J. Zhou, K. Tajima, K. Kurokawa, C. Fukai, and I. Sankawa. Ultrawide-band single-mode transmission performance in a low-loss photonic crystal fiber. *Journal of Lightwave Technology*, 23(1):7–12, 2005.

[138] J. C. W. Corbett and J. R. Allington-Smith. Coupling starlight into single-mode photonic crystal fiber using a field lens. *Optics Express*, 13(17):6527–6540, 2005.

[139] J. C. Baggett, T. M. Monro, K. Furusawa, V. Finazzi, and D. J. Richardson. Mode area limits in practical single-mode fibers. *In proceedings Conference on Lasers and Electrooptics*, page paper CMD6, 2005.

[140] A. Ferrando, E. Silvestre, J. J. Miret, P. Andres, and M. V. Andres. Donor and acceptor guided modes in photonic crystal fibers. *Optics Letters*, 25(18):1328–1330, 2000.

[141] M. Yan and P. Shum. Guidance varieties in photonic crystal fibers. *Journal of the Optical Society of America B-Optical Physics*, 23(8):1684–1691, 2006.

[142] K. Busch and S. John. Photonic band gap formation in certain self-organizing systems. *Physical Review E*, 58(3):3896–3908, 1998.

[143] B. T. Kuhlmey, R. C. McPhedran, and C. M. de Sterke. Modal cutoff in microstructured optical fibers. *Optics Letters*, 27(19):1684–1686, 2002.

[144] J. C. Baggett, T. M. Monro, K. Furusawa, V. Finazzi, and D. J. Richardson. Understanding bending losses in holey optical fibers. *Optics Communications*, 227(4-6):317–335, 2003.